The Finite Temperature QCD Phase Transition and the Thermodynamic Equation of State

An Investigation Employing Lattice QCD with $N_f = 2$ Twisted Mass Quarks

D I S S E R T A T I O N

zur Erlangung des akademischen Grades

d o c t o r r e r u m n a t u r a l i u m
(Dr. rer. nat.)
im Fach Physik

eingereicht an der
Mathematisch-Naturwissenschaftlichen Fakultät I
der Humboldt-Universität zu Berlin

von
Dipl.-Phys. Florian Burger

Präsident der der Humboldt-Universität zu Berlin:
Prof. Dr. Jan-Hendrik Olbertz

Dekan der Mathematisch-Naturwissenschaftlichen Fakultät I:
Prof. Stefan Hecht PhD

Gutachter:
1. Prof. Dr. Michael Müller-Preußker
2. Dr. Maria-Paola Lombardo
3. Prof. Dr. Edwin Laermann

eingereicht am: 04. Oktober 2012
Tag der mündlichen Prüfung: 21. Dezember 2012

Abstract

Heavy ion collision experiments at the *Relativistic Heavy Ion Collider* (RHIC) at BNL or at the *Large Hadron Collider* (LHC) at CERN are routinely performed today and provide insight into a new phase of strongly interacting matter that is created for a short time after the collision - the quark gluon plasma.

Its theoretical description requires the knowledge of the thermodynamic equation of state (EoS) of the plasma. It is calculable within the lattice approach to quantum chromodynamics, the established theory of strong interactions. The lattice discretisation however requires the complete control of the continuum limit to be taken in the end. Current discrepancies in results from different lattice collaborations suggest this to be very crucial for the EoS.

In this work we report about an evaluation of the trace anomaly providing the pressure and energy density. We employ the Wilson twisted mass discretisation of the quark action. This formulation is known to have an automatic improvement of lattice artifacts that are proved to occur only in the second order of the lattice spacing. Including two dynamical light quark flavours the twisted mass discretisation has been applied very successfully at zero temperature. This work presents first robust results for the non-vanishing temperature case. Due to the missing *strange* quark flavour, the results for the EoS are of qualitative nature useful to disentangle its *strange* quark contribution. The continuum limit of the trace anomaly is studied using several values of N_τ and the tree-level correction technique. From the corrected and interpolated trace anomaly the EoS is obtained from the temperature integral method.

Moreover, we are able to contribute to the yet unresolved question of the order of the two flavour phase transition in the chiral limit, for which two possibilities usually are discussed: a second order transition in the universality class of an $O(4)$ symmetric 3-dimensional spin model or alternatively a first order transition. For our currently simulated pion masses in the range of 300-700 MeV we present evidence that the finite temperature transition we observe is a crossover transition.

For these masses the chiral condensate as the order parameter in the chiral limit is analysed in comparison with the $O(4)$ universal scaling function which characterises a second order transition. It is found to agree with the collected numerical data, however only if several scaling violating contributions are considered, thus prohibiting a final conclusive statement.

Further, we investigate the chiral limit by comparing the scaling of the observed crossover temperature with the mass considering several possibilities among them above alluded ones. For the $O(4)$ scenario we find the transition temperature $T_c = 152\ (26)$ MeV in the chiral limit.

Zusammenfassung

Die heute routinemäßig durchgeführten Schwerionen-Experimente - etwa an dem bei BNL beheimateten *Relativistic Heavy Ion Collider* (RHIC) oder am *Large Hadron Collider* (LHC) am CERN - gewähren uns Einblick in einen neuen Zustand stark wechselwirkender Materie, das Quark-Gluon-Plasma. Für dessen theoretische Beschreibung benötigt man die thermodynamische Zustandsgleichung des Plasmas. Die Gitter-Methode zur Regularisierung der Quanten-Chromodynamik, der etablierten Theorie der starken Kraft, ermöglicht deren Bestimmung. Bei dieser Methode ist jedoch entscheidend, Artefakte, die aus der Diskretisierung resultieren, unter Kontrolle zu haben. Dass dieser so genannte Kontinuum-Limes besonders für die Zustandsgleichung wichtig ist, zeigen momentane Diskrepanzen der Resultate verschiedener Kollaborationen für diese Größe.

In der vorliegenden Arbeit wird die Spur-Anomalie, sowie ausgehend von dieser der Druck und die Energiedichte des Plasmas berechnet. Hierfür wird die Wilson twisted-mass Formulierung der Quark-Wirkung verwendet. Diese bietet hinsichtlich des Kontinuum-Limes eine bewiesene automatische Verbesserung, wodurch die dominierenden Artefakte der Diskretisierung erst in der zweiten Ordnung des Gitterabstandes zu erwarten sind. Sie wurde im Falle von zwei dynamischen Quark-Flavour bei verschwindender Temperatur erfolgreich angewendet.

In dieser Arbeit werden erste belastbare Resultate dieser Wirkung bei endlicher Temperatur gezeigt. Die Resultate für die Zustandsgleichung sind wegen des fehlenden *strange* Quarks von qualitativer Natur und können zur Abschätzung des *strange* Quark Beitrages herangezogen werden. Desweiteren wird der Kontinuum-Limes der Spur-Anomalie mit mehreren Gitterdiskretisierungen der Temperatur N_τ sowie unter Zuhilfenahme einer tree-level Korrektur untersucht. Die korrigierte und interpolierte Spur-Anomalie dient als Ausgangspunkt für die Berechnung der Zustandsgleichung mit Hilfe der Temperatur-Integral Methode.

Weiterhin können wir zur Lösung der bislang unbeantworteten Frage nach der Ordnung des Phasenüberganges der QCD mit zwei Quark Flavour beitragen. Im masselosen Grenzfall werden hierfür im Allgemeinen zwei Möglichkeiten diskutiert: a) ein Phasenübergang zweiter Ordnung in der Universalitätsklasse eines $O(4)$-symmetrischen dreidimensionalen Spin-Modells, oder b) ein Übergang erster Ordnung. Im Bereich der hier simulierten Pion-Massen zwischen 300 und 700 MeV wird von uns jedoch ein Crossover-Übergang beobachtet.

Für diese Massen wurde das chirale Kondensat, der Ordnungsparameter für die spontane Brechung der chiralen Symmetrie, vor dem Hintergrund der so genannten magnetischen Zustandsgleichung untersucht. Diese Funktion gibt das universelle Verhalten in der Nähe des Phasenüberganges für die Universalitätsklasse des $O(4)$ Modells an. Sie beschreibt die numerischen Daten, jedoch nur unter Hinzunahme eines oder mehrerer Zusatz-Terme, die die Verletzung der Universalität parametrisieren. Aus diesem Grunde ist zum jetzigen Zeitpunkt noch keine definitive Aussage hinsichtlich der Natur des Phasenüberganges möglich.

Darüber hinaus wurde die Abhängigkeit der gemessenen Crossover-Temperatur von der Masse untersucht und eine Extrapolation unter der Annahme verschiedener Szenarien für den chiralen Limes (darunter die oben genannten) analysiert. Für den Fall des $O(4)$ Szenarios erhalten wir $T_c = 152\ (26)$ MeV für die Übergangstemperatur im chiralen Limes.

Contents

1 Introduction

Constituting a tremendous success, the Standard Model of particle physics is capable of describing three out of the four known elementary forces of our world within one unique framework, namely the framework of renormalisable quantum field theory. Apart from gravity, the electromagnetic, weak as well as strong interactions are thereby encoded in the following group structure of underlying local $SU(N)$ gauge theories

$$SU(3)_{\text{strong}} \times SU(2)_{\text{weak}} \times U(1)_{\text{em}} \, .$$

The theory of the strong force is called quantum chromodynamics (QCD) and describes the interaction of the mediators of the force, the eight gluons, and the strongly interacting matter, the quarks that carry the colour charge. While the weak and electromagnetic interactions can be treated sufficiently well in terms of perturbative series expansions in their respective small coupling parameters, this is not possible for QCD at hadronic energy scales of about 1 GeV. In this regime a generically non-perturbative approach such as lattice QCD is needed for a reliable description of the dynamics. Due to the running of the coupling with the typical scale of energy in a process a perturbative treatment however becomes feasible at energy scales of a few GeV as the coupling is decreasing with increasing energy transfer of a process. The latter is known under the name of asymptotic freedom [Pol73, GW73, GW74]. At asymptotically large energies quarks can be considered as free, non-interacting particles, while at small energies they are bound together with gluons within hadrons as states of three valence quarks (the baryons) or as pairs of a quark and an anti-quark (the mesons). Particles affected by the strong force only exist within such colour neutral bound states, a phenomenon called confinement.

In 1965, R. Hagedorn realised that a limiting temperature T_{H} for hadronic matter should exist [Hag65]. From statistical considerations he deduced that the density of hadronic states $\rho(p)$ is growing exponentially with the temperature, which was also found experimentally, up to the energies that were within reach at that time. In this way the partition function

$$Z \propto \prod_i \int d^3p_i \; \rho(p_i) e^{-\frac{E_i(p_i)}{T}} = \prod_i \int d^3p_i \; e^{-\frac{E_i(p_i)}{T} + cT}$$

gets singular when the exponent approaches zero for $T \to T_{\text{H}}$. This is considered the first indication for a phase transition of hadronic matter [CP75]. Such a transition has also been predicted in early lattice studies of the gluon sector (using two colours) alone i. e. neglecting quarks [MS81a, KPS81].

For the case of QCD with three dynamical light quarks at their respective physical

masses, the phase transition from the hadronic confined phase at $T = 0$ to the deconfined and chirally restored phase has been located concordantly in a temperature range of $150-170$ MeV[1] by two independent collaborations, [B$^+$10b, BBC$^+$12] after long standing differences (see e. g. Refs. [ADF$^+$09, AFKS06, CCD$^+$06]) about the precise position in temperature have been attributed to remaining lattice artifacts.

However, the use of staggered fermions that have been employed for the successful localisation of the physical crossover temperature range is widely debated in literature (c. f. [Kro07, Cre07]). The so called "rooting trick" is utilised by taking the fourth root of the fermion determinant in the course of simulation. Nevertheless, their use is very popular due to significantly reduced numerical costs in comparison to for instance Wilson fermions. The latter (and variations of these, e. g. Wilson twisted mass fermions as are used in this work) are in turn based on save theoretical grounds but are much more demanding in terms of computer time. As a consequence, finite temperature simulations with Wilson fermions are currently performed at pion masses $\gtrapprox 300$ MeV, so yet somewhat above the physical point.

The mass dependence of the QCD phase diagram has been studied within various numerical setups as well as theoretically throughout literature. The pure gluonic system (corresponding to the case of infinitely heavy quarks) has been predicted [SY82] and confirmed by numerical simulation ([FOU90] and references therein) to feature a true first order transition. This case corresponds to the upper right corner of Fig. 1.1 (right panel) which shows the nature (order) of the phase transition depending on the mass (and number) of light quark flavours. It is observed that the phase transition is also present, if two or three light quark are included in the simulations. Its strength however weakens towards lighter quark masses and the transition becomes a crossover transition separated from the first order region by a second order phase boundary line in the universality class of a $Z(2)$ spin model in three dimensions.

Towards lower quark masses another symmetry of $N_f = 2$ ($N_f = 3$) QCD becomes increasingly relevant, namely its global chiral $SU(2)\times SU(2)$ ($SU(3)\times SU(3)$) symmetry. At $T = 0$ this symmetry is spontaneously broken by the QCD vacuum which develops a non-vanishing quark condensate (also called chiral condensate). However, this symmetry is only approximate at finite quark masses as it is explicitly broken by their small masses. At $T > 0$ chiral symmetry gets restored across the transition, the restoration taking place in a similar range of temperatures as the system also enters the deconfined phase.

Towards vanishing masses of the *up*, *down* and *strange* quarks, the system develops again a first order transition (the lower left corner of Fig. 1.1 (right panel)). In recent years, lattice simulations have become more and more advanced and simulations with physical quark masses have been possible with staggered types of discretisation. The thermal transition with physical setup of the light masses has been located to lie in the crossover region of the phase diagram [AEF$^+$06]. The phase diagram has thus been

[1] As the nature of the transition at physical quark masses is merely a crossover than a genuine phase transition, the location in temperature can be observable dependent. Therefore one is to study the temperature dependence of a given observable in the crossover region, which should coincide among different lattice discretisations once lattice artifacts are sufficiently under control.

widely explored by lattice QCD simulations with the exception of the upper left corner including the two flavour case. The order of the phase transition (if any) for two massless flavours remains yet unknown although di erent lattice studies have tried to conclude on its nature by testing the presence of universal scaling in the vicinity of a second order critical point. While good agreement of numerical data with a second order transition was found in Refs. [AK+01b] and [BHM+10], a first order transition is favoured in Ref. [DDGP05]. Thus the situation is so far inconclusive and we can hope to contribute settling this point.

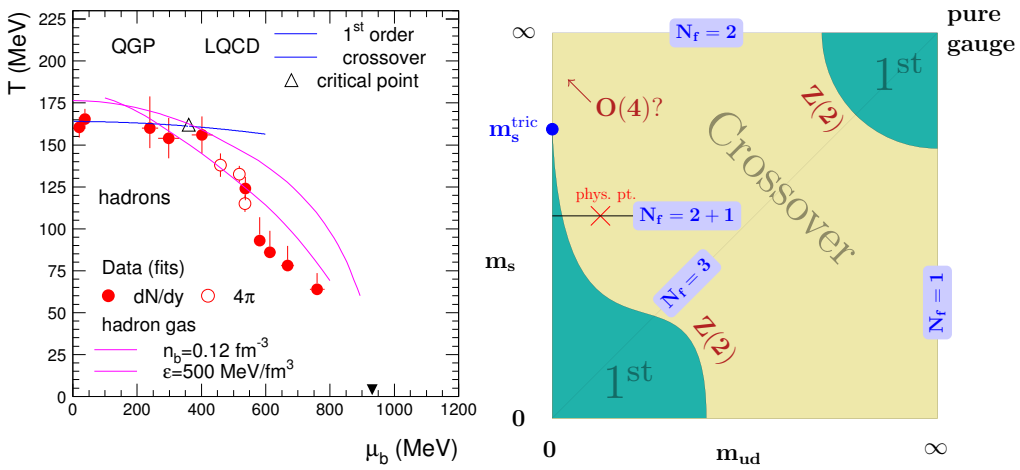

Figure 1.1: Left: Measured phase diagram of QCD in the T-μ_B plane from experiment taken from Ref. [ABMS06]. **Right**: Current knowledge of the dependence of the QCD at vanishing chemical potential $\mu_B = 0$ on the masses of the three lightest quarks $m_{u,d,s}$. *up* and *down* quarks are taken to be mass-degenerate. The schematic figure is adopted from Ref. [LP03].

For some years now heavy ion collision experiments as for instance performed at the RHIC collider (and newly also at LHC) have enabled us to study the QCD phase transition in experiment. The basic strategy of these experiments is to accelerate heavy nuclei (such as gold or lead) up to highly relativistic energies and to collide them within a detector thereby creating conditions as have been present in the hot early stage of the universe (at about 10^{-5} seconds of its existence Ref. [BMS07]). After a short time of the order of 1 fm/c in which the highly excited nucleus (or a part of it) is out of equilibrium, eventually an equilibrated quark gluon plasma (QGP) is formed. When the expanding quark gluon system has cooled down su ciently, it crosses the boundary of the phase transition and (re-)enters the hadronic phase and the so called freeze-out of the system occurs.

The relative abundances of particle species that are detected after hadronisation may be used to compute the temperature T and the baryonic chemical potential μ_B by comparing them to the abundances assuming the species to be in chemical equilibrium

according to their respective statistics [BMW09]:

$$n_i \propto \int_0^\infty dp \frac{p^2}{\exp\left[\left(E_i - \mu_i\right)/T\right] \pm 1} \ ,$$

where $E_i = \sqrt{(p^2 + m_i^2)}$ is the relativistic energy of the i-th produced particle and μ_i is its chemical potential. From fits of collider data to this formula one can infer the temperature and the baryonic chemical potential μ_B of the fireball at freeze-out. Such an analysis allows to draw the phase diagram of QCD from experimental data as is shown in Fig. 1.1 (left panel) [ABMS06]. In the small μ_B region that is accessible to lattice computations, a comparison to the predictions of lattice QCD is possible.

Within the intermediate period of expansion the equilibrated QGP system is theoretically describable by a relativistic hydrodynamics model of an ideal relativistic fluid (i. e. neglecting viscosity). The differential equations for the ideal fluid case that govern the evolution of the flow u_μ in an infinitesimal volume element have the following form [SBS10]:

$$\dot{\epsilon} = -(\epsilon + p)\theta \qquad \text{and} \qquad (\epsilon + p)\dot{u}^\mu = \nabla^\mu p$$
$$\text{with}: \theta = \partial^\mu u_\mu \qquad \dot{\{\ldots\}} \equiv u_\mu \partial^\mu \{\ldots\} \qquad \nabla^\mu \{\ldots\} \equiv \left(g^{\mu\nu} - u^\mu u^\nu\right) \partial_\nu \{\ldots\} \ .$$

In order for these equations to close, additional input about the equation of state (EoS) $p(\epsilon)$ is needed to relate the pressure p to the energy density ϵ of the hot medium. In the past, it has mostly been taken from model calculations, see for instance [HKH$^+$01], while the initial conditions for above evolution equations are adopted from a Glauber or a colour glass condensate type of model [SBS10]. Such hydrodynamic modeling is capable of describing experimental data at least on the qualitative level as is shown in Fig. 1.2, which presents hydrodynamic predictions for the elliptic flow coefficient $v_2 = \langle \cos(2\Phi) \rangle$ as function of the transverse momentum p_t. v_2 is the second Fourier coefficient of the azimuthal (Φ-) distribution of particles, which is anisotropic due to a non-vanishing impact parameter of the two colliding nuclei. The theoretical predictions are confronted with data from the STAR and PHENIX experiments at RHIC. The rather good agreement of an ideal hydrodynamic model with the data is evidence for the QGP behaving close to an ideal liquid with small ratio of shear viscosity η to entropy density.

Lattice QCD is capable of providing the EoS as input to hydrodynamics evolution from a first principle approach to QCD. In this respect calculations with staggered quarks are again the most advanced in comparison with other discretisations. Consequently two collaborations report results on the EoS with $2 + 1$ flavours at their physical masses [BEF$^+$10, CEH$^+$10]. These are however incompatible with one another so far. Given these yet unresolved discrepancies, it is worthwhile to study the EoS with alternative fermionic discretisation (e. g. the Wilson twisted mass formulation) in order to check for systematic errors as well as to test for universality in the results. Furthermore, only few results for the EoS with Wilson fermions exist so far and have been obtained yet more or less far away from physical quark masses and the continuum limit for $N_f = 2$

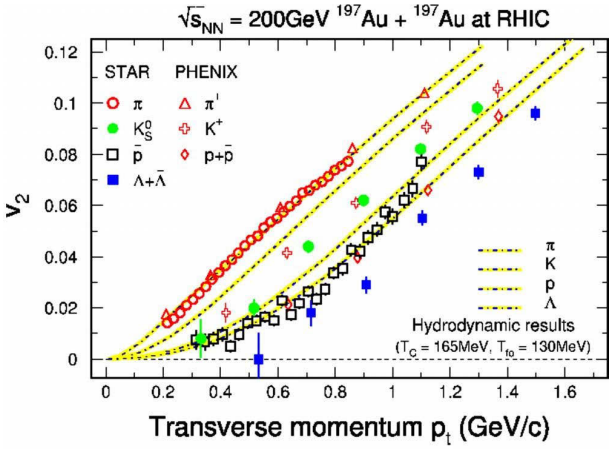

Figure 1.2: Elliptic flow v_2 as a function of transverse momentum. The picture is taken from Ref. [BMW09] and shows the experimental data of the STAR collaboration [A$^+$05] with hydrodynamic model predictions from Ref. [HKH$^+$01].

in [AK$^+$01a] and recently for $N_f = 2 + 1$ using a new approach in [U$^+$10].

This work is organised as follows. In chapter 2 we will outline the necessary theoretical basis and discuss the studied observables in chapter 3. The chapters 4, 5 and 6 are devoted to the presentation of our findings for the crossover temperature, its mass dependence towards the chiral limit and the thermodynamic EoS, respectively. We will present our concluding thoughts and discuss possible future work in chapter 7.

2 Twisted Mass Lattice QCD at $T > 0$

Starting with a short introduction to the continuum description of QCD we will define the lattice discretisation of the twisted mass quark action (section 2.2) and of the gauge action (section 2.3) that are used throughout this work. We continue by discussing the partition function at finite temperature (T) and give some details about its simulation. We proceed by reviewing the present knowledge of the specifics of the bare parameter phase space for the twisted mass action and outline the choice of simulation parameters used.

2.1 QCD in the Continuum

In the continuum, strong interactions among the gluons (represented by the fields A^μ) and the quarks (represented by the Grassmann valued fields ψ and $\bar{\psi}$) are described by the QCD Lagrangian

$$\begin{aligned} \mathcal{L}_{\mathrm{QCD}} &= -\frac{1}{2}\mathrm{Tr} F_{\mu\nu}F^{\mu\nu} + \sum_f \bar{\psi}^f_\alpha \left(i\gamma_\mu \partial^\mu - m_f + g\gamma_\mu A^\mu\right)^{\alpha\beta} \psi^f_\beta \\ &= \mathcal{L}_g + \mathcal{L}_f \ , \end{aligned} \tag{2.1}$$

see e. g. Ref. [PS95]. The sum goes over the six quark flavours found in nature. The field strength $F^{\mu\nu}$ is thereby constructed from the matrix valued A^μ (as being part of the algebra of $SU(3)$) as follows

$$F_{\mu\nu} = \partial_\mu A_\nu - \partial_\nu A_\mu - ig[A_\mu, A_\nu] \ . \tag{2.2}$$

The commutator is giving rise to gluon self interactions and g denotes the bare strong coupling constant. In terms of the above presented QCD Lagrangian the theory is defined by the partition function Z which is given as the following path integral

$$Z = \int D\psi D\bar{\psi} D A_\mu \mathrm{e}^{iS[\psi,\bar{\psi},A_\mu]} \tag{2.3}$$

over the fermionic and gluonic degrees of freedom with the action S defined as

$$S[\psi,\bar{\psi},A_\mu] = \int d^4x \mathcal{L}(x) = \int d^4x \left(\mathcal{L}_g + \mathcal{L}_f\right) \equiv S_g[A_\mu] + S_f[\psi,\bar{\psi},A_\mu] \ . \tag{2.4}$$

Due to the running of the coupling alluded to in the introduction, the effective coupling becomes large at small momentum scales and thus a perturbative description as a series expansion in the coupling is only possible at large momenta. However, Eq. (2.3) allows

for a numerical treatment in Euclidean space-time when turning to imaginary times and to Euclidean actions

$$\begin{aligned} t \to -i\tau \quad \Rightarrow \quad Z = \int D\psi D\bar{\psi} DA_\mu \mathrm{e}^{-\left(S_g^{\mathrm{E}}[A_\mu] + S_f^{\mathrm{E}}[\psi,\bar{\psi},A_\mu]\right)} \\ \mathcal{L}_g \to \mathcal{L}_g^{\mathrm{E}} \quad \mathcal{L}_f \to \mathcal{L}_f^{\mathrm{E}} \, . \end{aligned} \tag{2.5}$$

Then after that these continuum actions S_f^{E} and S_g^{E} have been discretised on a discrete space-time lattice, the integral Eq. (2.5) is solvable via Monte Carlo simulations on a (possibly fast) computer. This approach has so far proven to be the most successful technique for solving QCD and for giving theoretical predictions for hadronic quantities.

2.2 The Twisted Mass Fermion Action

The discretisation of the quark action (S_f^{E} in Eq. (2.5)) in use throughout this work is based on the popular discretisation due to Wilson [Wil77] whose derivation is by now discussed in many standard textbooks [MM94, Rot05]. The role of the continuum gauge fields A_μ is taken over by the lattice link fields U_μ that act as parallel transporters between neighbouring sites. We make the standard choice and set the Wilson parameter $r = 1$ here. The $N_f = 2$ version of Wilson's action is then modified by adding to it a second so-called twisted mass term proportional to $ia\mu\gamma_5\tau^3$:

$$\begin{aligned} S_f^{\mathrm{tm}}[U,\psi,\bar{\psi}] &= \sum_{x,y} \bar{\chi}(x) \left(\delta_{x,y} - \kappa D_{\mathrm{W}}(x,y)[U] + 2i\kappa a\mu\gamma_5\tau^3\delta_{x,y} \right) \chi(y) \\ &= \sum_{x,y} \bar{\chi}(x) D_{\mathrm{tm}}(x,y)\chi(y) \, . \end{aligned} \tag{2.6}$$

Here $D_{\mathrm{W}}(x,y)[U]$ denotes the Wilson Dirac operator which links neighbouring sites x and y that are separated by one unit of the lattice spacing a:

$$D_{\mathrm{W}}(x,y)[U] = \sum_\mu \left(1-\gamma_\mu\right) U_\mu(x)\delta_{y,x+a\hat{\mu}} + \left(1+\gamma_\mu\right) U_\mu^\dagger(x-a\hat{\mu})\delta_{y,x-a\hat{\mu}} \, . \tag{2.7}$$

It is accompanied by the quark mass related hopping parameter κ

$$\kappa = (2am_0 + 8r)^{-1} \tag{2.8}$$

and we denote the bare twisted mass parameter by $a\mu$ in Eq. (2.6). The commonly used field normalisation that renders the fermion fields χ dimensionless

$$\chi \to \frac{1}{\sqrt{2\kappa}} a^{3/2} \chi \, , \tag{2.9}$$

are already in place in above formulae and we amend that they are defined in the so-called twisted basis. This basis arises from the usual physical quark fields ψ (the physical

basis) by the following set of transformations:

$$\begin{aligned} \chi &= \exp\left(-i\alpha\gamma_5\tau^3/2\right)\psi \\ \bar{\chi} &= \bar{\psi}\exp\left(-i\alpha\gamma_5\tau^3/2\right) . \end{aligned} \tag{2.10}$$

It is noteworthy that due to the tracelessness of the flavour matrix τ^3 this rotation is free from producing unwanted quantum level anomalies. However, one has to rotate back into the physical basis in order to retrieve physical correlation functions after calculation in the twisted basis. Further basic features and implications of the twisted mass action are discussed in Ref. [Shi08].

The most remarkable fact about twisted mass fermions however is the property of so-called automatic $\mathcal{O}(a)$ improvement when the hopping parameter κ is tuned to its critical value, which is equivalent to set

$$\alpha = \frac{\pi}{2} \quad \text{(maximal twist)} \tag{2.11}$$

in Eq. (2.10) and is conventionally called *maximal twist*. Automatic improvement at maximal twist has first been pointed out in Ref. [FR04]. It implies that correlation functions have leading order lattice artifacts at $\mathcal{O}(a^2)$ and thus significantly improved continuum limit behaviour. The applicability of automatic improvement beyond the $T = 0$ case has been investigated in a quenched scaling analysis in Ref. [MPIJ$^+$09] for finite temperatures and has proven to be successful. The dependence of $\kappa_c = \kappa_c(\beta; T = 0)$ on the bare lattice gauge coupling $\beta = \frac{6}{g^2}$ has been established by the European Twisted Mass Collaboration (ETMC) [B$^+$08b] and is known for the range of couplings shown in Fig. 2.2 together with a Padé type of interpolation. For the tuning of the hopping parameter to its critical value, ETMC monitors the vanishing of the PCAC mass at large Euclidean time separations [B$^+$08b]:

$$\begin{aligned} m_{\mathrm{PCAC}} &= \frac{\langle \partial_0 A_0^a(x) P^a(0)\rangle}{2\langle P^a(x) P^a(0)\rangle} \quad a \in \{1,2\} \\ A_0^a &= \bar{\chi}\gamma_0\gamma_5\frac{\tau_a}{2}\chi \qquad P^a = \bar{\chi}\gamma_5\frac{\tau_a}{2}\chi , \end{aligned} \tag{2.12}$$

which is a sufficient condition for correct tuning to maximal twist. In practice however it has been found to be enough if the following condition is fulfilled [B$^+$08a]:

$$\left|\frac{m_{\mathrm{PCAC}}}{a\mu}\right| < 0.1 . \tag{2.13}$$

For the twisted mass case the usual bare untwisted quark mass (am_0) is connected via κ to the bare twisted mass ($a\mu$) by the following equation

$$(am_q) = \sqrt{\tfrac{1}{4}\left(\tfrac{1}{\kappa} - \tfrac{1}{\kappa_c}\right)^2 + (a\mu)^2} , \tag{2.14}$$

which states that, if $\kappa = \kappa_c$, the quark mass is made up solely from the twisted mass.

One drawback of the twisted formulation is the explicit breaking of parity symmetry by the twist term, which leads to a splitting of the mass of the pseudoscalar particles. More specifically, the flavour singlet (neutral) pion mass m_{PS}^{0} and the flavour doublet (charged) pion mass $m_{\mathrm{PS}}^{\pm}$ are not equal due to lattice artifacts. Although vanishing in the continuum with a power of a^2 in the lattice spacing, the splitting may be as large as 20 % at the masses and couplings simulated by ETMC [B$^+$10a]. Thus when referring to the mass of the pion this will be based on the mass of the charged pseudoscalar $m_{\mathrm{PS}}^{\pm}$.

2.3 Tree-Level Symanzik Improved Gauge Action

In the gauge sector of the action a tree-level Symanzik (tlSym) improved gauge action has been used in this work. By adding higher dimensional operators (vanishing in the continuum limit) to the standard Wilson plaquette action (the sum over all possible Wilson loops of length $4a$ (plaquettes) [Wil74]), it is possible to improve the continuum limit behaviour of the action. In this so-called Symanzik improvement program (cf. reference [DD06] for example) one may in this way correct the leading residual lattice artifacts of $\mathcal{O}(a^2)$ for the usual non-improved Wilson plaquette action by adding an irrelevant gauge-invariant order six operator term to yield:

$$\begin{aligned} S_g^{\mathrm{tlSym}}[U] = \beta\Big(c_0 \sum_P [1 - \frac{1}{3}\mathrm{ReTr}\,(U_P)] \\ + c_1 \sum_{\mathrm{R}} [1 - \frac{1}{3}\mathrm{ReTr}\,(U_R)]\Big)\,. \end{aligned} \tag{2.15}$$

Hereby the first sum goes over all $(6N_\tau N_\sigma^3)$ plaquettes of the lattice, where N_σ (N_τ) denote the number of lattice points in the spatial (time-like) direction. The additional second term corresponds to a sum over all unoriented planar rectangles U_R of length $6a$ and involves six link fields U_μ. The action is proportional to the bare lattice coupling $\beta = \frac{6}{g^2}$. At tree-level, leading lattice artifacts of this gauge action are expected at $\mathcal{O}(a^2 g^2)$ in the lattice spacing and the bare coupling g [LW85b, LW85a]. For the tree-level improvement to hold, the coefficients are fixed to the values $c_0 = \frac{5}{3}$ and $c_1 = -\frac{1}{12}$ [Wei83, WW84] satisfying $c_0 + 8c_1 = 1$.

2.4 The QCD Partition Function at $T > 0$

On the basis of the discretisations for the fermion and gauge actions in the previous sections, the hybrid Monte Carlo algorithm [DKPR87] is used to evaluate the partition function

$$Z = \int DU D\chi D\bar{\chi} \exp\left(-(S_f^{\mathrm{tm}} + S_g^{\mathrm{tlSym}})\right) = \int DU (\det D_{\mathrm{tm}}) \exp\left(-S_g^{\mathrm{tlSym}}\right) \tag{2.16}$$

numerically and to generate a Markov chain of gauge configurations with the correct probability distribution by means of importance sampling. To this purpose the Grass-

mann valued fermionic degrees of freedom are first integrated out analytically which yields the well known fermion determinant ($\det D_{\mathrm{tm}}$). It may be evaluated by means of a Gaussian integration over complex valued pseudo-fermion fields involving the numerically costly inversion of the fermion matrix. For the generation of gauge configurations we have made use of the publicly available hybrid Monte Carlo code package *tmLQCD* used by ETMC for their $T = 0$ simulations [UJSW06]. Additionally, the most compute intensive parts of the code (namely the inversions of the quark matrix and the calculation of gauge staples) have been ported to run on graphics accelerator hardware (GPUs) using NVIDIA's CUDA standard [NVI12]. We were thus able to effectively double the available numerical resources by running on $\mathcal{O}(30)$ GPUs. We refer the reader to appendix B for further details.

From thus generated gauge ensembles of N_g gauge configurations, the measurement of an observable $\langle O \rangle$

$$\langle O \rangle = \frac{1}{Z} \int DU \; O \; (\det D_{\mathrm{tm}}) \exp\left(-S_g^{\mathrm{tlSym}}\right) \tag{2.17}$$

proceeds as an averaging over the gauge ensemble obtained from the importance sampling, which converges to the right mean value for large N_g:

$$\frac{1}{N_g} \sum_k O_k \underset{N_g \to \infty}{\longrightarrow} \langle O \rangle \ . \tag{2.18}$$

Here, O_k denotes a measurement of O on a single gauge configuration. As subsequent gauge configurations generated in the Markov chain process are not independent of one another but are auto-correlated, it is important to estimate the autocorrelation of the measured observables and to take it into account. To this purpose we make use of the Γ-method [Wol04] employing an implementation due to C. Urbach [Urb12].

It now remains to highlight the connection between the statistical grand-canonical partition function Ξ that we want to study at finite temperature T, given volume V and chemical potential $\tilde{\mu}$ and the Euclidean partition function defined on the lattice Eq. (2.16). It is established by noting that Ξ is given as the trace over all quantum states and that upon discretising the time direction into infinitesimally small steps in Euclidean time can be expressed as a similar path integral as the Euclidean path integral of Eq. (2.5)

$$\begin{aligned} \Xi(T, V, \tilde{\mu}) &= \mathrm{Tr}\left(e^{-(\hat{H} - \tilde{\mu}\hat{N}_q)/T}\right) \\ &= \int D\psi D\bar{\psi} DA \; e^{-\int_0^{1/T} d\tau \int d^3x \left(\mathcal{L}_g^{\mathrm{E}}[A] + \mathcal{L}_f^{\mathrm{E}}[\psi, \bar{\psi}, A] - \tilde{\mu}\bar{\psi}\gamma_0\psi\right)} \\ &\underset{\tilde{\mu}=0}{\to} Z \ , \end{aligned} \tag{2.19}$$

which can be discretised in the same way as discussed above. The temperature appears as the upper integration bound in the exponent of the time integral and is thus given after discretisation as the inverse box length with N_τ lattice points in the Euclidean

time-like direction:

$$T = \frac{1}{N_\tau a} \,. \tag{2.20}$$

The boundary conditions in the temperature (time-like) direction are fixed by the nature of the trace in Eq. (2.19) to be periodic (anti-periodic) for the gauge (fermion) degrees of freedom (e. g. [Smi02]). Particle number is not conserved in Eq. (2.19) but the net quark number (Baryon number) is governed by the quark chemical potential $\tilde{\mu}$ (related to the baryonic chemical potential $\tilde{\mu}_B$ by $\tilde{\mu}_B = \tilde{\mu}/3$). However, as with $\tilde{\mu} \neq 0$ the fermion determinant becomes complex corresponding to the so-called sign problem (see for instance Ref. [Phi10]), a Monte Carlo approach as described above is impossible. Lattice QCD simulations are therefore restricted to vanishing chemical potential. However, several methods in order to access at least small chemical potentials are known in literature and we refer the reader to the discussion in Ref. [Phi10]. For the present work we so far restricted ourselves to the vanishing chemical potential case.

2.5 The Phase Diagram with Twisted Mass

The bare parameter space spanned by β, κ and $a\mu$ for the twisted mass lattice action at finite temperature and at vanishing chemical potential $\tilde{\mu} = 0$ has been studied in Ref. [IJL$^+$09]. It has been found that for fixed N_τ it is qualitatively divided up into three regions (see also Fig. 2.1):

- the Aoki-Phase [Aok84] for strong coupling, i. e. at small β,
- a bulk transition region [Mün04, SW05] at intermediate β with mass-dependent onset,
- the thermal transition and scaling region at larger β with the thermal transition line for $\mu \neq 0$ being part of a conical surface $(\kappa_t(\beta), a\mu(\beta))$ according to Eq. (2.14). The latter is also depicted in Fig. 2.1 and has been confirmed in Ref. [IJL$^+$09].

The two first mentioned unphysical phases have to be avoided in simulations for finite temperature QCD studies. In order to stay safely within the finite temperature scaling region, the coupling has to be chosen $\beta \gtrapprox 3.75$ [IJL$^+$09]. This fact together with the constraints presented by the bulk transition, which is also present at $T = 0$, limits the accessible temperature region for given time discretisation N_τ. In fact, for staying within the interval of couplings that have been simulated by ETMC ($\beta \geq 3.8$) it was necessary to simulate at $N_\tau = 12$ in order to cover the phase transition at the small pion masses that we wish to access. For a Wilson type of discretisation this is of course a challenging situation. Furthermore, using large values of N_τ presents limits on the precision one can obtain for the thermodynamic EoS (to be discussed in chapter 6) as the signal is expected to decrease dramatically with increasing N_τ.

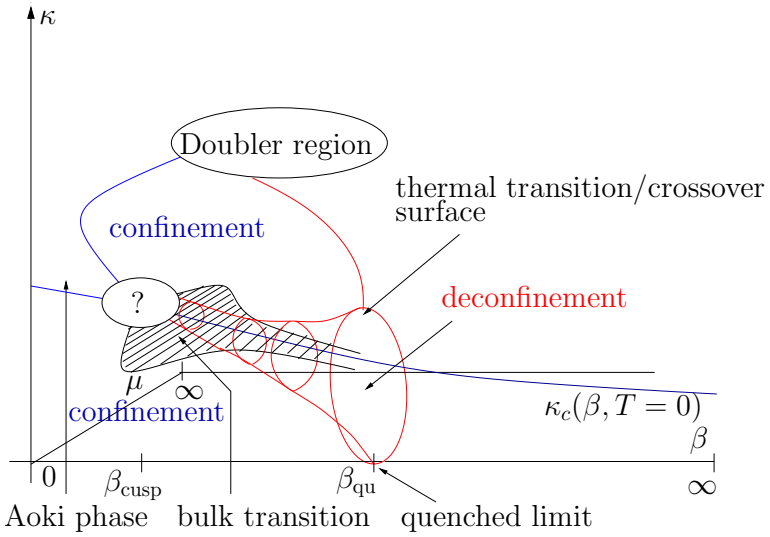

Figure 2.1: Phase diagram for twisted mass fermions extending in the μ direction [IJL+09] including the conical surface of the thermal transition.

2.6 Choice of Simulation Parameters

For automatic $\mathcal{O}(a)$ improvement to hold we have to simulate along the critical κ line while scanning across the phase transition. This prevents us from doing scans in the hopping parameter κ and allows only β- or $(a\mu)$-scans to be done. The advantage of doing scans in the bare coupling compared to doing scans in the mass is that when scanning temperature one is staying on a line of constant physics (LCP), which for the case of $N_f = 2$ is determined by a fixed constant pion mass. Staying on an LCP is especially crucial for the evaluation of the thermal equation of state (c. f. section 6).

Therefore, it is convenient to perform β-scans and to adjust $(a\mu)$ in such a way as to keep the physical pion mass approximately constant. The latter may be done using the one- or two-loop integrated β-functions $a_{1\mathrm{L}}$ and $a_{2\mathrm{L}}$ which relate the lattice spacing a to the (lattice) Lambda parameter Λ_L, the intrinsic scale of QCD:

$$\begin{aligned} 1-\mathrm{loop}: \quad & (a\mu)(\beta) = C_1 \exp\left(-\frac{\beta}{12\beta_0}\right) \equiv C_1 \; a_{1\mathrm{L}}(\beta) \\ 2-\mathrm{loop}: \quad & (a\mu)(\beta) = C_2 \left(\frac{6\beta_0}{\beta}\right)^{-\beta_1/2\beta_0^2} \exp\left(-\frac{\beta}{12\beta_0}\right) \equiv C_2 \; a_{2\mathrm{L}}(\beta) \; . \end{aligned} \tag{2.21}$$

The first two (universal) coefficients of the β-function are thereby given as

$$\beta_0 = (11 - 2N_f/3)/(4\pi)^2 \qquad \beta_1 = (102 - \frac{38}{3}N_f)/(4\pi)^4 \; . \tag{2.22}$$

The constants C_1 and C_2 that carry the dependence on Λ_L ($C_{1,2} \sim 1/\Lambda_L$) have been fixed using ETMC knowledge on the $(a\mu)$ dependence of the pion mass at $T = 0$. At values

of the coupling far above or far below the critical coupling β_c, the bare twisted mass has been set by using the two-loop equation. The relative difference between the one- and two-loop formulae is of the order of a few percent over the range of bare couplings β used in this work. As for smaller couplings (or for too large ranges in the coupling) the validity of the truncated perturbative series is not given, we have to check for violations of the LCP whenever we enlarge the range of couplings at $T = 0$. In section 6.6 we will further discuss this point and investigate how well we have tuned the LCP for two values of the pion mass for which we calculate the thermodynamic equation of state.

For setting κ to its critical value we have relied on the tuning of this parameter by the ETMC. Fig. 2.2 shows $\kappa_c(\beta)$ as well as a Padé fit to the data that has been constrained to the asymptotic value $\kappa_c = 1/8$ for zero coupling $g^2 = 6/\beta \to 0$. The fitted curve was used to set κ for all our finite temperature lattices and also for the runs at $T = 0$ that we have added in addition to the ETMC gauge ensembles. On these lattices we can thus check, how well the interpolation of the hopping parameter works and we find that the criterion Eq. (2.13) is well matched (c. f. table C.7 of the appendix). One exception to this is a lattice with $\beta = 3.65$ at $a\mu = 0.007903$ that has not been tuned well. We might thus face large discretisation effects there and a new tuning is required for the future.

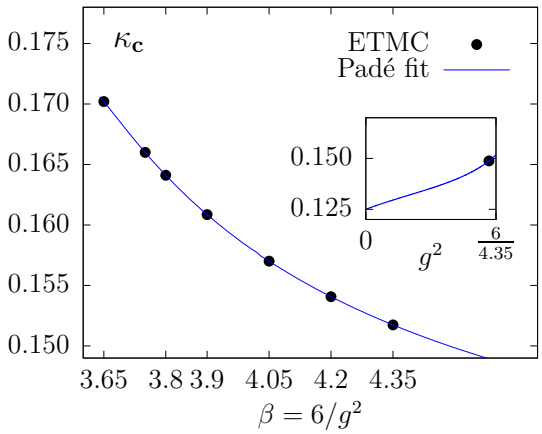

Figure 2.2: The dependence of the critical hopping parameter κ_c on the coupling β. The curve represents a Padé interpolation. In the inlaid figure we show the interpolation for asymptotically large $\beta = 6/g^2$, i. e. small g^2 where the fit has been constrained to $\kappa_c(g \equiv 0) = 1/8$ representing the attained value in the free limit.

In Fig. 2.3 we show a schematic picture of our so far performed simulations in terms of the pion mass and the discretisation in time N_τ. The figure also explains the naming convention we adopt in what follows to label our simulation points throughout this work. Much effort has been spent at $N_\tau = 12$ to simulate three ensembles at pion masses between 300 and 500 MeV in order to map out the dependence of the pseudo-critical temperature on the pseudo-Goldstone particle mass (orange points). For the purpose of studying cutoff effects, scans at $N_\tau = 10$ (blue points) and $N_\tau = 8$ (red points) have

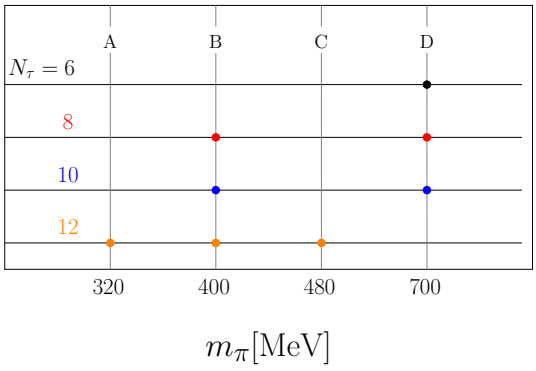

Figure 2.3: Schematic picture of β-scans that have been carried out. The simulation points are ordered according to the approximate pion mass m_π of the scan as well as with respect to the number of lattice points in the temporal direction. This figure also defines the naming scheme for our runs starting with the letter 'A' for the lightest pion mass that was used.

been performed for the B ensemble. At a somewhat larger mass of about 700 MeV (the D ensemble) we have performed high statistics runs to be able to study systematic effects in the evaluation of the thermodynamic quantities at $N_\tau = 10, 8$ and 6. The adopted naming convention consists in assembling a letter encoding the pion mass of a run and a number. We start with the letter 'A' for the lightest mass. and the number that is added corresponds to the value of N_τ in use. The simulations that were carried out for this work both at $T = 0$ and at $T > 0$ are listed with the corresponding bare parameters in appendix C. There we also provide results for the most relevant observables such as am_{PS} and $\left(\frac{r_0}{a}\right)$ for the $T = 0$ simulations.

For the D8 ensemble we have enlarged the range of available couplings at $T = 0$ beyond the range covered ETMC to span an interval in β of $3.65 \leq \beta \leq 4.6$. The lower bound even extends to a region in the coupling where one cannot expect to be in the finite temperature scaling region as for what has been discussed above in section 2.5. It therefore is especially crucial to check for lattice artifacts, which we have done by looking at three values of N_τ for the D mass where available. For the B (D) mass we have additionally simulated some points at $N_\tau = 4, 6$ ($N_\tau = 4$) in order to push the temperature to higher values and in order to study the impact of lattice artifacts on the thermal equation of state.

Another potential source of systematic errors are induced by a too small physical box size of the simulation. As a rule of thumb one should choose N_σ such that the condition $m_\pi L \geq 3$ is fulfilled in order to keep the finite size effect under control. This condition has been fulfilled on most of our $T = 0$ lattices (c. f. tables C.7 and C.8 in appendix C), apart from one point at $\beta = 4.35$, $a\mu = 0.00175$. This simulation (private communication with E. Garcia-Ramos) has been obtained on a lattice with a very small box size < 1.3 fm. We plan to redo the calculation on a larger lattice in the future.

3 Definition of Observables

In this chapter we provide definitions for some basic observables that are measured on the lattice. In section 3.1 we concentrate on bare thermal observables that will be used in the determination of the critical temperature later on. We then turn to the determination of some $T = 0$ observables relevant for this work, namely the determination of meson masses in section 3.2 and the determination of the force parameter r_0 (the Sommer parameter) in section 3.3. In sections 3.4 and 3.5 the renormalisation of the chiral condensate and the Polyakov loop is discussed.

3.1 Thermal Observables

We start by defining the basic gauge observables that have been studied. Building one part of the employed gauge action, the average plaquette is defined as:

$$\begin{aligned} P &= \frac{1}{6N_c N_\tau N_\sigma^3} \mathrm{ReTr} \sum_x \sum_{\mu>\nu} U_\mu(x) U_\nu(x+\hat{\mu}) U_\mu^\dagger(x+\hat{\nu}) U_\nu^\dagger(x) \\ &= \frac{1}{6N_\tau N_\sigma^3} \left(\frac{1}{3} \sum_P \mathrm{ReTr}\left(U_P\right) \right) . \end{aligned} \tag{3.1}$$

In the limit of infinitely heavy quarks, i. e. in the pure gauge case, the Polyakov loop

$$\hat{L}(\vec{x}) = \prod_{x_0=0}^{N_\tau - 1} U_0\left(x_0, \vec{x}\right) \tag{3.2}$$

constitutes an order parameter for the spontaneous breaking of centre symmetry. It indicates the thermal first order phase transition of the theory without fermions. According to Ref. [MS81b], $\hat{L}(\vec{x})$ is connected to the change in free energy when a single static quark is introduced into the Yang-Mills vacuum at space-time point $\vec{x}$:

$$\left\langle \mathrm{Tr}\hat{L}(\vec{x}) \right\rangle = \mathrm{e}^{-(F_q - F_0)/T} . \tag{3.3}$$

The inclusion of quarks explicitly breaks centre symmetry and $\hat{L}(\vec{x})$ is restricted to the trivial sector of the centre group. Thus we mainly consider the real part averaged over spatial volume:

$$\mathrm{Re}\left(L\right) = \mathrm{Re}\left\langle \frac{1}{N_c N_\sigma^3} \sum_{\vec{x}} \mathrm{Tr}\hat{L}(\vec{x}) \right\rangle , \tag{3.4}$$

where the trace is over colour. For these basic gauge observables we also measure variances

$$\chi_O = N_\sigma^3 \left\langle \left\langle O^2 \right\rangle - \langle O \rangle^2 \right\rangle \tag{3.5}$$

and integrated autocorrelation times τ_{int}. While the Polyakov loop is the order parameter in the limit of infinitely heavy quarks, the chiral condensate

$$\left\langle \bar{\psi}\psi \right\rangle = \frac{T}{V} \frac{\partial \ln Z}{\partial m_q} \tag{3.6}$$

constitutes an order parameter for the breaking of chiral symmetry at vanishing quark mass. From Eq. (2.14) at maximal twist ($\kappa = \kappa_c$) we can infer that $\left\langle \bar{\psi}\psi \right\rangle$ takes the form

$$\left\langle \bar{\psi}\psi \right\rangle = \frac{1}{N_\sigma^3 N_\tau} \left\langle \bar{\chi} i\gamma_5 \tau^3 \chi \right\rangle \tag{3.7}$$

in the twisted basis. It is expected to decrease monotonically towards zero across the transition into the chirally restored phase. Its variance over configurations on the other hand,

$$\sigma^2_{\bar{\psi}\psi} = \frac{V}{T} \left(\left\langle (\bar{\psi}\psi)^2 \right\rangle - \left\langle \bar{\psi}\psi \right\rangle^2 \right) , \tag{3.8}$$

which in this way makes up the disconnected part of the usual chiral susceptibility

$$\chi_\sigma = \frac{\partial \left\langle \bar{\psi}\psi \right\rangle}{\partial m_q} , \tag{3.9}$$

should exhibit a maximum in the transition region. The measurement of $\sigma^2_{\bar{\psi}\psi}$ in Eq. (3.8) involves the calculation of $\langle (\bar{\psi}\psi)^2 \rangle - \langle \bar{\psi}\psi \rangle^2$, which will be discussed in what follows.

The evaluation of a disconnected quantity such as $\left\langle \bar{\psi}\psi \right\rangle$ is usually performed using noise estimators [B$^+$08b]. It is therefore crucial to keep track of the multiplications in above expression to avoid the introduction of additional unwanted connected pieces which arise from multiplying an estimator with itself. To this end we adopt the following scheme for evaluating $\sigma^2_{\bar{\psi}\psi}$ from a given set of M stochastic estimators (in most cases we have used $M = 24$ and have checked for B12 that increasing to $M = 100$ does not change the result) of $\bar{\psi}\psi$. On a given configuration labelled by k we approximate $\bar{\psi}\psi_k$ from noise estimators in the following way:

$$\bar{\psi}\psi_k = \frac{1}{M} \sum_\alpha (\bar{\psi}\psi)^\alpha_k , \tag{3.10}$$

where α ranging from 1 to M denotes a single estimator and $(\bar{\psi}\psi)^\alpha_k$ denotes the α'th estimator on the k'th configuration. The evaluation of a single estimator $(\bar{\psi}\psi)^\alpha_k$ will be further illustrated in appendix A.1. In the following, Greek indices $\alpha, \beta \ldots$ enumerate the estimators while Latin indices $k, m, \ldots$ label gauge configurations. The two terms in

Eq. (3.8) are then estimated in the following way:

$$\left\langle (\bar{\psi}\psi)^2 \right\rangle = \frac{1}{N_g} \left(\sum_{k=1}^{N_g} \frac{1}{M(M-1)/2} \sum_{\alpha,\beta,\alpha<\beta} (\bar{\psi}\psi)_k^\alpha (\bar{\psi}\psi)_k^\beta \right), \tag{3.11}$$

and

$$\left\langle \bar{\psi}\psi \right\rangle^2 = \frac{1}{M(M-1)/2} \sum_{\alpha,\beta,\alpha<\beta} \left(\left(\frac{1}{N_g} \sum_{k=1}^{N_g} (\bar{\psi}\psi)_k^\alpha \right) \left(\frac{1}{N_g} \sum_{l=1}^{N_g} (\bar{\psi}\psi)_l^\beta \right) \right). \tag{3.12}$$

In both cases this procedure assures that estimators from a single source α are not squared on the same configuration k which would introduce connected contributions. We have however checked that a naive calculation of Eq. (3.8) which consists in averaging $(\bar{\psi}\psi)_k^\alpha$ over the noise and then calculating the naive variance produces the same result on the qualitative level.

3.2 Meson Masses

The masses of hadrons can be obtained from lattice simulations by studying correlation functions of appropriate lattice versions of operators that have the correct symmetry properties (quantum numbers) as the hadron of interest. Using the continuum formulation (superscript $(\ldots)^{\mathrm{C}}$) as a starting point, the correlation function C_{AB}^{C} of two local operators O_A and O_B separated a distance t in time is given as the following time-ordered product

$$C_{AB}^{\mathrm{C}}(t,\vec{x}) = \langle 0 | \, T \left\{ O_A(t,\vec{x}) O_B(0,\vec{0}) \right\} | 0 \rangle \ . \tag{3.13}$$

If one considers the integral over space dimensions of Eq. (3.13)

$$C_{AB}^{\mathrm{C}}(t) = \langle 0 | \int d^3x \ T \left\{ O_A(t,\vec{x}) O_B(0,\vec{0}) \right\} | 0 \rangle \tag{3.14}$$

and inserts the identity operator over single particle states (n) with energies $E_n(\vec{p})$

$$\mathbb{1} = |0\rangle \langle 0| + \sum_n \int d^3p \ \frac{1}{2E_n(\vec{p})} |n,\vec{p}\rangle \langle n,\vec{p}| \tag{3.15}$$

in between the operators O_A and O_B, $C_{AB}^{\mathrm{C}}(t)$ is projected onto zero momentum $\vec{p} = \vec{0}$. One arrives at the following expression:

$$\begin{aligned} C_{AB}^{\mathrm{C}}(t) = {} & \langle 0 | O_A(0,\vec{0}) | 0 \rangle \langle 0 | O_B(0,\vec{0}) | 0 \rangle \\ & + \sum_n \frac{1}{2E_n(\vec{0})} \left\langle 0 \right| O_A(0,\vec{0}) \left| n,\vec{0} \right\rangle \left\langle n,\vec{0} \right| O_B(0,\vec{0}) \left| 0 \right\rangle \mathrm{e}^{-\mathrm{i}E_n(\vec{0})t} \ , \end{aligned} \tag{3.16}$$

where $E_n(\vec{0}) = m_n$ is the mass of the n-th particle state. On the way we have used

$$O_A(t, \vec{x}) = \mathrm{e}^{\mathrm{i}p\cdot x} O_A(0, \vec{0}) \mathrm{e}^{-\mathrm{i}p\cdot x} \tag{3.17}$$

and the one-particle energies are given as the usual relativistic energies:

$$E_n(\vec{p}) = \sqrt{m_n^2 + (\vec{p})^2}\ . \tag{3.18}$$

Considering Eq. (3.16) in Euclidean space-time (superscript $(\ldots)^{\mathrm{E}}$) doing the replacement $t \to -\mathrm{i}\tau$ and assuming $O_{A,B}$ to have vanishing vacuum expectation value one realises that the state with lowest mass m_0 is the dominant contribution for $\tau \to \infty$ to the Euclidean correlation function C_{AB}^{E} and is calculable as

$$m_0 = -\lim_{\tau\to\infty} \frac{1}{\tau} \ln C_{AB}^{\mathrm{E}}(\tau). \tag{3.19}$$

Note that the approach outlined above is a priori only valid for stable particles on the mass shell. Thus in particular it is not useful for calculating the mass of the ρ- (vector-) meson which is a resonance state decaying into two pions. However, at the masses of the pseudoscalar particle that are so far accessible by our simulations, the mass of the pseudoscalar is too high for the rho to decay into a pair of these [JMMU09].

The meson creation and annihilation operators we need to determine the meson masses we are interested in have the following structure

$$O_A(x) = \bar{\psi}_f(x) \Gamma_A \psi_g(x), \tag{3.20}$$

where f, g denote the quark flavour. Γ_A is a generic combination of γ-matrices that represents the Dirac structure of the meson under consideration. They have to reflect the specific transformation properties of the meson under the discrete Lorentz symmetries, the parity (P), charge (C) and time reversal (T) transformations.

For a meson with a given γ-structure Γ_A we are lead to evaluating the following correlator Eq. (3.14) on the lattice:

$$\begin{aligned} C_{AA}^{\mathrm{L}}(t) &= a^3 \sum_{\vec{x}} \left\langle \bar{\psi}_f(t, \vec{x}) \Gamma_A \psi_g(t, \vec{x}) \bar{\psi}_g(0, \vec{0}) \Gamma_A \psi_f(0, \vec{0}) \right\rangle \\ &= -a^3 \sum_{\vec{x}} \left\langle \mathrm{Tr}\left(D_f^{-1}(0, x) \Gamma_A D_g^{-1}(x, 0) \Gamma_A \right) \right\rangle\ , \end{aligned} \tag{3.21}$$

where in the second line according to Wick's theorem we have inserted appropriate quark propagators $D_{g,f}^{-1}$, assuming for the moment different flavours g and f, such that no disconnected piece arises in the Wick contractions.

For the pion and the ρ-meson the according transformation properties as well as local operators are given in table 3.1, and we are left with the evaluation of the following

Meson	$I^G(J^{PC})$	Operator	Particle
Pseudoscalar	$1^-(0^{-+})$	$\bar{u}\gamma_5 d$	$\pi^\pm$
	$1^-(0^{-+})$	$\bar{u}\gamma_5\gamma_0 d$	$\pi^\pm$
Vector	$1^+(1^{--})$	$\bar{u}\gamma_i d$	$\rho^\pm$
	$1^+(1^{--})$	$\bar{u}\gamma_i\gamma_0 d$	$\rho^\pm$

Table 3.1: Quantum numbers of mesons according to [N$^+$10] as well as appropriate lattice operators.

correlation functions:

$$\begin{aligned} C^{\mathrm{L}}_{PP}(t) &= a^3 \sum_{\vec{x}} \left\langle \bar{d}(t,\vec{x})\gamma_5 u(t,\vec{x})\bar{u}(0,\vec{0})\gamma_5 d(0,\vec{0}) \right\rangle \\ C^{\mathrm{L}}_{VV}(t) &= a^3 \frac{1}{3} \sum_{i,\vec{x}} \left\langle \bar{d}(t,\vec{x})\gamma_i u(t,\vec{x})\bar{u}(0,\vec{0})\gamma_i d(0,\vec{0}) \right\rangle , \end{aligned} \tag{3.22}$$

where we have restricted ourselves to the cases not involving γ_0. For the evaluation of above correlators one can make profit of the γ_5-hermiticity of the twisted mass Dirac Operator (c. f. appendix A). The rotations between the physical and the twisted basis have to be accounted for properly. From fitting cosh- (or sinh-) functions symmetric (or antisymmetric) about the midpoint of the lattice to the correlators (Eq. (3.22)), one can extract the corresponding particle masses. For the pseudoscalar meson we are using the routines provided by the hadron package [Urb12] while for the vector meson we use our own implementation for performing correlated fits.

3.3 The Sommer Scale

For the conversion of lattice results into physical units the lattice spacing a needs to be determined. This so-called scale setting amounts to identify a physical quantity calculated on the lattice in units of a with the known physical value of this observable. This in turn fixes the value of a in fm ($1/a$ in GeV), and from this any other observable can be converted into physical units. To this end, one possibility is to consider the force $F(r)$ of an infinitely heavy (static) quark anti-quark pair that is separated a distance of r from one another:

$$r^2 F(r)\Big|_{r=r(C)} = C \; . \tag{3.23}$$

A common convention is to set $C = 1.65$ [Som94] and to use the thereby defined Sommer scale r_0. Phenomenologically r_0 is of the order of ≈ 0.5 fm, so well accessible by today's lattices. Its determination involves the calculation of the static potential $V(r)$ between two colour charges separated by a distance r from one another from which the force $F(r) = dV(r)/dr$ is readily computed. Following the discussions in Ref. [B$^+$08b], $V(r)$

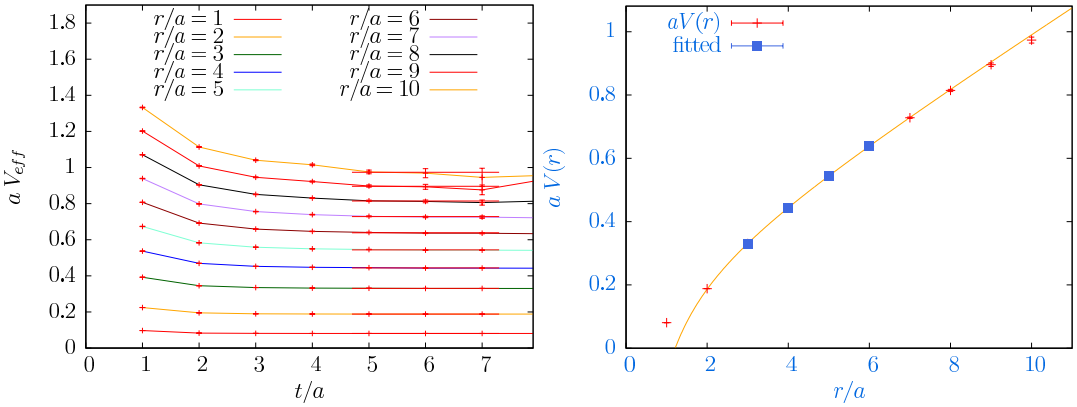

Figure 3.1: Effective mass plot for the extraction of the potential $V(r)$ (left). Horizontal lines indicate the value of the potential from fits to Eq. (3.25) and show the adopted range for the fit. The fit of Eq. (3.26) to the thereby extracted potential $V(r)$ (right) yields r_0/a. Data included in the fit is depicted by squares. The figures correspond to $\beta = 3.76$ and $a\mu = 0.022175$.

is obtained from measuring time-like Wilson-Loops:

$$W_{r,t}(x) = \frac{1}{3}\sum_{l=1}^{3}\prod_{y\in\mathcal{C}^l_{r,t}(x)} U_\kappa(y)\ , \tag{3.24}$$

where $\mathcal{C}^l_{r,t}(x)$ is a closed oriented path starting at space-time position x pointing into the l-th spatial direction and taking r steps in this direction before turning into the time-like direction for t steps. The path then closes by taking r steps in the negative l-th spatial direction and subsequently t steps in the negative time-like direction. Along the path the gauge link field $U_\kappa(y)$ always points into the direction of the step that is taken such that $\mathcal{C}^l_{r,t}(x)$ becomes a gauge invariant quantity. For large t the Wilson loop $W_{r,t}$ is connected to the static potential in the following way:

$$W_{r,t} \equiv \frac{1}{N_\tau N_\sigma^3}\sum_x W_{r,t}(x) \underset{t\to\infty}{\sim} C\mathrm{e}^{-tV(r)}\ , \tag{3.25}$$

such that the potential can be extracted at large enough time separations by

$$V(r) = -\lim_{t\to\infty}\frac{1}{t}W_{r,t}\ . \tag{3.26}$$

Once extracted from the Wilson loops the potential is fit to the formula

$$V(r) = V_0 + \frac{\alpha}{r} + \sigma r\ , \tag{3.27}$$

and r_0/a can be extracted from the interpolation provided by the fit.

In order to increase the overlap of the string operator with the ground state, we use spatial APE smearing [A$^+$87]. The signal to noise ratio is improved by using modified HYP smeared links in the time direction [HK01]. HYP smearing is known to shift the value of the static potential by a constant, while the force is not changed. Figure 3.1 (left) shows an effective mass plot of the potential

$$a\, V_{eff}(t) = -\log\left(W_{r,t+1}/W_{r,t}\right) \tag{3.28}$$

for different spatial separations r. In the right panel the corresponding potential $V(r)$ with a fit to Eq. (3.27) is illustrated.

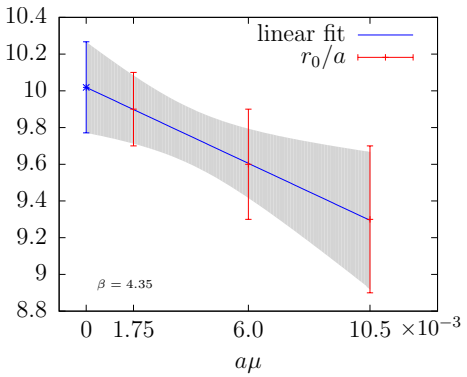

Figure 3.2: Linear chiral extrapolation of the Sommer scale for $\beta = 4.35$.

For the calculation of Wilson loops, the extraction of the potential and the determination of r_0/a we have used part of the ETMC contraction code as well as fitting routines provided by M. Wagner. We have used 20 steps of APE smearing and HYP smearing parameters have been set to $\vec{\alpha} = (1, 1, 0.5)$ which corresponds to the standard choice also used by ETMC [B$^+$08b]. We have performed the fits in several fit intervals in order to investigate the systematic effects associated therewith. In all cases we have checked to obtain good plateaus for $V_{eff}(t)$ for all distances r/a that are used to fit the static potential and we only consider such fits in the analysis. The spread of the fitted values for r_0/a obtained from several fits is used to estimate the systematic error associated with the freedom in the choice of the fit ranges. We add this error to the statistical error in quadrature. For the moment we have not yet performed a check of how much higher state excitations are contaminating our results of r_0/a by considering different levels of smearing and solving the generalised eigenvalue problem.

For $\beta = 3.8, 3.9, 4.05, 4.2$ we use values for r_χ/a reported in Table 7 of Ref. [B$^+$10a]. At all other values of β where at least two simulated values of the light quark mass are available we perform linear fits in the bare mass ($a\mu$) in order to obtain chirally extrapolated values for the Sommer scale r_χ. According to Ref. [B$^+$10a, B$^+$08b] an extrapolation linear in the square of the light quark mass could also be possible, but we stick to linear fits in ($a\mu$) here that are compatible with data. As an example we show the extrapolation for $\beta = 4.35$ in Fig. 3.2.

3.4 Renormalisation of the Chiral Condensate

Due to the breaking of chiral symmetry the chiral condensate as computed from Wilson fermions is known to have an additive as well as multiplicative renormalisation [BMM+85]. While with standard Wilson fermions the additive divergence is present even in the chiral limit, the situation is more favourable in the maximally twisted mass case as the renormalised chiral condensate is of the form [Vla11]:

$$\langle\bar{\psi}\psi\rangle_{ren} = Z_{\mathrm{P}}\left(\left\langle\bar{\chi}i\gamma_5\tau^3\chi\right\rangle_{bare} + \frac{\mu\ c_{\mathrm{P}}(\beta)}{a^2}\right) + \dots\ . \tag{3.29}$$

The ellipsis represents less divergent mass dependent powers in $1/a$ and we thus observe that for twisted mass the additive divergences vanish in the chiral limit. We therefore define the following subtracted chiral condensate $\langle\bar{\psi}\psi\rangle_R$ (private communication with M. P. Lombardo):

$$\langle\bar{\psi}\psi\rangle_R = \frac{\langle\bar{\psi}\psi\rangle(T,\mu) - \langle\bar{\psi}\psi\rangle(0,\mu) + \langle\bar{\psi}\psi\rangle(0,0)}{\langle\bar{\psi}\psi\rangle(0,0)}\ , \tag{3.30}$$

where $\langle\bar{\psi}\psi\rangle(T,\mu)$ is $\langle\bar{\psi}\psi\rangle$ evaluated at finite temperature T and finite μ. Further we assume the renormalisation pattern of Eq. (3.29) to apply equally at finite temperature. As in the chirally restored phase for $T \to \infty$ we have $\langle\bar{\psi}\psi\rangle(T,\mu) \to 0$ we observe on the one hand that in the chiral limit this quantity vanishes for large temperatures. On the other hand for small T the first two terms in the numerator cancel, such that $\langle\bar{\psi}\psi\rangle_R$ becomes unity. Thus this quantity resembles the behaviour of an order parameter in the chiral limit.

At zero temperature $\langle\bar{\psi}\psi\rangle(0,\mu)$ is obtained from an interpolation in the mass μ by means of a polynomial of degree two. For the interpolations in β we use a spline fit. At the smallest mass for each value of β[1] we additionally perform an infinite volume extrapolation for the $T = 0$ condensate $\langle\bar{\psi}\psi\rangle(0,\mu)$ with the following ansatz:

$$\frac{\langle\bar{\psi}\psi\rangle(L) - \langle\bar{\psi}\psi\rangle(L=\infty)}{\langle\bar{\psi}\psi\rangle(L=\infty)} = A_L \cdot \exp\left(-m_{\mathrm{PS}}L\right)\ , \tag{3.31}$$

where we have omitted the labels for zero temperature and mass for better readability. $\langle\bar{\psi}\psi\rangle(L=\infty)$ and A_L are treated as fit parameters. The mass of the pseudoscalar am_{PS} is taken as input from the simulation with largest box size, respectively. We include the difference of $\langle\bar{\psi}\psi\rangle_R$ obtained without extrapolation to infinite volume as a systematic error.

For evaluating $\langle\bar{\psi}\psi\rangle(0,0)$ we moreover perform a chiral extrapolation of the interpolated $\langle\bar{\psi}\psi\rangle(0,\mu)$ data at every value of the coupling of interest. We use a linear extrapolation through three points at every β. The data is compatible with linear μ-

[1] We restrict ourselves to $\beta = 3.8, 3.9, 4.05, 4.2$, where several volumes are available for the smallest simulated mass. We have not considered $\beta = 3.9$, $a\mu = 0.003$ as no other box size is available there such that $a\mu = 0.004$ is the smallest mass at this coupling.

dependence over the whole temperature range we consider here. In order to perform these tasks all available $T = 0$ ETMC lattices have been used.

The result for the renormalised chiral condensate for the B mass is shown in Fig. 3.3. The temperature scale is based on method 2 for scale setting (c. f. section 4.1). Indeed $\langle\bar{\psi}\psi\rangle_R$ seems to follow the familiar curve of an order parameter in the transition region. Most notably, the curves for different lattice discretisations N_τ agree, some slight tension being visible when comparing the two finest discretisations at low temperatures. For large temperatures the error is mostly dominated by the systematic error corresponding to the infinite volume extrapolation which demands for further investigation.

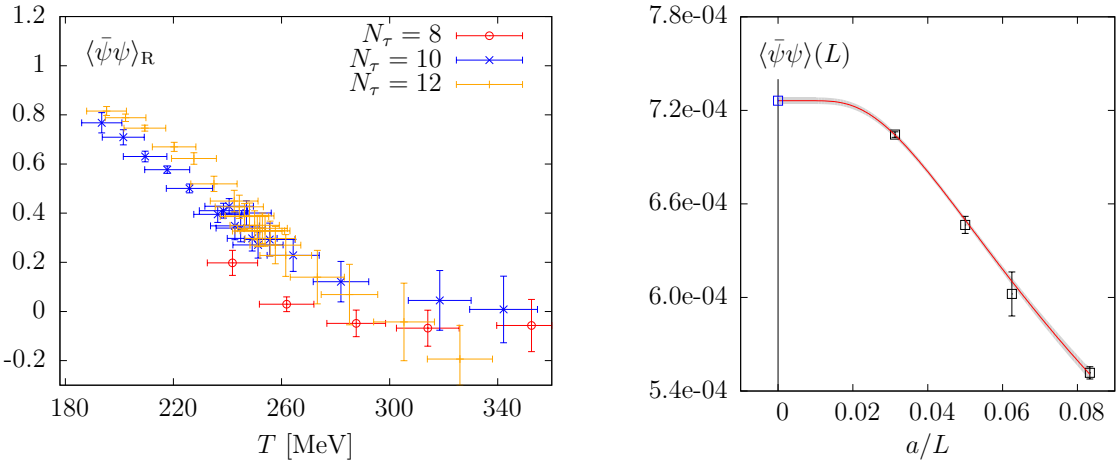

Figure 3.3: Left: Renormalised chiral condensate $\langle\bar{\psi}\psi\rangle_R$ as a function of the temperature (scale setting method 2) for the B ensembles with $N_\tau = 8, 10, 12$. **Right**: Extrapolation to infinite volume at $T = 0$ for $\beta = 4.05$ and $a\mu = 0.0030$.

3.5 Renormalisation of the Polyakov Loop

The correlator of Polyakov loops at finite temperature located at space points $\vec{x}$ and $\vec{0}$

$$\left\langle \mathrm{Tr}\hat{L}^\dagger(\vec{x})\mathrm{Tr}\hat{L}(\vec{0})\right\rangle \tag{3.32}$$

is connected to the free energy of a quark anti-quark pair (see e. g. Ref. [Phi10]) present in the system

$$\left\langle \mathrm{Tr}\hat{L}^\dagger(\vec{x})\mathrm{Tr}\hat{L}(\vec{0})\right\rangle = \mathrm{e}^{-\frac{F_{\bar{q}q}(\vec{x},T)-F_0(T)}{T}} \underset{T\to 0}{\to} \mathrm{e}^{-\frac{V(|\vec{x}|)}{T}}\ , \tag{3.33}$$

where the static quark anti-quark potential $V(|\vec{x}|)$ is the difference in energy between the quark anti-quark state and the ground state. The real part of the Polyakov loop may thus be renormalised according to the following prescription used in Ref. [AFKS06]

for the renormalisation of the absolute value $|\langle L\rangle|$ of the Polyakov loop:

$$\langle \mathrm{Re}(L)\rangle_R = \exp\left(V(r_0)/2T\right)\left(\mathrm{Re}(L)\right) \equiv Z_L\left(\mathrm{Re}(L)\right) \ . \tag{3.34}$$

$V(r_0)$ is the static quark anti-quark potential evaluated at the Sommer scale r_0 both having been introduced to the reader in section 3.3. Considering the modulus of the complex renormalised Polyakov loop $|\langle L\rangle_{\mathrm{R}}|$ instead of $\langle \mathrm{Re}(L)\rangle_{\mathrm{R}}$ just results in somewhat larger errors, as we have checked that the imaginary part of L averages to zero over the gauge ensemble for all temperatures. In order to evaluate the potential V at $T = 0$ we interpolate in both the bare twisted mass $a\mu$ as well as in the bare coupling β using spline fits to V. As for r_0 we take the value at finite quark mass, i. e. not the chirally extrapolated values r_χ. The calculation of the potential proceeds along the prescription explained in section 3.3. However, as hypercubic blocking leads to a shift in $V(r)$ it is mandatory to refrain from using HYP smearing for this analysis. In Fig. 3.4 we show the renormalised Polyakov loop for the B ensembles ($N_\tau = 8, 10, 12$) as well as for the D ensembles ($N_\tau = 6, 8, 10$). For the conversion to temperature we have used method 2 for the scale setting as is explained in section 4.1. We observe a nice scaling behaviour throughout different temporal extents suggesting small residual lattice artifacts in our data apart from $N_\tau = 6$ for the D mass, for which we see a sizable deviation. The smallest available temperature point at around 250 MeV for the D6 ensemble is shifted with respect to the D8 and D10 curves by about 60 MeV. From the presently available data it can of course only be suspected that the trend of the shift prolongs towards smaller temperatures and results in an according shift in the pseudo-critical temperature for this ensemble with coarsest discretisation.

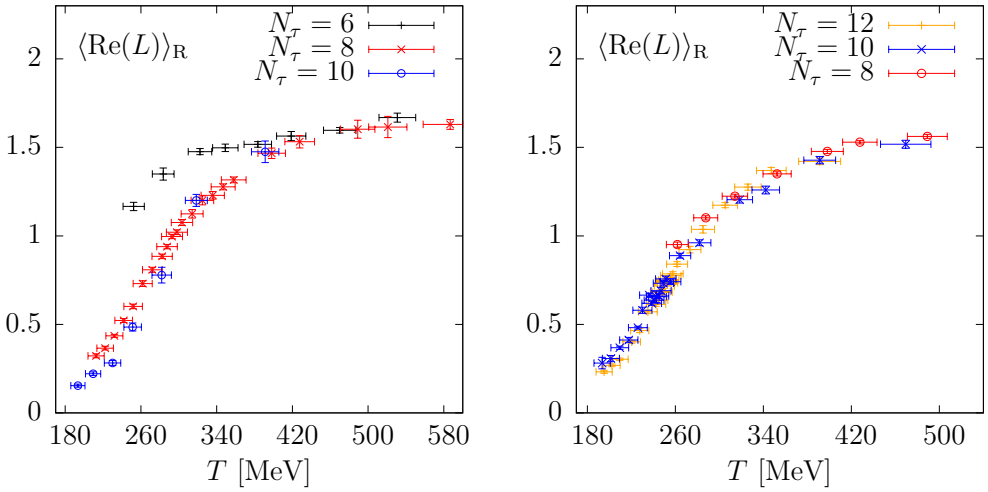

Figure 3.4: Renormalised Polyakov loop $\langle \mathrm{Re}(L)\rangle_R$ as a function of the temperature (scale setting method 2). **Left**: Data for the D ensembles with $N_\tau = 6, 8, 10$ is shown. **Right**: B ensembles with $N_\tau = 8, 10, 12$.

4 The Crossover Temperature

In this chapter the estimation of the pseudo-critical coupling β_c as well as the determination of the pseudo-critical temperature T_c from different observables is discussed. The location of T_c is at the basis for the study of the mass dependence towards the chiral limit that we will conduct in the chapter 5. We will show the β- and T-dependence of different observables and employ fits in order to infer the pseudo-critical couplings and temperatures and compare our findings for the mass dependence of the transition points with the results from other groups' two flavour studies of the phase transition. We start though by outlining the scale setting used in this work.

4.1 Setting the Temperature Scale

For the conversion of the bare coupling values to temperatures we make use of the scale setting done by the ETMC (Ref. [B$^+$10a]). The values of lattice spacings a that are presented in this reference are obtained from chiral fits to the lattice data fixing the pseudoscalar decay constant to its physical value at the physical pion mass. We have made use of two different methods for the conversion to temperature given the bare coupling β that will be described in the following.

- Method 1:
  Using the values of a for $\beta = 3.9, 4.05$ and 4.2 stemming from a combined chiral fit to lattice data at these coupling we can obtain the temperature in this interval of β by performing an interpolation of $a(\beta)$ and making use of Eq. (2.20). The interpolation has been obtained by L. Zeidlewicz [Zei11] and is shown in Fig. 4.1 (left).

- Method 2:
  We have enlarged the range of simulations beyond the interval covered by our first method to set the temperature scale described above, both towards lower and

Source	r_0 [fm]
ETMC [B$^+$10a]	0.420(15)

Table 4.1: Value of r_0 in femtometers used in this work for the conversion into physical units. The statistical and systematic errors reported in Ref. [B$^+$10a] have been added in quadrature.

higher values of the bare coupling. Therefore it was necessary to implement this second method to set the temperature scale with an increased range of validity. It uses an interpolation of the chirally extrapolated Sommer scale r_χ/a from a fit of the following ansatz to the lattice data:

$$\frac{r_\chi}{a}(\beta) = c_0 + c_1\beta + c_2\beta^2 \ . \tag{4.1}$$

The fit provides a good description with a value of $\chi^2/\mathrm{dof} = 1.05$ at six degrees of freedom. The quality of the interpolation is shown in Fig. 4.1 (right). In the figure we additionally show a point corresponding to the $T = 0$ simulation carried out at $\beta = 4.6$, where a chiral extrapolation could not yet be performed as no second quark mass is available. This point is not included in the fit of the interpolation. In order to obtain an error on the interpolation, we fit above expression added by a cubic term in β to the values of a 1-σ deviation from the according central value. Doing so with both the upper and the lower deviations and keeping the maximum of both as the error on the interpolation, we obtain the shaded grey error band shown in Fig. 4.1 (right).

In all cases (apart from $\beta = 3.65$) the error from our interpolation curve is slightly larger than the errors on the data points themselves. For evaluating the temperature from above interpolation of r_χ/a we calculate

$$T(\beta) \ \ [\mathrm{MeV}] = \frac{(r_\chi/a)\,(\beta)}{N_\tau \ \ r_0[\mathrm{fm}]} \times (\hbar c \ \ [\mathrm{MeV\ fm}]) \ , \tag{4.2}$$

using the value of r_0 given by the ETMC (see table 4.1) and adding all errors in quadrature to obtain the error on the temperature. In this way we end up with uncertainties on T that are of the order of 3-5 % in the range of $\beta = 3.65 - 4.35$ and are mostly dominated by the 3.6 % error on r_0.

We point out that the value of r_0 that is used here to convert to physical units has been obtained from lattice data at $\beta = 3.9$ and $\beta = 4.05$ only. It would be worthwhile to include more lattice data (being available now) into the chiral fits and into the determination r_0 in the future.

We conclude this section by stating that in the common interval in between $\beta = 3.9$ and $\beta = 4.2$ both our methods yield compatible values for the temperature, the first method giving more precise results (as the error of r_0 is larger than the errors for a).

4.2 Determination of T_c

In the range of pion masses we are currently focusing on it is expected that the type of the finite temperature transition is an analytic crossover. Lacking a true order parameter at intermediate pion masses in the range from 300 MeV to 700 MeV that are studied here, one is obliged to calculate and consider a variety of physical quantities. One has

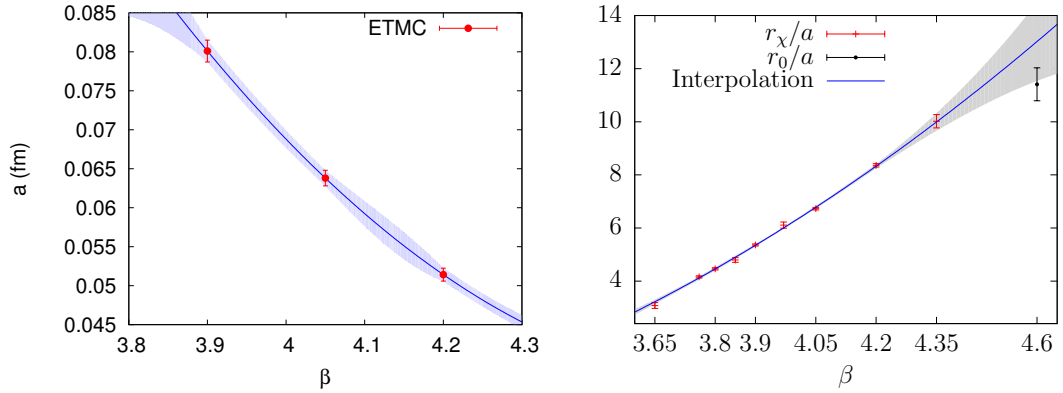

Figure 4.1: Left: Interpolation of $a(\beta)$ **Right**: Interpolation of r_χ/a in the bare coupling. The point at $\beta = 4.6$ is not obtained from a chiral extrapolation and is not included in the fit.

to look for (possibly simultaneous or nearby with respect to temperature) signalling behaviour in these. For an analytic crossover it is however not required that the critical temperatures T_c obtained from different observables agree at precisely the same value. This is why one often calls it the pseudo-critical temperature.

The observables we have investigated so far in order to locate the phase transition are those introduced in section 3. Unfortunately, the signal in the most easily computable gauge observables is small and we do not observe clear maxima to fix β_c in either of the susceptibilities of the gauge observables (c. f. Fig. 4.5 for the susceptibility of the bare Polyakov loop of B12 and Fig. 4.6 for A12 and C12), which have been mainly considered for the determination of β_c in Ref. [BIK$^+$11]. However, the disconnected part of the bare chiral susceptibility defined in Eq. (3.8) is showing the most pronounced as well as consistent signal throughout different pion masses and temporal extents N_τ of our simulation points. The peak in $\sigma^2_{\bar\psi\psi}$ can be fitted around the maximum by a Gaussian function

$$G(\beta) = a_G + b_G \cdot \mathrm{e}^{-c_G(\beta-\beta_c)^2} \ , \tag{4.3}$$

yielding a reasonable fit result. We are treating a_G, b_G, c_G as well as the critical coupling β_c as free parameters. In Fig. 4.2 and Fig. 4.3 we show such fits for the A12 and B12 ensembles and for the C12 and D8 ensembles, respectively. The pseudo-critical coupling is then converted to temperature using method 1 for A12, B12 and C12 and method 2 for D8. In table 4.2 we list our current estimates for β_c as well as the thereof calculated critical temperatures T_c.

In Fig. 4.4 we compare the unrenormalised chiral susceptibility $\sigma^2_{\bar\psi\psi}$ divided by the temperature squared (so a per se dimensionless quantity) among different lattice discretisations, i. e. among different N_τ for our B and D ensembles. As this quantity would need renormalisation (see e. g. Ref. [BBC$^+$12]) before being able to perform the continuum limit we note that the mere purpose of this comparison is to qualitatively estimate the effect of the finite cutoff on the location of T_c. Comparing the positions of the max-

Ensemble	A12	B12	C12	D8
Pion mass m_π[MeV]:	316(16)	398(20)	469(24)	690(33)
β_c from $\sigma^2_{\bar\psi\psi}$:	3.89(3)	3.93(2)	3.97(3)	3.78(1)
T_c[MeV] from $\sigma^2_{\bar\psi\psi}$:	202(7)	217(5)	229(5)	251(10)
T_c[MeV] from $\langle \mathrm{Re}(L)\rangle_R$:	-	249(5)	258(5)	266(11)

Table 4.2: Extracted (pseudo-) critical couplings β_c from fits to the maximum of the chiral susceptibility as well as according temperatures T_c. Another estimate for T_c as originating from a fit to the renormalised Polyakov loop is also shown where available. Furthermore the simulated pion mass (corresponding to the charged pion as obtained from ETMC data alone) is listed. We have converted to physical units by means of method 1 for A12, B12 and C12 and using method 2 for D8.

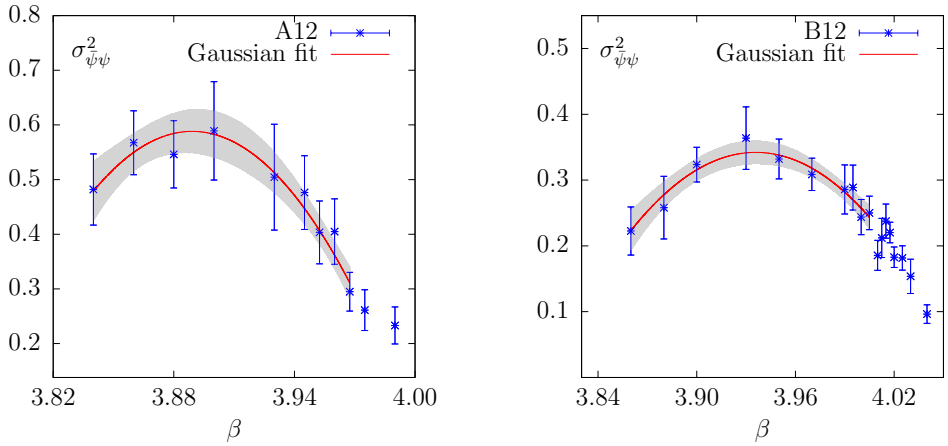

Figure 4.2: Results for the susceptibility of $\bar\psi\psi$, $\sigma^2_{\bar\psi\psi}$, in the critical β region with Gaussian fit: **Left**: for ensemble A12, **Right**: for ensemble B12.

imum of the susceptibility for $N_\tau = 8$ and $N_\tau = 10$ for the D ensemble we observe it to lie approximately at the same temperature while the falling edge of the susceptibility for $N_\tau = 6$ appears to be shifted to lower temperatures suggesting again a smaller T_c for the coarsest discretisation. This is in accord with what has been observed for the renormalised Polyakov loop (c. f. Fig. 3.4). From comparing the maxima of the chiral susceptibility for the B ensembles we conclude that for $N_\tau = 10$ and 12 the peak region seems to coincide around $T = 220$ MeV (although it can be clearly seen that the $N_\tau = 10$ points still need some improvement in terms of statistics). From the falling edge that is yet accessible by our B8 simulations we are even lead to believe that for $N_\tau = 8$ lattice artifacts are not too big as to give rise for a shift in T_c. Although, obviously, smaller temperatures are needed to resolve the maximum.

For the ensembles B12, C12 and D8 an additional way of extracting T_c based on another observable is possible. As the data for the renormalised Polyakov loop is robust enough and shows an s-shape behaviour for these ensembles with reasonably small errors

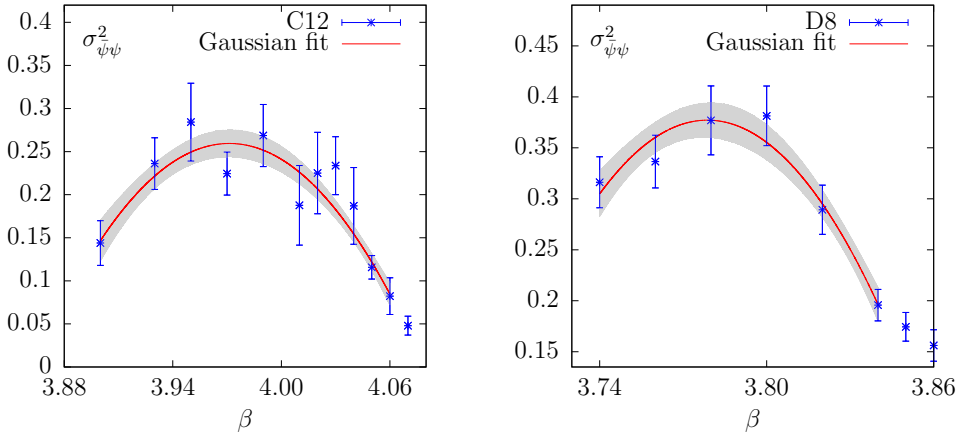

Figure 4.3: Results for the susceptibility of $\bar\psi\psi$, $\sigma^2_{\bar\psi\psi}$, in the critical β region with Gaussian fit: **Left**: for ensemble C12, **Right**: for ensemble D8.

we have fitted the following ansatz:

$$S(T) = a_S + b_S \cdot \tanh\left(c_S(T - T_c)\right) \tag{4.4}$$

to $\langle \mathrm{Re}(L)\rangle_R$ with a_S, b_S, c_S and T_c being free parameters. For B12 and D8 we attain reasonable fits with χ^2 per degree of 1.6 and 1.1, respectively. For C12 the fit is slightly inferior producing $\chi^2/\mathrm{dof} = 2.0$. The considered fit ranges have been 195 MeV $\leq T \leq$ 392 MeV, 208 MeV $\leq T \leq$ 327 MeV and 212 MeV $\leq T \leq$ 400 MeV for B12, C12 and D8, respectively. In the fits we consider solely the error on $\langle \mathrm{Re}(L)\rangle_R$ and neglect the error of the temperature. The uncertainty for T_c from the fits (in all cases $1-2$ MeV) are then added to the uncertainty of the temperature scale at the fitted T_c in quadrature, which yields the uncertainties on T_c shown in Table 4.2. For the fits to B12 and C12 we have used the scale setting from $a(\beta)$ (method 1) while for the fit to the D8 data we have employed the scale setting based on $\left(\frac{r_X}{a}\right)(\beta)$ (method 2). Comparing the thus obtained values for T_c with the estimates from the bare susceptibility of $\bar\psi\psi$ we observe that it is significantly shifted to higher values in each case with the difference becoming smaller for larger pion mass. It is worthwhile to compare the couplings that correspond to the fitted T_c values to the range in β we have assigned to the location of the crossover transition from the study of different bare gauge observables alone [BIK+11]. Shaded bands in the left panel of Fig. 4.5 mark these ranges as well as in Fig. 4.6, where the susceptibility of the Polyakov loop is shown. This observable shows a shoulder-like behaviour within the marked region for all considered pion masses, although with low significance, admittedly. We remark however that for B12 and C12 the indicated coupling ranges agree with the pseudo-critical couplings ($\beta_c \sim 4.025$ for B12 and $\beta_c \sim 4.05$ for C12) which we infer from the fitted T_c of the analysis of the renormalised Polyakov loop.

From the overall noisiness of our signals and even more from the fact that the location of T_c differs for observables related to confinement and chiral symmetry (which is also seen e. g. by the Budapest-Wuppertal group for the case of $N_f = 2+1$, see e. g. Ref.

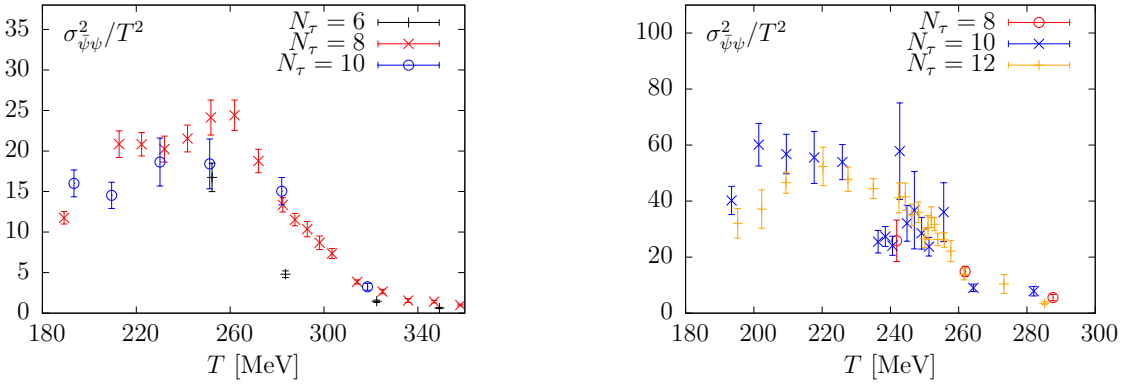

Figure 4.4: Comparison of the peak region of the disconnected chiral susceptibility $\sigma^2_{\bar{\psi}\psi}/T^2$ as a function of temperature among different discretisations of the temporal direction (different N_τ). Data is not renormalised such that the comparison is on a qualitative level in order to check the N_τ dependence of the maximum of this observable. **Left**: Data from the D ensembles is shown at $N_\tau = 6, 8$ and 10. **Right**: Data from the B ensembles is shown at $N_\tau = 8, 10$ and 12.

[AFKS06]) we conclude that in the range of masses we are investigating we observe no true phase transition actually but merely a weak crossover. The QCDSF-DIK collaboration [BHM$^+$10, BHN$^+$11] who have studied the finite temperature transition with two flavours of light Wilson (clover-improved) quarks however report that the location of the chiral and deconfinement transition signals coincide for their investigation. In contrast to our approach however, scans in κ (i. e. in both mass and temperature) instead of scans in β (i. e. in the temperature) are used there. It might be interesting to consider also mass scans (i. e. in $a\mu$) for our setup in the future. One could thus check for a possible coincidence of T_c from different observables. If we consider for the moment T_c as extracted from the chiral susceptibility, we already find that the location of our data within the temperature mass plane is in accord with the data of the QCDSF-DIK collaboration (Fig. 4.7 (left)) and a universal curve is found.

In Fig. 4.7 (right) we compare the critical temperature from $\sigma^2_{\bar{\psi}\psi}$ as a function of the ratio $(m_{\mathrm{PS}}/m_{\mathrm{V}})^2$ with findings by the CP-PACS collaboration [AK$^+$01a] from simulations with $N_f = 2$ clover-improved Wilson fermions. To do so we have interpolated for the D8 ensemble m_{V} in between the two values of β surrounding β_c. The mean and error of $(m_{\mathrm{PS}}/m_{\mathrm{V}})^2$ are obtained from a constant fit to this quantity over the whole range of available couplings. The latter is justified as the vector and pseudoscalar mass ratio is constant within errors (see also discussion in section 6.6). The interpolations needed for the A12, B12 and C12 point have been carried out using data for am_{V} obtained from $T = 0$ ETMC lattices at $\beta = 3.9$ and $\beta = 4.05$ (personal communication with M. Petschlies). For the interpolation in $a\mu$ a linear fit ansatz has been used which is compatible with the data. We then interpolate am_{V} linearly in β to β_c. The uncertainty of the interpolation related to β_c is added in quadrature to the interpolated statistical error

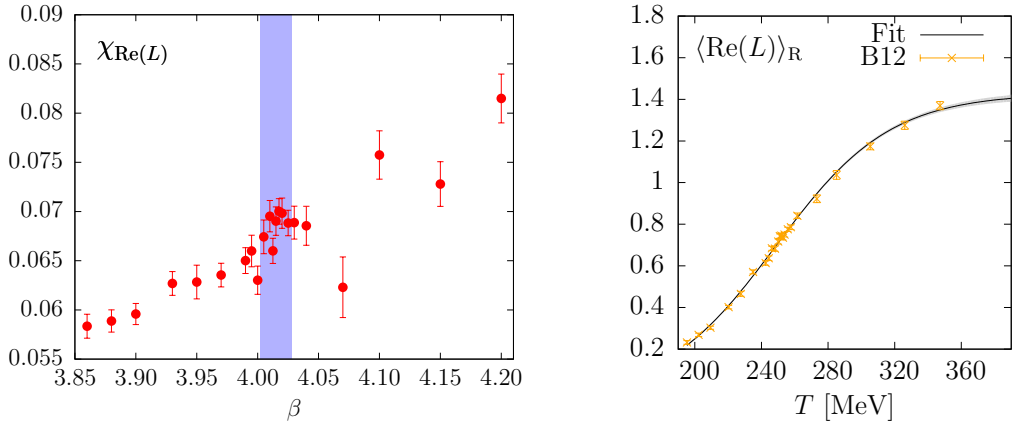

Figure 4.5: Left: The susceptibility of the bare Polyakov loop for the B12 ensemble. The vertical shaded band corresponds to the range in β that has been identified as the location of the crossover from the study of different gauge observables. **Right**: The renormalised Polyakov loop for B12 with a fit to Eq. (4.4) for the determination of T_c.

of am_{V}. To this end β_c is varied by one standard deviation and the maximal deviation of the interpolated mass from the central value is regarded as the associated error.

In general, our data is in the whole compatible with the curve spanned by the CP-PACS data. However, it seems to slightly undershoot it at $N_\tau = 12$ towards small mass ratio. As the CP-PACS results were obtained at $N_\tau = 4$ however, this effect might be suspected to be caused by lattice artifacts.

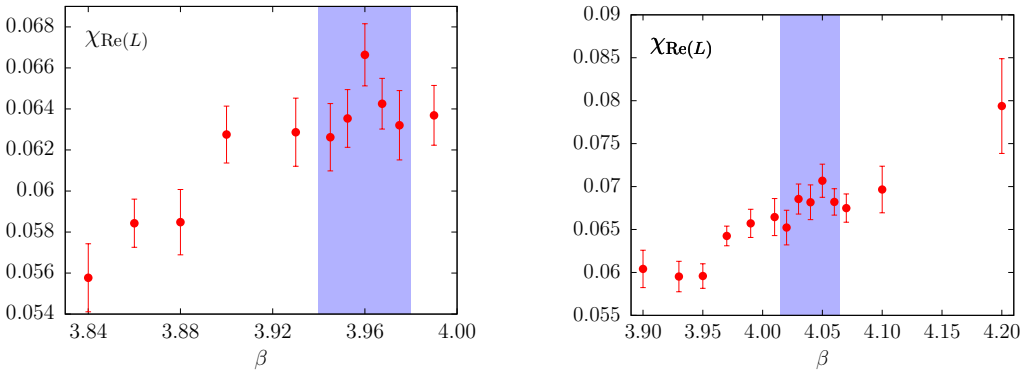

Figure 4.6: **Left**: The susceptibility of the bare Polyakov loop for the A12 ensemble. The vertical shaded band corresponds to the range in β that has been identified as the location of the crossover from the study of different gauge observables. **Right**: The same for C12.

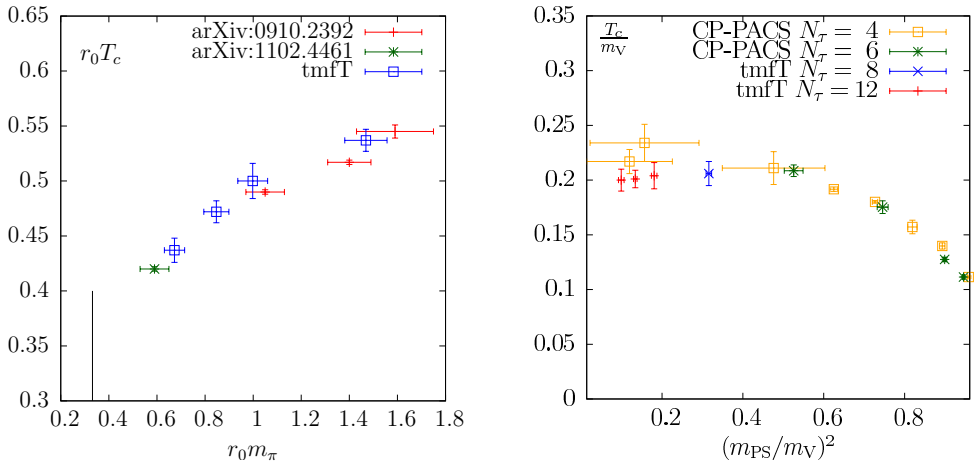

Figure 4.7: Comparison of our findings for the quark mass dependence of the critical temperature. **Left**: Comparison of $r_0 T_c$ with the findings of the QCDSF-DIK collaboration Ref. [BHM+10, BHN+11]. **Right**: Comparison of T_c/m_{V} with results from the CP-PACS collaboration Ref. [AK+01a]. Our points for the critical temperature labelled with tmfT are results obtained from the maximum of the chiral susceptibility.

5 Investigation of the Chiral Limit

The QCD Lagrangian (Eq. (2.1)) in its massless limit is invariant under separate rotations of left- (L) and right-handed (R) field components (c. f. [PS95]),

$$\begin{aligned} &\psi_L^f \equiv \frac{1}{2}\left(\mathbb{1}-\gamma_5\right)\psi^f \qquad && \psi_R^f \equiv \frac{1}{2}\left(\mathbb{1}+\gamma_5\right)\psi^f \\ &\psi_L^f \to \left(\mathrm{e}^{i\alpha_L^a\tau^a}\right)^{fg}\psi_L^g \qquad && \psi_R^f \to \left(\mathrm{e}^{i\alpha_R^a\tau^a}\right)^{fg}\psi_R^g \\ &\text{and} \\ &\psi_L^f \to \left(\mathrm{e}^{i\alpha_L}\right)\psi_L^f \qquad && \psi_R^f \to \left(\mathrm{e}^{i\alpha_R}\right)\psi_R^f\,, \end{aligned} \tag{5.1}$$

which is known under the name of chiral symmetry. Associated with this invariance is the following global symmetry pattern:

$$SU(N_f)_V \times SU(N_f)_A \times U(1)_V \times U(1)_A \tag{5.2}$$

under vector (V) and axial (A) transformations for $\alpha_R^{(a)} = \alpha_L^{(a)}$ and $\alpha_R^{(a)} = -\alpha_L^{(a)}$, respectively. Clearly, above symmetries are broken explicitly for finite quark masses, but they are at least realised approximately for small quark masses i. e. if one considers only the three (or even only the two) lightest quarks. While the vector symmetries are intact symmetries associated with the observed baryon number conservation the axial $SU(N_f)_A$ symmetry is broken spontaneously at $T = 0$. This is indicated by a non-vanishing value of the chiral condensate $\left\langle\bar{\psi}\psi\right\rangle$ (Eq. (3.6)) acting as the corresponding order parameter. The $U(1)_A$ symmetry (although exact in the $m_f = 0$ classical case) is broken dynamically by the anomaly, the associated Noether current $j_5^\mu = \bar{\psi}\gamma^\mu\gamma_5\psi$ being non-conserved by the density of instantons [PS95]:

$$\partial_\mu j_5^\mu = -\frac{g^2 N_f}{32\pi^2}\epsilon^{\mu\nu\rho\sigma}F_{\mu\nu}^c F_{\rho\sigma}^c\,. \tag{5.3}$$

Hence if at $T > 0$ the axial $U(1)_A$ is sufficiently broken, the symmetry breaking pattern for $N_f = 2$ is

$$SU(2)_V \times SU(2)_A \to SU(2)_V\,, \tag{5.4}$$

and thus the finite temperature transition, if of second order in the chiral limit, would belong to the universality class of an $O(4)$ spin model [PW84] as $SU(2)\times SU(2) \simeq O(4)$. However, as argued in the same reference, $U(1)_A$ should be restored at high temperatures and might even be restored at temperatures below the restoration of $SU(N_f)_A$. In this case a first order transition could be realised. Because simulations at zero quark mass are

Universality class	$\tilde{\beta}$	γ	δ	Reference
$O(4)$	0.38	1.45	4.86	Ref. [EM00]
$Z(2)$	0.3265	1.2372	4.789	Ref. [PV02]

Table 5.1: Critical exponents for various chiral scenarios.

impossible, the general strategy of investigation is to collect data at a set of temperatures and masses and to try to observe universal behaviour of observables as expected in the vicinity of a critical point of a second order phase transition. This behaviour is common to all systems sharing the same dimensionality and symmetries and is encoded in the respective critical exponents.

5.1 The Magnetic Equation of State

According to what has been said above the temperature and external field dependence of the order parameter M ($\langle\bar{\psi}\psi\rangle$ for chiral symmetry in QCD) is governed by a universal scaling function f_G in the vicinity of the critical point. In terms of the scaling variable z and the critical exponents $\tilde{\beta}$ and δ it can be written as

$$M(\tau, h) = h^{1/\delta} f_G(z) \qquad z = \frac{\tau}{h^{1/(\tilde{\beta}\delta)}} \ . \tag{5.5}$$

f_G is sometimes called the magnetic equation of state (mEoS). The normalised and reduced temperature τ is thereby defined as

$$\tau = \frac{1}{T_0} \frac{T - T_c}{Tc} \ , \tag{5.6}$$

and h corresponds to the normalised external symmetry breaking field. In the case of a spin model the role of h is played by an external magnetic field H, in the case of QCD it is played by the quark mass

$$h = \frac{H}{H_0} \ . \tag{5.7}$$

According to Eq. (5.5) the behaviour of the combination $M/h^{1/\delta}$ is universal as long as the system is in the proximity of the critical point and thus this combination should be investigated. The explicit form of the scaling function $f_G(z)$ is known for a variety of spin models and for the case of the three-dimensional $O(4)$ model a full parametrisation of f_G has been given in Ref. [EM00]. The critical exponents γ, δ and $\tilde{\beta}$ which enter f_G are listed for reference in Table 5.1. The scaling function Eq. (5.5) incorporates the following limits, that are known from the definition of the critical exponents $\tilde{\beta}$ and δ:

$$M \sim h^{1/\delta} \qquad \tau = 0 \tag{5.8}$$

and in the phase with broken symmetry:

$$M \sim |\tau|^{\tilde{\beta}} \qquad h = 0 \; . \tag{5.9}$$

The first limit is obvious from the fact that $f_G(0) = 1$. In order to verify the second limit one should consider a fixed small $z < 0$ (in order to be in the broken phase) and take the limit $h \to 0$. This results in $\tau \sim h^{1/(\tilde{\beta}\delta)}$. As f_G is constant (z being held fixed) we see by substituting h into the prefactor that $M \sim |\tau|^{\tilde{\beta}}$.

As the correct normalisation of τ and h taking effect in Eqs. (5.6) and (5.7) are not known for the QCD case we define the reduced temperature (represented by the reduced coupling) as

$$\tau = (\beta - \beta_{\text{chiral}}) \tag{5.10}$$

as well as the breaking field (given by the quark mass) as

$$h = 2a\mu \tag{5.11}$$

without these normalisations. Then these normalisations are to be treated as multiplicative factors of f_G and its argument that both have to be fitted when confronting numerical QCD data with Eq. (5.5).

Investigations of fits to the universal scaling function have for instance been carried out in Refs. [AK$^+$01b, EKL$^+$09]. The authors of Ref. [EKL$^+$09], who were using $N_f = 2 + 1$ staggered fermion simulations for the comparison, have found it necessary to include several correction terms to the scaling function in order to be able to describe the numerical data sufficiently.

In our analysis we adopt the same strategy and add three correction terms to f_G:

$$\left\langle \bar{\psi}\psi \right\rangle = c \; h^{1/\delta} f_G(d \; z) + a_\tau \; \tau \; h + b_1 h + b_3 h^3 \; , \tag{5.12}$$

where the normalisation constants c and d discussed earlier as well as a_τ, b_1 and b_3 have to be adjusted by the fit.

In the following we present fit results of the mEoS to lattice data as has been already shown by the tmfT collaboration in Ref. [BIK$^+$11] but with less precise data for the order parameter. For the fits we use an implementation of f_G as found in Ref. [EM00] due to L. Zeidlewicz. We employ the optimisation routine *optim* provided by R [R D10] for the minimisation of the χ^2-function.

In Table 5.2 we give a representative list of our fit results for different combinations of data that is included in the fit as well as for different combinations of scaling violating terms that are imposed. We have restricted the fits to data lying in the intervals from $\beta = 3.83$ (3.85, 3.89) to $\beta = 3.97$ (4.03, 4.04) for A12 (B12, C12), which means that we are not fitting the complete range of available data. One reason for this is that we have not covered the same range of temperatures (measured as a fraction of T_c) for the different pion masses we are studying. For instance in the case of B12 (partly also C12) we have more data at larger temperature at our disposition. The second reason is that with broader fit range we expect the scaling violating terms to become more and more

dominant and it may be doubted that the leading order violation terms in Eq. (5.12) are sufficient to describe the violations of scaling. Indeed we find substantially larger values for χ^2 per degree of freedom if we include the whole range of available data into the fits. If some of the fit parameters have been treated as fixed input, the corresponding numbers are marked in bold face in Table 5.2. For fits No. 8-10 we have e. g. fixed the critical coupling in the chiral limit to $\beta_{\text{chiral}} = 3.73$ in order to reduce the number of fit parameters. We have chosen this specific value as this is the value of β_{chiral} that is favoured given our results for the pseudo-critical couplings β_c, if we study the scaling with respect to the mass (see the forthcoming section 5.2).

As an example we show fit No. 11 in the left panel of Fig. 5.1. In this fit we include A12, B12 and C12 data and fit all three scaling violating terms presented in Eq. (5.12). Due to the violation of scaling, points corresponding to different ensembles are shifted with respect to one another. If we however subtract the fitted scaling violating terms from the order parameter, we expect the thus corrected values to lie on a universal curve given by the mEoS. That this expectation is indeed true is nicely depicted in the right panel of Fig. 5.1, where we show the data from fit No. 11 corrected for the fitted scaling violating terms.

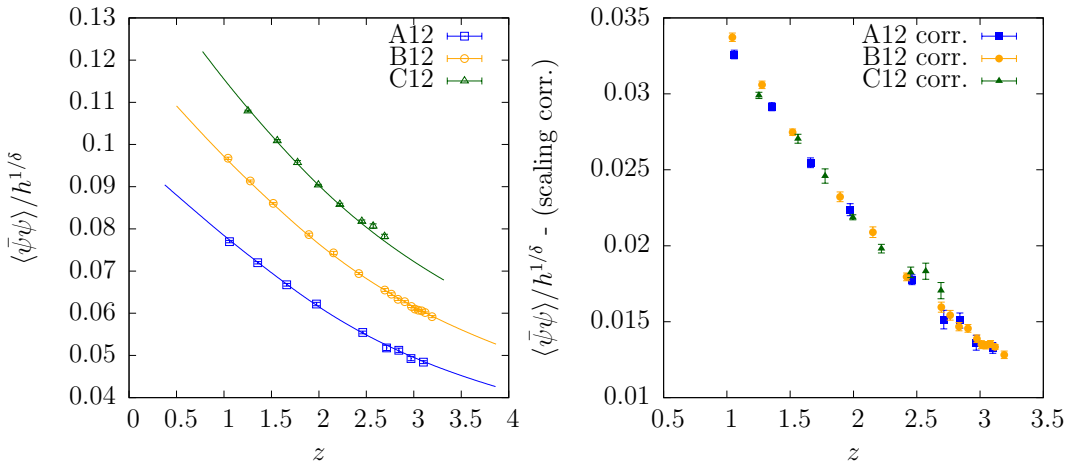

Figure 5.1: Left: Fit of the magnetic equation of state Eq. (5.12) to the order parameter $\langle\bar{\psi}\psi\rangle$. The fit shown includes the ensembles A12, B12 and C12 and corresponds to fit No. 11. **Right**: The order parameter corresponding to the same fit after subtraction of the fitted scaling violating terms. As expected, the so corrected data follows a universal behaviour dictated by the mEoS.

5.2 Comparison of Chiral Scenarios

From the scaling function for the order parameter M (Eq. (5.5)) it is possible to derive the dependence of the pseudo-critical coupling on the symmetry breaking field h [Kar94]. First we observe that with Eq. (5.5) a similar scaling function for the susceptibility of

No	Data	β_{chiral}	d	c	a_τ	b_1	b_3	χ^2/dof
1	A	3.57(4)	0.367(7)	0.14(2)	**0**	**0**	**0**	0.43
2	B	3.40(5)	0.36(2)	0.22(4)	**0**	**0**	**0**	0.64
3	C	3.12(2)	0.39(2)	0.42(3)	**0**	**0**	**0**	2.42
4	A,B	3.368(6)	0.383(5)	0.257(6)	**0**	**0**	**0**	3.31
5	A,B	3.48(2)	0.48(2)	0.225(6)	0.7(1)	**0**	**0**	2.2
6	A,B	3.57(2)	0.53(2)	0.152(7)	**0**	0.90(6)	**0**	1.75
7	A,B	3.82(4)	1.1(2)	0.028(9)	-2.2(2)	2.49(8)	**0**	0.42
8	A,B	**3.73**	0.825(8)	0.1279(8)	4.01(4)	**0**	**0**	76
9	A,B	**3.73**	0.81(2)	0.0759(7)	**0**	1.61(2)	**0**	7.2
10	A,B	**3.73**	0.74(2)	0.053(2)	-1.8(2)	2.23(6)	**0**	0.63
11	A,B,C	3.76(2)	0.83(6)	0.047(6)	-1.5(2)	2.20(6)	50(11)	1.8

Table 5.2: Results for the fits of the scaling function (mEoS) Eq. (5.12) to the chiral condensate including different scaling violating terms. Numbers in bold face have been fixed in the fit.

the order parameter χ (corresponding to Eq. (3.9) in the case of QCD) exists:

$$\chi = \frac{\partial M}{\partial h} = h^{1/\delta-1}\left(\frac{1}{\delta}f_G(z) - f_G'(z)z\right) \equiv h^{1/\delta-1}F(z)\ . \tag{5.13}$$

As χ develops a peak at the pseudo-critical coupling β_c, the derivative of χ with respect to τ has to vanish:

$$\frac{1}{h^{1/\delta-1}}\frac{\partial\chi}{\partial\tau} = \frac{1}{h^{1/(\tilde{\beta}\delta)}}F'(z) \stackrel{!}{=} 0\ . \tag{5.14}$$

This condition can only be realised for general h for a constant argument to the scaling function F, i. e. $z \equiv B$. Together with the definition of z (Eq. (5.5)) we arrive at a relation between the pseudo-critical coupling $\beta_c(h)$ and the external field h for a second order phase transition point in the chiral limit:

$$\beta_c(h) = \beta_{\text{chiral}} + B\ h^{1/(\tilde{\beta}\delta)}\ , \tag{5.15}$$

which upon converting to physical units is equivalent to

$$T_c(m_\pi) = T_c(0) + A\ m_\pi^{2/(\tilde{\beta}\delta)}\ . \tag{5.16}$$

Here we have made use of the leading result of chiral perturbation theory $m_\pi^2 \propto m_q$. The distinction between different universality classes is introduced by different critical exponents in Eqs. (5.15) and (5.16). These equations are however only true given a second order phase transition in the chiral limit. One might think of various other scenarios for vanishing mass, though. For instance, one could imagine a first order transition in the chiral limit turning into a second order critical end point of universality class of an Ising $Z(2)$ spin model at a finite value of the pion mass $m_{\pi,c}$. Such a scenario would correspond to the scenario at the opposite side of the mass range for

$m_\pi \to \infty$ (i. e. the upper right corner of Fig. 1.1 (right)). This means that critical scaling according to Eq. (5.16) would only set in at pion masses larger than $m_{\pi,c}$ amounting to the replacement of $m_\pi^2 \to (m_\pi^2 - m_{\pi,c}^2)$ in this relation. Another possibility is the case $m_{\pi,c} = 0$ corresponding to a $Z(2)$ critical point directly in the chiral limit. We have listed the critical exponents relevant to this case in Table 5.1. Although scaling arguments do not apply to first order transitions, there are studies of the two-flavour QCD transition supposing a first order transition in the chiral limit making use of the scaling formula Eq. (5.16) and the first order combination of exponents $1/(\tilde{\beta}\delta) = 1$ [CCD$^+$06, BHM$^+$10]. We have also included this case in our study of the chiral limit.

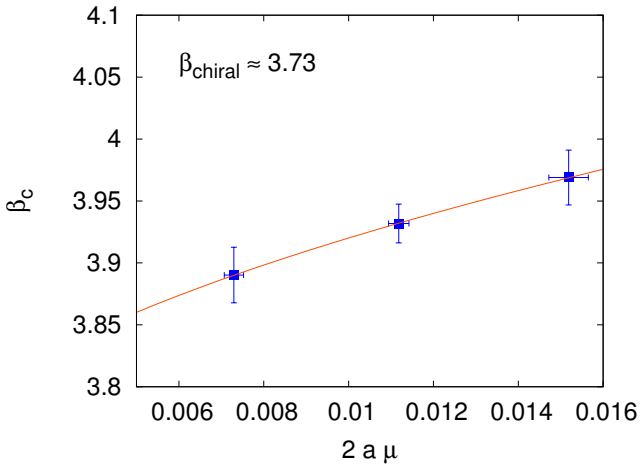

Figure 5.2: Fit of the pseudo-critical couplings β_c to Eq. (5.15).

Both scaling formulae (Eq. (5.15) and Eq. (5.16)) for the mass dependence of the critical coupling (temperature) have been confronted with our lattice determinations of β_c (T_c) corresponding to the available $N_\tau = 12$ ensembles A12, B12 and C12. In both cases we are dealing with fits of two parameters to three data points, treating β_{chiral} and B ($T_c(0)$ and A) as adjustable parameters. Fig. 5.2 shows a fit of the numerically found β_c dependence for a chiral $O(4)$ scenario which gives the prediction

$$\beta_{\text{chiral}} = 3.73(9)$$

for the $O(4)$ critical coupling in the chiral limit. The central value given above has been used as an input to the mEoS in the previous paragraph. The error on the x-axis arises from the uncertainty in $a\mu$ (being varied with β) as induced by the uncertainty in β_c and is taken into account in the fit.

In Fig. 5.3 we show a comparison of the performance of different chiral scenarios as discussed above. For the $Z(2)$ assumption we have tested $m_{\pi,c} = 0$ MeV as well as $m_{\pi,c} = 200$ MeV. As can be appreciated from the figure our current data is not yet capable of discriminating between the different scenarios. Further, possibly lower masses should be added in future in order to make a distinction possible.

For the $O(4)$ scenario with only $N_\tau = 12$ data at the three smallest quark masses

included in the fit we obtain for the chiral critical temperature:

$$T_c(0) = 152\ (26)\ \text{MeV}\ ,$$

while for the other scenarios somewhat larger values are preferred. We find values of χ^2/dof in the range of $0.01 - 0.1$ for these fits. The error of above estimate of $T_c(0)$ includes both the x- and the y-errors of the fitted data via a bootstrap analysis assuming these errors to be independent (which actually is not true, as in both cases the error includes the error from the scale setting). If we include the D8 point in the fit for the $O(4)$ scenario we obtain the value

$$T_c(0) = 168\ (14)\ \text{MeV}$$

for the $O(4)$ scenario. The other scenarios produce again slightly larger values. But the application of leading order chiral perturbation theory implicitly used in Eq. (5.16) might not be justified for the large pion mass of the D8 run. Thus we would consider this result to be based on a weaker footing than the above. However, also in this case we find acceptable χ^2/dof in the range of $0.5 - 1.3$.

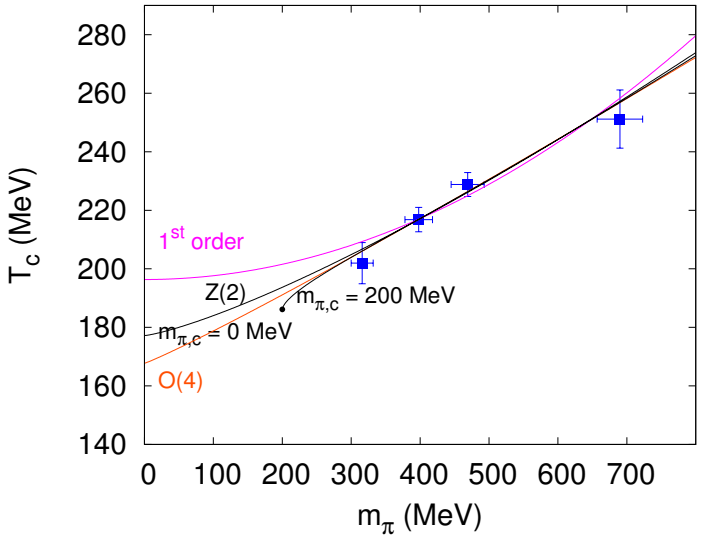

Figure 5.3: Comparison of different chiral scenarios for the mass dependence of the pseudo-critical temperature. We show the fit with included D8 point. From the present available data a discrimination between the possible scenarios is not possible yet.

6 The Thermodynamic Equation of State

The thermodynamic equation of state (EoS) of the hot medium in the temperature region around the transition is important for the description of the expansion of the plasma in terms of relativistic hydrodynamics equations. It can be provided by lattice QCD studies and has been evaluated by several groups within different setups. A recent overview on the status of the field is given in Ref. [Phi12]. So far there are only few results for the EoS from Wilson type of discretisations, most notably an $N_f = 2+1$ calculation at a mass of the pion of ~ 630 MeV [U$^+$10, U$^+$12] using the so-called fixed-scale approach [UEA$^+$09]. For $N_f = 2$ with Wilson fermions results for the EoS are available at considerably coarse lattices at $N_\tau = 4$ and 6 from Ref. [AK$^+$01a]. The most advanced calculations have been done within the framework of $N_f = 2 + 1$ staggered quarks at physical masses and as alluded to in the introduction are exhibiting inconsistencies at present.

In the following the determination of the thermodynamic EoS will be discussed for the here present two flavour Wilson twisted mass case. After having given a definition of the basic quantities we are considering in section 6.1, we will focus on how these quantities are accessible on the lattice at the basis of the trace anomaly in section 6.2. In section 6.3 a discussion on the determination of the β-functions needed in the calculation of the trace anomaly will be added. The Stefan-Boltzmann limiting case of free bosonic and fermionic quantum gases as well as lattice corrections will be considered in section 6.4. The ratio of the lattice to the continuum result for the pressure will serve to correct the results for the trace anomaly for lattice artifacts in section 6.7. There we will also present the main results for the trace anomaly and the derived thermodynamic EoS. Some preliminary results for the trace anomaly have already been presented in Ref. [Phi12]. We will furthermore discuss the continuum limit of the trace anomaly and check for finite size effects at two values of the temperature of the D mass ensemble. In sections 6.5 and 6.6 some technical details about the $T = 0$ subtraction of the trace anomaly and the achieved quality of how a line of constant physics has been followed by our simulations will be given, respectively. We close the chapter by a brief comparison of the precision of our evaluation of the trace anomaly to an evaluation that is using staggered quarks.

6.1 Basic Thermodynamics

In this paragraph we want to give the reader a brief introduction to the basic quantities of thermodynamics that form the basis of the present work. Being discussed in most of the introductory textbooks on statistics and thermodynamics, we rely in the following on the discussion given in the book of Yagi et al. [YHM05].

The quantum grand-canonical partition function represents a natural starting point for the study of a thermodynamic system held at fixed external temperature T and volume V allowing for particle number fluctuations controlled via chemical potential $\tilde{\mu}$

$$\begin{aligned} \Xi(T, V, \tilde{\mu}) &= \mathrm{Tr}\left(e^{-(\hat{H}-\tilde{\mu}\hat{N})/T}\right) \\ &\equiv e^{-\Omega(T,V,\tilde{\mu})/T} , \end{aligned} \tag{6.1}$$

where Ω is the associated thermodynamic potential (the grand potential) and $\hat{\rho}$ is the quantum density operator defined in terms of the quantum Hamilton operator $\hat{H}$ and the quantum particle number operator $\hat{N}$ as

$$\hat{\rho} = \frac{1}{\Xi} e^{-(\hat{H}-\tilde{\mu}\hat{N})/T} . \tag{6.2}$$

By construction $\hat{\rho}$ has unit expectation value $\mathrm{Tr}\hat{\rho} = 1$. Thermodynamic expectation values of observables $\hat{O}$ are defined in the usual way in terms of $\hat{\rho}$:

$$\langle O \rangle = \mathrm{Tr}(\hat{\rho}\hat{O}) . \tag{6.3}$$

With the definitions of the average system energy E, the average particle number N and the average entropy S,

$$E = \left\langle \hat{H} \right\rangle \quad N = \left\langle \hat{N} \right\rangle \quad S = \left\langle \hat{S} \right\rangle = -\mathrm{Tr}(\hat{\rho} \ln \hat{\rho}) , \tag{6.4}$$

the following thermodynamic relations hold for the grand potential and its infinitesimal variation:

$$\begin{aligned} \Omega(T, V, \tilde{\mu}) &= E - TS - \tilde{\mu}N \\ d\Omega &= -S\ dT - p\ dV - N\ d\tilde{\mu} , \end{aligned} \tag{6.5}$$

where the pressure p is defined as

$$p = -\left.\frac{\partial \Omega}{\partial V}\right|_{T,\tilde{\mu}} . \tag{6.6}$$

As the volume V is the only extensive quantity, the extensive quantity Ω depends on, Ω must be proportional to V:

$$\Omega = -pV \tag{6.7}$$

and together with Eq. (6.1) we arrive at

$$\frac{p}{T} = \frac{1}{V} \ln \Xi . \tag{6.8}$$

As explained in section 2.4, the partition function Eq. (2.16) is equivalent to the grand-canonical partition function Ξ at $\tilde{\mu} = 0$ with finite temperature T imposed externally

upon the system via a shortened (Euclidean) time-like direction, i. e.

$$\Xi \equiv Z \ . \tag{6.9}$$

The pressure p and energy density ϵ defined as

$$\epsilon = \frac{E}{V} \tag{6.10}$$

can be obtained from derivatives of the grand-canonical partition function (from here on we impose $\tilde{\mu} = 0$) as follows:

$$\begin{aligned} \epsilon &= \frac{T}{V} \frac{\partial \ln Z}{\partial \ln T}\bigg|_V \\ p &= T \ \frac{\partial \ln Z}{\partial V}\bigg|_T \end{aligned} \tag{6.11}$$

It is obvious, that the evaluation of both these quantities from lattice calculations is problematic, as $V = N_s^3 a^3$ and $T = 1/(N_\tau a)$ are not independent (both depending on the bare parameter β). However, Eq. (6.11) requires to vary either T or V while keeping fixed the other one. Therefore, the evaluation of p and ϵ is usually performed by employing the quantity $\epsilon - 3p$, the so-called trace anomaly, in an intermediate step of the calculation. Being a total derivative in the lattice spacing a, as will be shown in the next paragraph it is a quantity easier to evaluate on the lattice. It allows for the calculation of pressure and energy density in a subsequent step.

Another observable of phenomenological interest derivable from the basic bulk thermodynamic quantities p and ϵ is the velocity of sound of the hot medium which is defined as the derivative of the pressure with respect to the energy density

$$c_s^2 = \frac{dp}{d\epsilon} \tag{6.12}$$

and may be calculated from the ratio p/ϵ by means of the following identity [CEH$^+$10]:

$$\frac{dp}{d\epsilon} = \epsilon \frac{d(p/\epsilon)}{d\epsilon} + \frac{p}{\epsilon} \ . \tag{6.13}$$

6.2 The Trace Anomaly

For the calculation of the temperature dependence of pressure $p(T)$ and energy density $\epsilon(T)$ we will employ the integral method (see e. g. [DH09]). The basic quantity one has to compute in this case is the trace anomaly (sometimes called interaction measure)

$$I = \epsilon - 3p = -\frac{T}{V} \frac{d \ln Z}{d \ln a} \ . \tag{6.14}$$

That this can be written as a total derivative with respect to the lattice spacing a becomes obvious if we consider for a moment an anisotropic lattice with separate lattice spacings in the time-like (a_τ) and space-like (a_σ) lattice directions. The evaluation of thermodynamic derivatives then proceeds as:

$$\begin{aligned}\left.\frac{\partial}{\partial T}(\ldots)\right|_V &= \left.\frac{\partial}{\partial(1/(N_\tau a_\tau))}(\ldots)\right|_V \\ &= -(N_\tau a_\tau)^2 \frac{1}{N_\tau}\left.\frac{\partial}{\partial a_\tau}(\ldots)\right|_{a_\sigma} \\ &= -\frac{1}{T} a_\tau \left.\frac{\partial}{\partial a_\tau}(\ldots)\right|_{a_\sigma}\end{aligned} \tag{6.15}$$

and

$$\left.\frac{\partial}{\partial V}(\ldots)\right|_T = \frac{1}{3V} a_\sigma \left.\frac{\partial}{\partial a_\sigma}(\ldots)\right|_{a_\tau} . \tag{6.16}$$

Employing the definitions of pressure and energy density (Eq. (6.11)) we have

$$\begin{aligned}\epsilon - 3p &= \frac{T^2}{V}\left.\frac{\partial \ln Z}{\partial T}\right|_V - 3T \left.\frac{\partial \ln Z}{\partial V}\right|_T \\ &= -\frac{T^2}{V}\frac{1}{T} a_\tau \left.\frac{\partial}{\partial a_\tau}(\ln Z)\right|_{a_\sigma} - 3\, T \frac{1}{3V}\, a_\sigma \left.\frac{\partial}{\partial a_\sigma}(\ln Z)\right|_{a_\tau} \\ &= -\frac{T}{V}\left(\left.\frac{\partial \ln Z}{\partial \ln a_\tau}\right|_{a_\sigma} + \left.\frac{\partial \ln Z}{\partial \ln a_\sigma}\right|_{a_\tau}\right)\end{aligned} \tag{6.17}$$

and we arrive at Eq. (6.14) for the case of $a_\sigma = a_\tau = a$ i. e. for the isotropic case.

Then, by making use of the explicit form of our lattice action (Eq. (2.6) and Eq. (2.15)) we perform the derivative with respect to a by taking the derivatives with respect to the bare parameters κ, $a\mu$ and β. Taking into account that both κ_c and $a\mu$ are themselves functions of the coupling we arrive at:

$$\begin{aligned}\frac{I}{T^4} = \frac{\epsilon - 3p}{T^4} &= -\frac{T}{VT^4}\frac{d \ln Z}{d \ln a} \\ &= N_\tau^4 \left(a\frac{d\beta}{da}\right) \frac{1}{N_\sigma^3 N_\tau}\left\{\frac{c_0}{3}\left\langle \mathrm{ReTr}\sum_P U_P\right\rangle_{\mathrm{sub}} + \frac{c_1}{3}\left\langle \mathrm{ReTr}\sum_R U_R\right\rangle_{\mathrm{sub}}\right. \\ &\qquad + \left(\frac{\partial \kappa_c}{\partial \beta}\right)\langle \bar\chi D_{\mathrm{W}}[U]\chi\rangle_{\mathrm{sub}} \\ &\qquad \left. - \left[2(a\mu)\left(\frac{\partial \kappa_c}{\partial \beta}\right) + 2\kappa_c\left(\frac{\partial (a\mu)}{\partial \beta}\right)\right]\left\langle \bar\chi i\gamma_5 \tau^3 \chi\right\rangle_{\mathrm{sub}}\right\} .\end{aligned} \tag{6.18}$$

Upon defining the β-functions as the derivatives of the bare parameters with respect to

the lattice spacing

$$B_\beta = a\frac{d\beta}{da}\,, \qquad B_\mu = \frac{1}{(a\mu)}\frac{\partial(a\mu)}{\partial\beta}\,, \qquad B_\kappa = \frac{\partial\kappa_c}{\partial\beta}\,, \tag{6.19}$$

we end up with the following expression for the trace anomaly:

$$\begin{aligned}\frac{I}{T^4} = N_\tau^4 B_\beta \frac{1}{N_\sigma^3 N_\tau}\Bigg\{ &\frac{c_0}{3}\left\langle \mathrm{ReTr}\sum_P U_P\right\rangle_{\mathrm{sub}} + \frac{c_1}{3}\left\langle \mathrm{ReTr}\sum_R U_R\right\rangle_{\mathrm{sub}} \\ &+ B_\kappa \left\langle \bar\chi D_{\mathrm{W}}[U]\chi\right\rangle_{\mathrm{sub}} \\ &- [2(a\mu)B_\kappa + 2\kappa_c(a\mu)B_\mu]\left\langle \bar\chi i\gamma_5\tau^3\chi\right\rangle_{\mathrm{sub}}\Bigg\}\,.\end{aligned} \tag{6.20}$$

The evaluation of the β-functions will be discussed further in section 6.3.

The expectation values one needs to calculate in Eq. (6.20) have to be normalised to their corresponding $T = 0$ values in order to render them finite in the ultraviolet [CEH$^+$10] by means of the following subtraction:

$$\langle\ldots\rangle_{\mathrm{sub}} \equiv \langle\ldots\rangle_{T>0} - \langle\ldots\rangle_{T=0}\ . \tag{6.21}$$

As we are partly relying on the available ETMC data for taking these subtractions it is necessary to perform interpolations of the $T = 0$ data in the bare coupling and mass to be discussed in section 6.5. The evaluation of the fermionic terms will be further illustrated in appendix A.

From Eq. (6.8) it is straightforward to calculate the following relation between the trace anomaly I and the pressure p

$$\frac{I}{T^4} = T\frac{\partial}{\partial T}\left(\frac{p}{T^4}\right)\,. \tag{6.22}$$

Then by Eq. (6.22) the pressure can be evaluated by means of $\epsilon - 3p$ via integration:

$$\frac{p}{T^4} - \frac{p_0}{T_0^4} = \int_{T_0}^{T} d\tau \frac{\epsilon - 3p}{\tau^5}\bigg|_{\mathrm{LCP}}\,, \tag{6.23}$$

which has to be performed along a line of constant physics (LCP), see discussion in paragraph 6.6 below. Furthermore, the lower bound of the integration should be set at a low enough temperature value T_0 in such a way that p_0 is close to zero and can be neglected.

The integration of Eq. (6.23) is performed by fitting the ansatz

$$\frac{I}{T^4} = \exp\left(-h_1\bar t - h_2\bar t^2\right)\cdot\left(h_0 + \frac{f_0\left\{\tanh\left(f_1\bar t + f_2\right)\right\}}{1 + g_1\bar t + g_2\bar t^2}\right) \tag{6.24}$$

to the available lattice data of $\frac{I}{T^4}$ and integrating numerically in temperature. Above

ansatz, that has been used in Ref. [BEF+10], incorporates the sharp rise of the trace anomaly around T_c via the tanh function as well as its decrease at larger T. But instead of fixing the normalisation temperature T_0 in the dimensionless ratio $\bar{t} \equiv T/T_0$ as was done in Ref. [BEF+10] we include T_0 as a fit parameter.

6.3 Evaluation of β-Functions

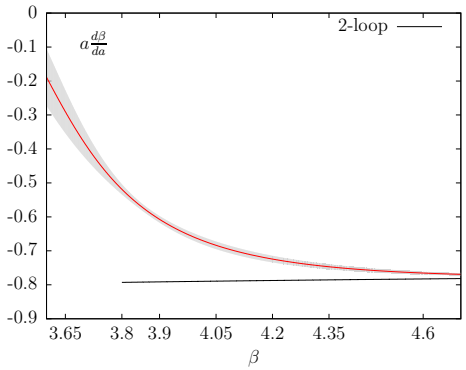

Figure 6.1: The β-function obtained according to Eq. (6.25) from fitting expression (6.26) to the chirally extrapolated data of the Sommer scale $\left(\frac{r_\chi}{a}\right)$. We also show the perturbative 2-loop expectation at large couplings according to Eq. (6.28).

The evaluation of Eq. (6.20) requires the knowledge of the β-functions B_β, B_μ and B_κ. Following Ref. [CCD+08] we try to evaluate these functions using non-perturbative input from our $T = 0$ lattice data. In order to reproduce the correct perturbative behaviour of the β-functions we incorporate it explicitly into fit functions that we fit to $T = 0$ data.

The most prominent β-function B_β, entering Eq. (6.20) as a multiplicative factor, we will evaluate by means of the following identity which expresses it in terms of the chirally extrapolated Sommer parameter $\left(\frac{r_\chi}{a}\right)$:

$$B_\beta = \left(a\frac{d\beta}{da}\right) = -\left(\frac{r_\chi}{a}\right)\left(\frac{d\left(\frac{r_\chi}{a}\right)}{d\beta}\right)^{-1} . \tag{6.25}$$

One could also choose to use other dimensionful physical quantities to reexpress B_β as has been done above. $\left(\frac{r_\chi}{a}\right)$ though seemed to us the most convenient, as it is easily calculated. In order to be consistent, also the temperature is defined from this quantity throughout this chapter, corresponding to method 2 for scale setting (see section 4.1).

In order to recover the perturbative behaviour of B_β at large couplings we employ the following ansatz for fitting $\left(\frac{r_\chi}{a}\right)$:

$$\left(\frac{r_\chi}{a}\right)(\beta) = \frac{1 + n_0 R(\beta)^2}{d_0\left(a_{2\mathrm{L}}(\beta) + d_1 R(\beta)^2\right)} , \tag{6.26}$$

where the ratio $R(\beta)$ is defined as follows in terms of the two-loop perturbative formula for $a_{2\mathrm{L}}(\beta)$ Eq. (2.21):

$$R(\beta) = \frac{a_{2\mathrm{L}}(\beta)}{a_{2\mathrm{L}}(3.9)} \,. \tag{6.27}$$

The functional form is inspired by an ansatz employed in Ref. [CCD+08] but with reduced number of fit parameters, as we have fewer data points to fit. At present, we have nine data points for $\left(\frac{r_\chi}{a}\right)$ at our disposal and we manage to obtain a good fit with $\chi^2/\mathrm{dof} = 0.74$. The point at $\beta = 4.6$ that has not yet been chirally extrapolated has been neglected in the fit. Using Eq. (6.25) and the two-loop expression Eq. (2.21) we obtain the following asymptotic formula valid at large couplings β:

$$B_\beta(\beta) = -12\beta_0 - 72\frac{\beta_1}{\beta} \,. \tag{6.28}$$

The interpolation of B_β we calculate from the fit is shown in Fig. 6.1 together with the 2-loop perturbative expectation according to Eq. (6.28). The grey band in the graph shows the error from the fit which is obtained by means of a bootstrap analysis. The level of the error is of the order of 20 % for low values of the coupling and goes down to the 1 % level for higher values.

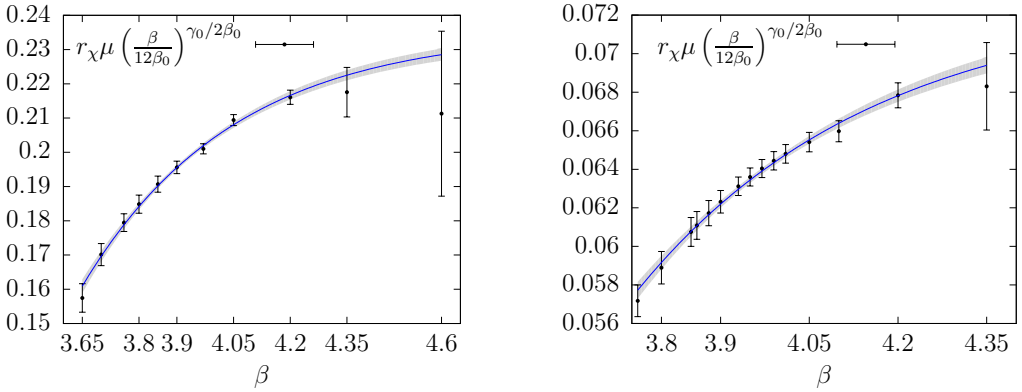

Figure 6.2: Left: Fit of $r_\chi\mu$ to the formula Eq. (6.30) for the D mass. **Right**: The same quantity for the B mass.

For the evaluation of the second β-function B_μ we observe that:

$$\begin{aligned} B_\mu &= \frac{1}{(a\mu)}\frac{\partial(a\mu)}{\partial\beta} \\ &= \frac{1}{(a\mu)}\left(\mu\frac{\partial a}{\partial\beta} + a\frac{\partial\mu}{\partial\beta}\right) \\ &= \frac{1}{(a\mu)}\left((a\mu)\frac{1}{a}\frac{\partial a}{\partial\beta} + \frac{1}{\left(\frac{r_\chi}{a}\right)}\frac{\partial(r_\chi\mu)}{\partial\beta}\right) \\ &= B_\beta^{-1} + \frac{1}{r_\chi\mu}\frac{\partial(r_\chi\mu)}{\partial\beta} \,, \end{aligned} \tag{6.29}$$

where we have used the fact that $\frac{\partial r_\chi}{\partial \beta} = 0$, r_χ being the physical quantity that fixes the scale. We then fit $(r_\chi \mu)(\beta)$ by the following expression

$$r_\chi \mu = \left(\frac{12\beta_0}{\beta}\right)^{\gamma_0/2\beta_0} P(\beta) \; . \tag{6.30}$$

The first factor gives the leading perturbative β-dependence of the mass (compare e. g. Ref. [CR00]) with $\gamma_0 = 1/(2\pi^2)$. The second term is a polynomial in terms of the ratio $R(\beta)$ defined above for which we take

$$P(\beta) = a_\mu \left(1 + b_\mu R(\beta)^2\right) \; . \tag{6.31}$$

As Fig. 6.2 is conveying we obtain reasonable fit results using this ansatz and we show the result for the combination of β-functions $B_\beta B_\mu$ in Fig. 6.3.

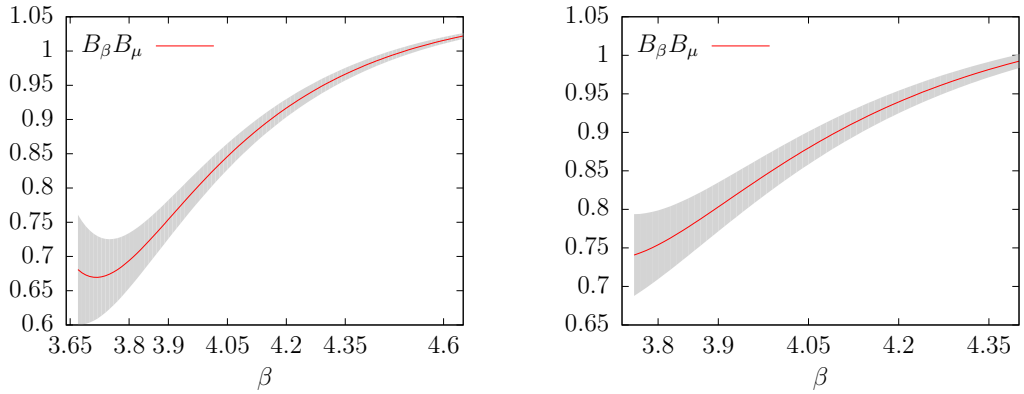

Figure 6.3: Left: Combination of β-functions $B_\beta B\mu$ for the D mass. **Right**: The same quantity for the B mass.

The third and remaining β-function B_κ is calculated in the most straight-forward manner from an explicit derivative of κ_c with respect to β using the fitted Padé interpolation that was presented in Fig. 2.2.

6.4 The Stefan-Boltzmann Limit

For a non-interacting field theory the pressure can be evaluated analytically in the massless limit. For the derivation of the so-called Stefan-Boltzmann limit we follow the discussion of [Rot05].

Starting from Eq. (6.8) for the pressure of a single real bosonic quantum field ϕ with

$$\begin{aligned} Z_0 &= \mathcal{N} \int D\phi \; \mathrm{e}^{-\int_0^{1/T} d\tau \int d^3\sigma \mathcal{L}_E[\phi, \partial_\mu \phi]} \\ &= \widehat{\mathcal{N}} \int D\hat{\phi} \; \mathrm{e}^{-1/2 \int_0^1 d\hat{\tau} \int d^3\hat{\sigma} \; \hat{\phi}(-\hat{\partial}_\mu \hat{\partial}_\mu + \hat{M}^2)\hat{\phi}} \; , \end{aligned} \tag{6.32}$$

where the Euclidean Lagrangian density $\mathcal{L}_E[\phi, \partial_\mu\phi]$ for a real scalar field

$$\mathcal{L}_E[\phi, \partial_\mu\phi] = \frac{1}{2}\left(\partial_\mu\phi\partial_\mu\phi + M^2\right) \tag{6.33}$$

has been used and where in the second line of Eq. (6.32) we have expressed all ingredients in terms of dimensionless variables by multiplying with according powers of the temperature:

$$\begin{aligned} \hat{\phi} &= \frac{\phi}{T}, \qquad & \hat{M} &= \frac{M}{T}, \\ \hat{\tau} &= T\tau, \qquad & \hat{\sigma}_i &= T\sigma_i \ . \end{aligned} \tag{6.34}$$

The divergent multiplicative constant $\mathcal{N}$ ($\widehat{\mathcal{N}}$), which corresponds to an irrelevant shift in the pressure, will be dropped further on. After performing the usual Gaussian integral one is left with the evaluation of the determinant of the operator

$$\ln Z_0 = \ln\left(\det(-\hat{\partial}_\mu\hat{\partial}_\mu + \hat{M}^2)\right)^{-1/2} \ . \tag{6.35}$$

The functions

$$\tilde{\phi}(\hat{\vec{\sigma}}, \hat{\tau}) = \frac{1}{\sqrt{\hat{V}}}\mathrm{e}^{2\pi\mathrm{i}\left(n\hat{\tau} + \vec{m}\cdot\hat{\vec{\sigma}}/\hat{L}\right)} \tag{6.36}$$

are eigenfunctions of the operator $\frac{1}{2}\left(\hat{\partial}_\mu\hat{\partial}_\mu + \hat{M}^2\right)$ with eigenvalues

$$\lambda_{n,\vec{m}} = (2\pi)^2\left(n^2 + \frac{\vec{m}^2}{\hat{L}^2} + \hat{M}^2\right) \ . \tag{6.37}$$

Making use of the fact that the determinant of an operator is given as the product of all eigenvalues and dropping constant shifts in $\ln Z_0$, Eq. (6.35) yields:

$$\ln Z_0 = -\frac{1}{2}\sum_{\vec{p}}\sum_n \ln\left(n^2 + \left[\frac{E(\vec{p})}{2\pi T}\right]^2\right) \ , \tag{6.38}$$

where $E(\vec{p}) = \sqrt{\vec{p}^2 + M^2}$ and $\vec{p} = \frac{2\pi}{L}\vec{m}$ have been substituted. Upon replacing the finite sum over momenta $\vec{p}$ by an integral via

$$\sum_{\vec{p}} \to V\int \frac{d^3p}{(2\pi)^3} \ , \tag{6.39}$$

performing the sum over n explicitly[1] and discarding again irrelevant constant shifts of

[1] The divergent sum $\sum_{-\infty}^{\infty}\ln\left(n^2 + x^2\right)$ can be done by noting that it is equivalent to the expression $\ln(x^2) + 2g(x)$ where $\frac{dg}{dx} = \sum_1^\infty \frac{2x}{n^2+x^2}$. The latter is explicitly summable and can in turn be integrated to yield an expression for $g(x)$. See [Rot05] for further details.

$\ln Z_0$ one is left with the integral

$$\ln Z_0 = -V \int \frac{d^3p}{(2\pi)^3} \ln\left(1 - \mathrm{e}^{-E(\vec{p})/T}\right) \ . \tag{6.40}$$

After partial integration and switching to spherical coordinates, the integral becomes a tabulated standard integral upon taking the limit $M \to 0$:

$$\Omega_0 = -T \ln Z_0 = -TV \frac{\zeta(4)}{\pi^2} T^3 \ , \tag{6.41}$$

where $\zeta(4) = \pi^4/90$ is the Riemann zeta function. Using Eq. (6.7) we get for the bosonic pressure of one degree of freedom:

$$p_B = \frac{\pi^2}{90} T^4 \ . \tag{6.42}$$

For fermions one finds the according ideal gas formula as in Eq. (6.40) but with an overall minus sign and with the sign in the logarithm inverted. These differences in signs lead to an overall factor of $\frac{7}{8}$ and the fermionic free gas pressure reads:

$$p_F = \frac{7}{8} \frac{\pi^2}{90} T^4 \ . \tag{6.43}$$

We are left to count the number of bosonic and fermionic degrees of freedom n_B and n_F for $N_f = 2$ QCD:

$$\begin{aligned} n_B &= 2 \times (N^2 - 1) = 16 \\ n_F &= N_f \times N \times 2_{\text{spin}} \times 2_{\text{anti}} = 24 \ . \end{aligned} \tag{6.44}$$

These reflect the eight gluons that (as being massless particles) can incorporate two helicity states as well as N_f coloured quarks of spin two that have an according anti-particle ($\times 2_{\text{anti}}$). Finally we arrive at the Stefan-Boltzmann pressure relevant for this work:

$$\frac{p_{\text{SB}}}{T^4} = \left(16 + \frac{7}{8} \times 24\right) \frac{\pi^2}{90} \approx 4.0575 \ . \tag{6.45}$$

Using free lattice propagators it is also possible to calculate the free Stefan-Boltzmann pressure p^L_{SB} on the lattice. Compared to p_{SB} the latter receives N_τ-dependent corrections vanishing in the continuum limit for $N_\tau \to \infty$. For the twisted-mass action p^L_{SB} has been calculated in Refs. [PZ10, Zei08]. Through the mass dependence of the fermion propagator, p^L_{SB} as well as p_{SB} depend in general on the ratio of renormalised quark mass and temperature $\frac{m_R}{T}$.

Because this dependence is weak (the change being of the order of below 1 % when varying $\frac{m_R}{T}$ from 0.2 to 0.02, see page 45 of Ref. [Zei08]), one can use the ratio $p^L_{\text{SB}}/p_{\text{SB}}$ for the correction of the trace anomaly as both p and I are related via Eq. (6.22). As the dependence on T proceeds via the dependence on the dimensionless ratio $\frac{m_R}{T}$ (which is

found to be small), a correction of the pressure dividing p by $p^L_{\mathrm{SB}}/p_{\mathrm{SB}}$ on the right hand side of Eq. (6.22) leads to the same correction of the trace anomaly on the left hand side, as the division factor can be taken out of the temperature derivative being approximately T-independent. This procedure is known in literature as tree-level improvement on the observable level and has been applied to thermodynamic quantities in Ref. [BEF$^+$10]. Its effectiveness is also demonstrated in Ref. [BEF$^+$11].

The ratio of lattice and continuum pressure for the twisted mass fermion action are taken from page 45 of Ref. [Zei08] for a value of $\frac{m_R}{T} = 0.2$ (the value for $N_\tau = 12$ has been taken from figure 4 of Ref. [PZ10] for the case of $\frac{m_R}{T} = 0.03$). Together with the corresponding ratio for the tree-level Symanzik improved gauge action to be found in Ref. [KLP00] we obtain the following correction factors that are used throughout this work:

N_τ	4	6	8	10	12
$p^L_{\mathrm{SB}}/p_{\mathrm{SB}}$	2.586	1.634	1.265	1.134	1.084

.

The tree-level correction then amounts to making the following replacement for the trace anomaly in the whole temperature interval:

$$\left(\frac{I}{T^4}\right) \Rightarrow \left(\frac{I}{T^4}\right) \Big/ \left(\frac{p^L_{\mathrm{SB}}}{p_{\mathrm{SB}}}\right) . \tag{6.46}$$

6.5 Interpolation of $T = 0$ Observables

We have calculated the quantities needed in Eq. (6.20) for all pairs of values of β and $(a\mu)$ that are available from ETMC [B$^+$10a]. Additionally we have substantially increased the $T = 0$ data by additional $T = 0$ runs.

Nevertheless, we have to interpolate (mildly extrapolate in some cases) these quantities to the precise value of the twisted mass parameter $(a\mu(\beta))$ that are used for the finite temperature runs. This is done by fitting a cubic spline function in $a\mu$ to our $T = 0$ data points and use the outcoming fit curve as interpolation curve. This kind of interpolation in $(a\mu)$ is only necessary to do for some values of β where the bare masses are not matched with the simulations done at $T > 0$ (in most cases at values of the couplings that have been studied by ETMC). Additionally to this we have to do an interpolation of these (possibly $(a\mu)$-interpolated) values in the coupling β in order to match to the values of the coupling we have used at finite temperature. We are using polynomial fits of degree four (five) for the gauge (fermionic) expectation values of Eq. (6.20) as we are not aware of any physically motivated fit function for the bare contributions to the trace anomaly in the bare coupling.

As long as we have not supplemented every $T > 0$ simulation by an according $T = 0$ simulation we have to rely on such interpolations, two of which are shown in the left and right panels of Fig. 6.4 for the plaquette and the chiral condensate. As from these figures it is impossible to estimate (by eye) the quality of the fit due to the tiny error bars of $\langle U_P \rangle$ and $\langle \bar{\psi}\psi \rangle$, we show the residuals of the fits (i. e. the difference of the data and the fit normalised by the corresponding errors) in the lower panels of the figures. For the D

Ensemble		ReTr $\langle U_P \rangle$	ReTr $\langle U_R \rangle$	$\langle \bar{\psi}\psi \rangle$	$\langle \bar{\chi} D_{\mathrm{W}}[U] \chi \rangle$
D	χ^2/dof	2.6	3.7	1.2	1.8
B	χ^2/dof	1.4	1.3	1.3	2.3

Table 6.1: Fit results for $T = 0$ interpolations providing the subtraction for the trace anomaly. In all cases we have used a polynomial ansatz of degree 5.

mass ensemble we restrict the fits to the β-interval $3.70 \leq \beta \leq 4.2$, i. e. we do not include $\beta = 3.65$ nor $\beta = 4.35$ and 4.6 in the fits. If one includes these points large negative values for the trace anomaly are obtained for both low and high temperatures and one ends up with a bad description of the data by the fit function resulting in large values of χ^2/dof. This of course seems plausible as one can not expect that a non-physical polynomial ansatz is capable of describing bare data over such a large interval in the coupling. We can however include these finite temperature points by directly subtracting the $T = 0$ result at these couplings.

For the B mass we have included all available $T = 0$ data points apart from $\beta = 3.8$. The reason for discarding this point is that it is responsible for a sizeable increase of the χ^2/dof. Table 6.1 summarises the interpolating fits for the different contributions to the trace anomaly.

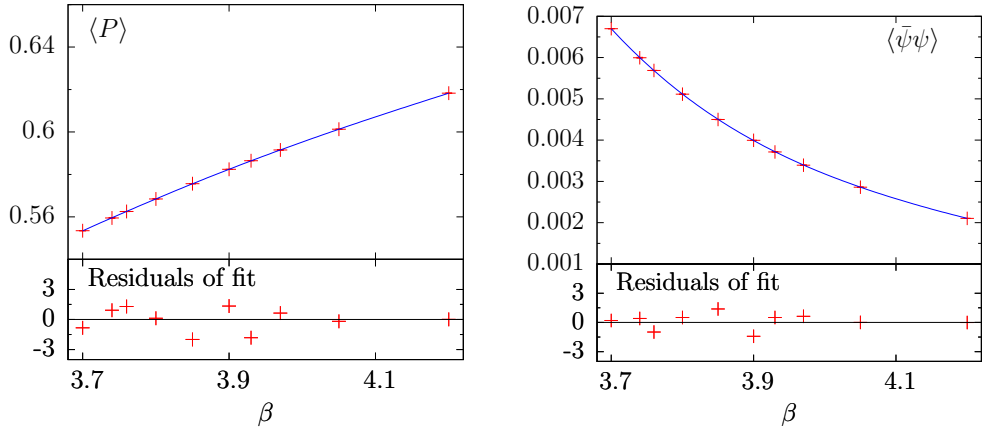

Figure 6.4: **Left**: Interpolation of ($T = 0$) values in the coupling β for the plaquette $\langle P \rangle = \mathrm{ReTr}\,\langle U_P \rangle / (18 N_\tau N_\sigma^3)$ using a polynomial fit. **Right**: The same for the chiral condensate $\langle \bar{\psi}\psi \rangle$. In both cases we show the residuals of the fits in the lower panels in order to show the quality of the interpolation.

6.6 Lines of Constant Physics

Because the physical quark mass is not changing when crossing the finite temperature transition from the hadronic into the QGP phase, the calculation of the pressure by

means of integrating Eq. (6.23) has to be done on a line of constant physics (LCP).

Several prescriptions can be found in literature on how to fix the LCP. While in the $N_f = 2+1$ simulations with staggered fermions of Ref. [BEF$^+$10] and Ref. [CEH$^+$10] the masses of the strange and light quarks have been kept fixed to their physical (or almost physical) values during the integration of the pressure, the authors of Ref. [AK$^+$01a] chose to keep the mass ratio of the pseudoscalar and vector meson $m_{\mathrm{PS}}/m_{\mathrm{V}}$ constant.

For the determination of the critical temperatures we have approximately fixed the pion mass in a small range of temperature (i. e. the bare coupling) around the critical region by tuning the bare quark mass by means of the β-function (see paragraph 2.6). We have sticked to this prescription when enlarging the temperature interval covered by our simulations both towards larger and lower temperatures. For the ensembles at $N_\tau = 12$ this procedure resulted in a constant physical pion mass within errors. In Fig. 6.6 we show the situation for the B mass for which we have simulated more $T = 0$ points. As one observes from the figure the newly simulated points fall on a line with the ETMC data and we fit all points to a constant which yields $m_\pi = 410(8)$ MeV.

For our largest mass (the D ensemble) we though observe a rise of m_{PS} over the available range of couplings (left panel of Fig. 6.5). Especially in the low coupling region the mass is increasing while it seems to saturate to some extent and becomes constant within errors for $3.8 \leq \beta \leq 4.2$ as we do observe for the A, B and C mass. For $\beta > 4.2$ it starts rising again. This is caused by the fact that we were relying on the β-function to set the bare mass also in this high mass region, where no input (i. e. simulation data) has been available from ETMC. The same is true for $\beta < 3.8$, where it has become necessary to simulate in order to cover the whole range of the transition for $N_\tau = 8$. We note however that the violations of the LCP we are facing are at the level of 10 % as can be seen from the two dashed lines in the left panel of Fig. 6.5 which denote the 10 % deviations from the fitted mean value (solid line). The magnitude of the mismatched LCP can be compared with the reported 3 % violation of the LCP in Ref. [CEH$^+$10]. Moreover, we notice that at least with the present set of $T = 0$ simulations we managed to keep fixed the ratio of meson masses of the pseudoscalar and the vector meson $m_{\mathrm{PS}}/m_{\mathrm{V}}$. This is caused by the fact that m_{V} is a rising function of m_{PS}. Fig. 6.5 shows this mass ratio together with a constant fit that yields $m_{\mathrm{PS}}/m_{\mathrm{V}} = 0.562(6)$. We also show the 1-$\sigma$ confidence interval of this fit in the figure.

6.7 Results for the Equation of State

In this section we present our results for the trace anomaly and the thereof derived thermodynamic quantities for the B and D ensembles. The results have been obtained using the methods introduced in the previous paragraphs.

Table 6.2 lists the best fit parameters together with errors of fits of the interpolation formula Eq. (6.24) to the trace anomaly data for the D and B ensembles after the trace anomaly has been corrected using the tree-level correction Eq. (6.46). The table also provides the resulting values of χ^2/dof of these fits. The interpolations are illustrated together with the corresponding data in the right panels of Fig. 6.7 and Fig. 6.8 for the

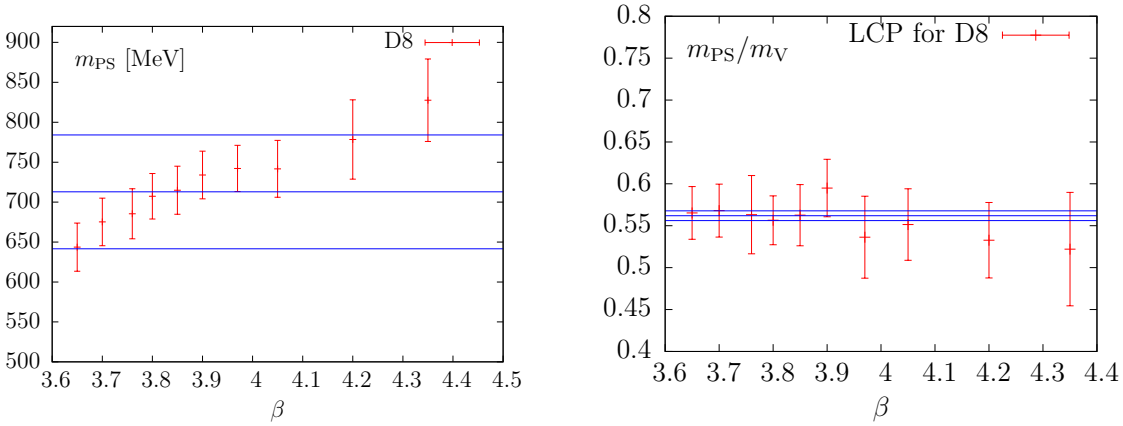

Figure 6.5: Left: Pseudoscalar mass in physical units for the D ensembles together with a constant fit over all data points. The dashed lines indicate the 10 % deviations of the fitted central value in both directions. **Right**: Mass ratio of pseudoscalar and vector mesons for the D ensembles together with a constant fit and the according fit error (dashed lines).

D and B mass, respectively.

The error of the interpolation indicated by a grey band in these figures is evaluated as follows. From fits to bootstrap samples of our data we estimate a first error of our interpolation, giving rise to the errors on the fit parameters presented in Table 6.2. A second error is obtained by fitting the interpolation function to the data shifted by one standard deviation in the upper and lower directions and measuring the deviation to the fit of the original data. Both errors are then added in quadrature. We have adopted this rather non-standard method because we have observed that the first of these errors (originating from the bootstrap analysis) is very small as compared to the uncertainties of the data themselves. This is especially true for the low temperature region. Thus by considering the pure fit error we would certainly have underestimate the error of the trace anomaly interpolation there.

For the D ensemble we have included $N_\tau = 10$ and $N_\tau = 8$ into the fit, while for the B ensemble we fit $N_\tau = 12, 10$ and 8. For the B ensemble this mixing of data including potentially different lattice cutoff effects is necessary in order to cover a wide enough range in T. If we had restricted ourselves to the data of our finest lattices at $N_\tau = 12$ we could have evaluated thermodynamic quantities only up to $T \approx 400$ MeV. Moreover, doing so, we would not have been able to use the other values of N_τ at all, as we are not covering the rising part of I/T^4 with these lattices yet. The validity of this approach and the use of the tree-level correction after all will be justified in what follows.

The tree-level correction of the trace anomaly may be substantiated by studying the continuum limit of I/T^4 with and without the correction in place. To this purpose we show in Fig. 6.9 a comparison of two different ways to take the continuum limit of the trace anomaly for the D ensemble. We study three values of the temperature $T = (282,$

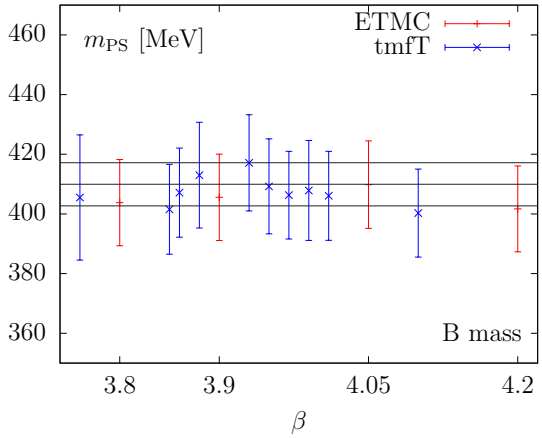

Figure 6.6: Pion mass in physical units for the B ensemble together with a constant fit over all data points. We also show the according error band by dashed lines.

Ensemble	Parameters				
	h_0	h_1	h_2	f_0	f_1
D	0.01(5)	-7(2)	7(1)	0.08(7)	1.026(6)
	f_2	g_1	g_2	T_0	χ^2/dof
	4.798(3)	-2.04(8)	1.08(8)	272(6)	1.7
Ensemble	Parameters				
	h_0	h_1	h_2	f_0	f_1
B	0.0(5)	-8(2)	9(2)	0.1(6)	-1.29865(2)
	f_2	g_1	g_2	T_0	χ^2/dof
	12.41691(1)	-1.98(8)	1.00(8)	255(8)	1.8

Table 6.2: Fit parameters obtained from fits of Eq. (6.24) to the tree-level corrected trace anomaly data of the D and B mass ensembles.

318 and 392) MeV in the range of the maximum of the interaction measure. Data for $N_\tau = 6$ and $N_\tau = 8$ is linearly interpolated in between the two points adjacent to the given temperature under investigation. We perform continuum extrapolations linear in $1/N_\tau^2$ once with the multiplicative correction (Eq. (6.46)) in place and once without this correction. We observe that both procedures lead to compatible continuum limit values matching each other within two standard deviations for the trace anomaly. A similar study has been done for the B mass ensemble concentrating again on three values of the temperature, namely $T = (250,\ 326,\ \text{and}\ 391)$ MeV. While for the two lower values of T we have considered $N_\tau = 8, 10$ and 12 for the continuum limit, we were even able to include a data point at $N_\tau = 6$ for $T = 391$ MeV. Looking at the result presented in Fig. 6.10 we conclude again that the same continuum value is reached from both the corrected as well as the uncorrected data. In general the correction leads to a flatter continuum limit than we observe for the uncorrected data especially at large tempera-

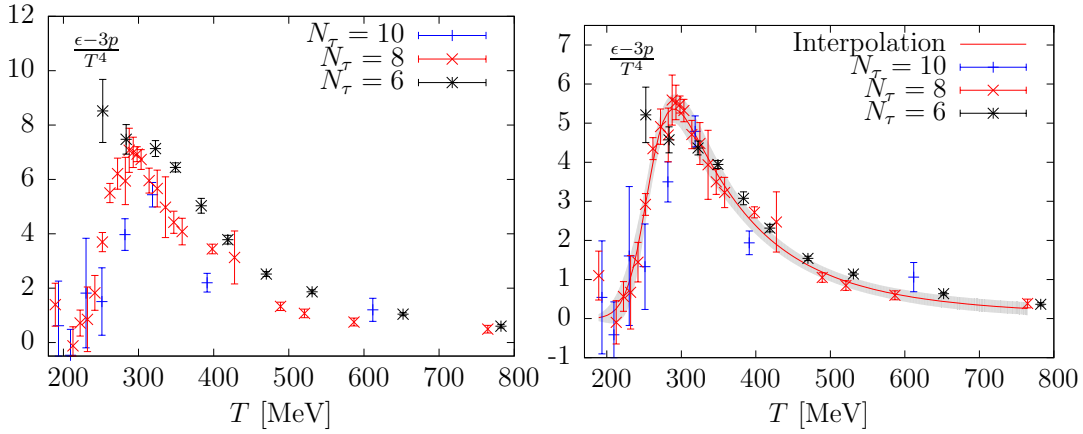

Figure 6.7: Left: The trace anomaly for the D mass obtained for different values of the temporal extent N_τ. **Right**: The same quantity but divided by the tree-level correction factor for the pressure $\frac{p^L_{\mathrm{SB}}}{p_{\mathrm{SB}}}$ defined in Eq. (6.46) to reduce lattice artefacts. Also shown is the result of a combined fit of the interpolation formula Eq. (6.24) to the $N_\tau = 8$ and 10 data.

tures. There the corrected results are even compatible with a constant continuum limit. Moreover, the corrected trace anomaly at the two largest temporal extents for the D mass ($N_\tau = 8, 10$ and 12 for the B mass) are in most cases compatible within errors. This fact thus justifies a posteriori our choice to include lattices from different N_τ into the same interpolation fit of the trace anomaly. The effectiveness of tree-level improvement may be even appreciated directly from the corrected trace anomaly depicted in the right panel of Fig. 6.7 for the D ensemble as well as in the right panel of Fig. 6.8 for the B ensemble, where we present our final results for the interaction measure. The correction effectively superimposes the curves of $I(T)$ for different values of N_τ. For a definite statement if the correction leads to the same continuum limit for the D mass at the three considered temperatures as well as over the whole temperature interval it is necessary to increase the precision on the $N_\tau = 10$ data as well as to add points with $N_\tau = 12$. The latter seems mandatory as the transition might be shifted towards lower temperatures for our coarsest discretisation as argued in sections 3.5 and 4.2. As for the B mass, more data at $N_\tau = 10$ is needed for the low temperature region in order to check the continuum limit behaviour there.

For the D6 ensemble we have additionally checked if finite size effects are present in the data at $T > 0$ for two points in temperature. We have done so by increasing the spatial extent of the lattices from $N_\sigma^3 = 16^3$ to $N_\sigma^3 = 32^3$ i. e. by doubling the lattice size in each spatial direction. The following small table shows the values for the trace anomaly before tree-level correction in comparison:

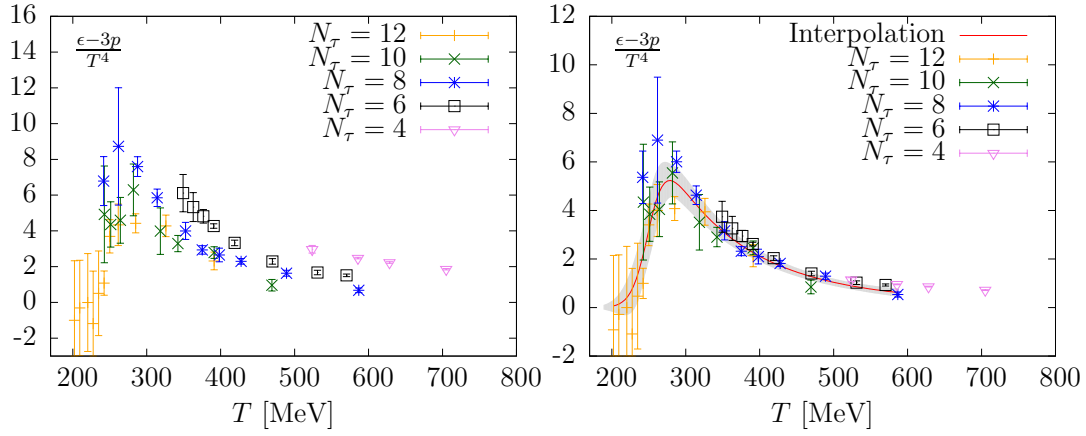

Figure 6.8: Same as in Fig. 6.7 but for the B mass. The curve in the right panel shows the result of a fit of the interpolation formula Eq. (6.24) to the $N_\tau = 8, 10$ and 12 data.

$\frac{\epsilon-3p}{T^4}$	$T = 470$ MeV ($\beta = 3.97$)	$T = 531$ MeV ($\beta = 4.05$)
$N_\sigma = 16$	2.5(1)	1.87(7)
$N_\sigma = 32$	2.61(8)	1.87(7)

.

While for the smaller temperature the larger lattice produces a little bit larger value still almost compatible within errors, we observe no difference in the result for the trace anomaly at the larger temperature. We thus conclude that finite size effects are under control at the larger couplings at least for the finite temperature simulations.

We now turn to the comparison of our results for the interaction measure with results obtained elsewhere. Starting with the D mass our results for the trace anomaly can be compared to results from the CP-PACS collaboration [AK$^+$01a]. The smallest ratio of pion to vector mass for which results are reported in this reference reads $m_{\rm PS}/m_{\rm V} = 0.65$. Thus, this corresponds to a slightly larger value than is found here but we will nevertheless compare to the data at this ratio of masses in what follows. Having in mind the discrepancy in the staggered $N_f = 2 + 1$ case alluded to in the introduction, the most interesting quantity to compare is the height of the peak in the interaction measure. Referring to figure 22 of Ref. [AK$^+$01a], the maxima in I/T^4 are lying at ~ 13 and ~ 8 for $N_\tau = 4$ and $N_\tau = 6$, respectively. These values refer to the uncorrected trace anomaly and compare to the value obtained here: $I/T^4 \sim 7$ for the maximum at $N_\tau = 8$. The maximum for $N_\tau = 10$ can not be resolved with the given resolution in temperature at the moment.

We might also compare the height of the trace anomaly maximum with results at $N_f = 2 + 1$. From the fixed scale approach with Wilson fermions ($m_\pi \sim 630$ MeV) the maximum is reported at a value of ~ 7.5 [U$^+$12], while for simulations at the physical point it is reported at ~ 4 (stout staggered quarks [BEF$^+$10]) and ~ 6.5 (HISQ staggered quarks [CEH$^+$10]). Our results for the maximum of I/T^4 (considering the interpolation curve fitted to the tree-level corrected data) of ~ 5.5 is thus lying in the same range.

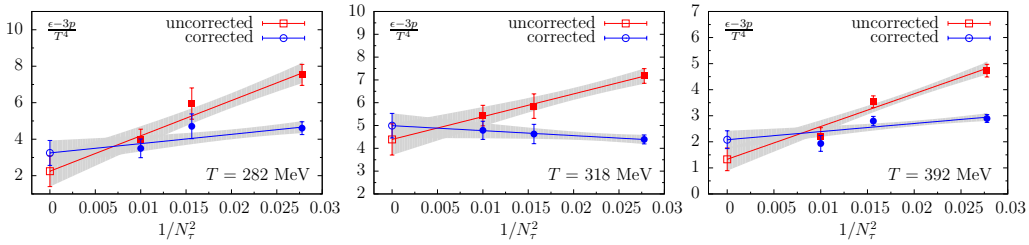

Figure 6.9: Continuum limit of the trace anomaly for three values of the temperature once with tree-level correction (blue points and lines) and once without (red points and lines). Data for the D mass ensemble at $N_\tau = 6, 8$ and 10 is shown.

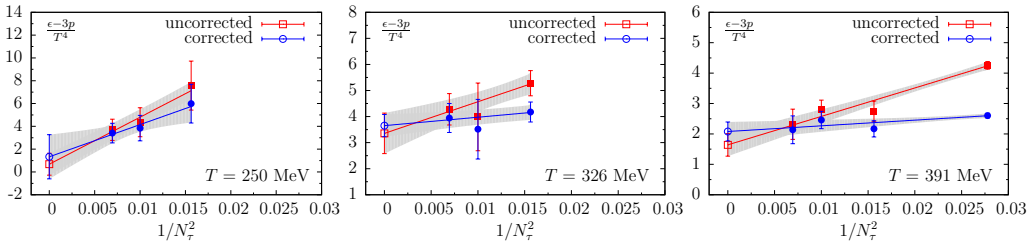

Figure 6.10: Same as Fig. 6.9 but for the B mass ensemble. The continuum limit is performed using data for $N_\tau = 8, 10$ and 12. For the highest temperature ($T = 391$ MeV) we have even included a data point at $N_\tau = 6$ into the extrapolation.

From the interpolation of the interaction measure described earlier in this paragraph it is straight forward to calculate the pressure by means of Eq. (6.23) by performing a numerical integration starting in all cases from the lowest available data point of I/T^4 where we set the pressure equal to zero. In other words we set $p_0 = 0$ in Eq. (6.23) with T_0 being our smallest temperature. Another possibility for the subtraction would be to consider model input for the pressure at temperatures far below the critical temperature region. For this purpose one could e. g. make advantage of a hadron resonance gas model that takes into account the distorted mass spectrum from lattice simulations using larger than physical pion mass as was done for instance in Ref. [HP10]. Correspondingly one would also have to consider in the model the missing of the *strange* quark in our current $N_f = 2$ approach. The integration is done making use of the function *integrate* that is provided by the R package. From the smooth interpolation we obtain the pressure (and the energy density from adding three times the pressure to I) for all temperatures in the temperature interval covered by our simulations. We do not restrict ourselves to the points in T where we actually have lattice data, but rather give the corresponding error channels for all upper integration bounds. This seems to us the most natural choice as we have included into the interpolation fits to I/T^4 data from several values of N_τ. In Fig. 6.11 we show our final results for the pressure ($3p$) as well as the energy density

(ϵ) as a function of the temperature. In these figures we also mark the temperature as a multiple of the critical temperature T_c at the top of the figures as obtained from the maximum of the chiral susceptibility (see section 4.2). The energy density features a sharp rise around T_c signalling the transition into the quark-gluon plasma regime. At temperatures of about $\sim 1.3\ T_c$ however, the increase has stopped and we observe an almost constant behaviour up to the largest temperatures considered. This feature is also observed by other groups c. f. Ref. [CEH$^+$10, BEF$^+$10, AK$^+$01a]. At large temperatures we can confront pressure and energy density to the ideal gas Stefan-Boltzmann pressure (Eq. (6.45)), which is indicated by the black arrow to the right of the figures. We see that at our largest temperatures around $\sim 3\ T_c$ ($\sim 2.7\ T_c$ for the B mass) the obtained pressure equals 0.68(9) (0.61(12)) of the Stefan-Boltzmann pressure. For the B mass this is a little bit lower (although of course compatible given the large error) than what is for instance reported by the Budapest-Wuppertal group. In Ref. [BEF$^+$10] they calculate a value of $\sim 0.69\ p_{\mathrm{SB}}$ at $T \sim 3\ T_c$ for their $N_f = 2+1$ simulations at the physical point. An explanation for this observation might be given by the fact that the zero point of the pressure is set at $T = 100$ MeV corresponding to roughly two third of the critical temperature in that reference. This temperature, which would equate to $T \sim 166$ MeV for the D ensemble ($T \sim 143$ MeV for the B ensemble) in our case, is thus lying 23 MeV (46 MeV) below our smallest available temperature. In order to clarify this point several smaller temperatures have to be simulated as well as the precision on the yet available small temperature data has to be increased.

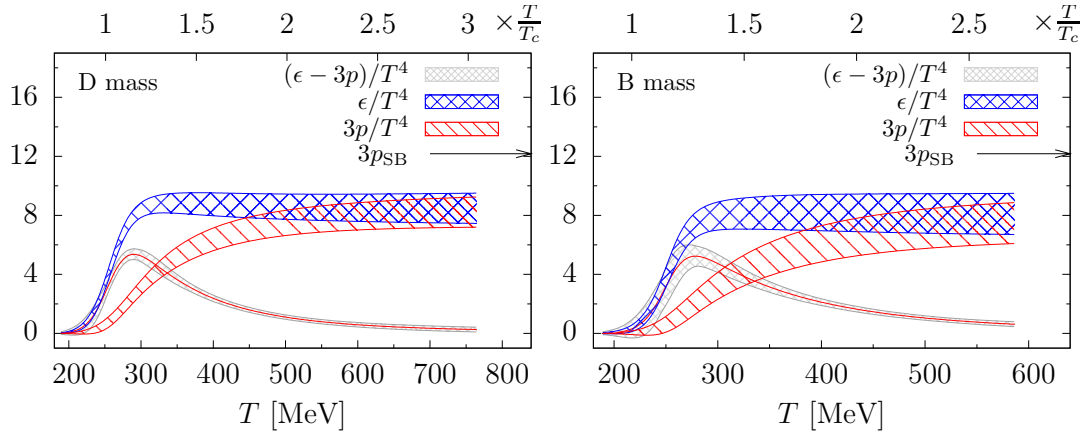

Figure 6.11: Left: Final result for pressure p and the energy density ϵ in units of T^4 for the D mass ensemble. We also show once more the interpolation of the trace anomaly used for integrating the pressure. **Right**: The same quantities for the B mass ensemble. The arrow to the right of the figures indicates the expected Stefan-Boltzmann limit for the pressure. On top of the figures we give the temperature in units of T_c.

In Fig. 6.12 we show our result for the ratio of pressure and energy density as well as the speed of sound c_s^2 as a function of the energy density in units of GeV/fm^3. The

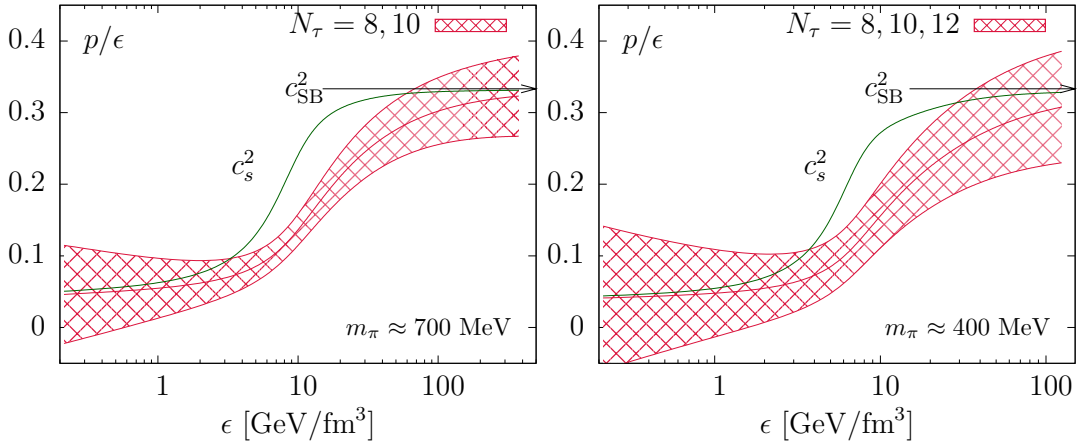

Figure 6.12: Left: The ratio $\frac{p}{\epsilon}$ for the D ensemble as a function of the energy density in units of GeV/fm^3. We also show the speed of sound squared c_s^2 obtained from $\frac{p}{\epsilon}$. **Right**: The same quantity for the B mass ensemble. Arrows indicate the expected large T Stefan-Boltzmann limit given by 1/3.

ratio p/ϵ is evaluated most directly from p and ϵ, whereas the speed of sound c_s^2 is evaluated according to Eq. (6.13) from its derivative. We do not calculate any error so far for the velocity of sound, as the error on the basic quantity p/ϵ itself is already very large. At large temperatures we observe that the limiting Stefan-Boltzmann value of $(p/\epsilon)_{\rm SB} = 1/3$ is nicely approached. However, we are not able at the current precision to resolve the dip at small temperatures that is observed in p/ϵ results from staggered simulations [BEF$^+$10, BBC$^+$09].

6.8 Discussion

We end this chapter with a short discussion about how the precision of the achieved results for the EoS compare to the precision of results obtained by typical staggered fermion simulations. Speaking generally, results for the EoS from latter fermion discretisations are much more advanced than the results presented in this work. Of course one of the advantages is the much smaller calculational costs of staggered in comparison to Wilson like fermion discretisations. Another reason for our results being less precise can certainly be sought in the shear numerical power in terms of computing time the large scale staggered simulation programs (as conducted by the hotQCD and Budapest-Wuppertal groups) are granted. However, there is yet a further possible explanation for the difference in precision which concerns fluctuations and autocorrelation times we find in both our $T = 0$ and finite temperature simulations in comparison to the staggered case.

As a small example of this statement we are in the following comparing one of our $T > 0$ data points (taking as an example the expectation value of the plaquette) with

another data point from a typical staggered calculation found in Ref. [BBC$^+$09]. The error on the plaquette value we obtain for $\beta = 3.8$ of our B mass point at $N_\tau = 8$ (with $N_\sigma = 28$) at ~ 5000 trajectories with $\tau_{\mathrm{MD}} = 1$ is of the order of $3 \cdot 10^{-5}$. Comparing this to the error of a point at $T = 206$ MeV found in table 10 of the appendix to Ref. [BBC$^+$09] from an asqtad staggered simulation we observe that the error that is quoted there is of the order of $5 \cdot 10^{-6}$ and thus much smaller than our uncertainty. Clearly the statistics reported for this point (~ 15000 trajectories with $\tau_{\mathrm{MD}} = 1$) is about a factor of three larger than ours and the staggered simulation is performed at spatial extent $N_\sigma = 32$ which also reduces somewhat the variance. Nevertheless, this cannot account for the factor of six in the error between these two points given the square root law of statistics. We furthermore emphasise that the two points we have chosen for this comparison are both lying in the region of temperature where the trace anomaly is maximal such that the difference is not related to temperature. Moreover, the staggered simulation is done at a significantly lower mass of the pseudoscalar particle and the intrinsic fluctuations of the gauge ensemble should therefore be larger (at least this is our empirical finding for our fermion discretisation). We are thus lead to the conclusion that our action has much more intrinsic noise which we would have to compensate for by increasing statistics. We dare to speculate that this fact might be attributed to the use of smearing in the staggered simulation, which reduces fluctuations.

7 Concluding Remarks & Perspectives

In this thesis we have presented a study of QCD thermodynamics within the Wilson twisted mass framework including two dynamical flavours of light mass-degenerate quarks. The mass dependence of the crossover transition has been investigated at several values of the pseudoscalar mass reaching down to a value of about 300 MeV which is at the edge of feasibility for a Wilson type of fermion discretisation given the present computational resources.

After having given a short introduction to the subject of finite temperature QCD on a lattice and having presented to the reader the twisted mass discretisation in chapter 2 we have introduced observables that are supposed to carry information about the finite temperature transition in chapter 3. Based on these observables we have been able to identify a region in temperature within which the transition occurs in chapter 4. We have found consistent signals in these observables throughout the range of the considered pseudoscalar mass. Being more precise, we have found observable dependent locations of the transition temperature from which we conclude that we are merely probing a crossover rather than a true phase transition in this region of intermediate quark masses. This observation is in accord with conclusions from investigations with other types of fermion discretisation. We thereby find that the chiral observables (i. e. the chiral susceptibility) features a smaller crossover temperature than the Polyakov loop connected to deconfinement. We moreover have observed a decrease of this difference in pseudo-critical temperatures towards higher mass which is understandable because a true phase transition is approached in this case.

In chapter 5 we have investigated the mass dependence of the crossover temperatures and couplings extracted from the signal of the chiral susceptibility. We have therewith tried to give an answer to the most interesting open physical question associated with the two flavour variant of QCD, namely the question of the order of the phase transition in the chiral limit. The basic idea that has been applied is that universal behaviour should be detectable in the vicinity of second order transitions. To this end we have compared our data for the mass dependence of T_c to different possible chiral scenarios in the chiral limit. We have been including an $O(4)$ second order transition scenario as well as a first order scenario and have studied the scaling in the mass imposing the respective critical exponents. From comparing the performance of the considered scenarios with one another we have made the observation that we are not yet able to discriminate in between different scenarios with the present set of pion masses. In order to do better, significantly lighter pion masses are required. From the present analysis we have been able however to quote the following value for the transition temperature in the chiral limit corresponding to the $O(4)$ scenario: $T_c(0) = 152(26)$ MeV. For this case we also

have conducted a comparison study of the order parameter employing the universal scaling function belonging to this universality class (the magnetic equation of state) for its description.

Our findings are that our data is compatible with the scaling function when data of a single individual mass is fit. For fitting several masses simultaneously however it was found necessary to add one or more scaling violating terms to the scaling function in order to obtain acceptable fits. Additionally, we have not included the high temperature data in the fits as doing so leads to unsatisfying fits. Thus, on the one hand, we are able to describe the lattice order parameter for three different masses with a deformed universal scaling function. But on the other hand, we observed that the performance of these fits is not overwhelmingly good such that in our opinion no conclusive statement neither in favour nor against the $O(4)$ scenario is possible at the present stage of the project. Including more (preferably smaller) masses to the analysis would thus be favourable in order to better understand the role of the scaling violations. Possibly, an investigation of the renormalised chiral condensate could improve the comparison as we expect that lattice artifacts are reduced in comparison to the unrenormalised case considered so far.

In chapter 6 we have presented our studies of the thermodynamic equation of state for two out of the four studied values of the pseudoscalar mass. We have introduced the trace anomaly in conjunction with the integral technique as the quantity and method of choice for the evaluation of the related thermodynamic observables pressure and energy density. We have explained to the reader how the trace anomaly is calculated in the twisted mass setup and have discussed a tree-level correction to the trace anomaly. We found it effective for the reduction of lattice artifacts and it has made possible a smooth interpolation of the interaction measure for different lattice discretisations N_τ. For several values of the temperature it was then shown that, as far as we are able to say at present, the tree-level corrected trace anomaly yields the same value when extrapolated to the continuum as the uncorrected one. We are thus confident that it works in our case. However, we amend that a thorough study of the temperature dependence of the correction factors should be conducted in order to check in which range a temperature independent correction, as was done here, is sufficient and in order to maybe improve the method further. For the future a further improvement of the trace anomaly for the smaller out of the two mass values is desirable especially at low temperatures. We try to achieve this goal by collecting more statistics both at finite and at vanishing temperature and by possibly adding some $N_\tau = 14$ points. From the corrected trace anomaly we furthermore have evaluated the pressure and energy density as well as the speed of sound of the hot medium in a subsequent step. Our results for the thermodynamic equation of state have been compared both to the free gas Stefan-Boltzmann limit as well as to results found in literature. We have added a small comparison of the precision of our results in contrast to the precision achieved in a simulation employing staggered quarks. Admittedly, without a dynamical *strange* quark included the results we present for the $N_f = 2$ case are of limited relevance for phenomenological application in terms of input to hydrodynamical modelling of the quark-gluon plasma. Nevertheless, our results can be beneficial for judging the contribution of the heaviest of the three light flavours to thermodynamics. In this sense turning to the $N_f = 2 + 1 + 1$ twisted mass action as

is done successfully in the $T = 0$ case is of course recommended for the future, although we expect it to be very challenging. As we have found in this work it is not sufficient to have only a small amount of $T = 0$ lattices at just a few values of the gauge coupling. Thinking of the necessary $T = 0$ subtraction for the trace anomaly it is unavoidable to have a good precision also at vanishing temperature especially towards large values of the temporal lattice extent.

A Evaluation of Fermionic Observables

In what follows we will present details of how we have estimated fermionic quantities using noise techniques. We will also give the details of matrix conventions that have been in use throughout this work.

As the Wilson Dirac operator D_{W} Eq. (2.7) fulfils what is called γ_5-hermiticity

$$D_{\mathrm{W}}^{\dagger} = \gamma_5 D_{\mathrm{W}} \gamma_5 \tag{A.1}$$

one finds straight forwardly the following identity for the *up* component (D_u) and *down* component (D_d) of the twisted-mass Dirac operator Eq. (2.6)

$$\gamma_5 D_u \gamma 5 = D_d^{\dagger} \, . \tag{A.2}$$

Note that the † operation also interchanges the space-time coordinates in above formula such that we obtain the following relation between the *up* and *down* type propagators D_u^{-1} and D_d^{-1}:

$$\gamma_5 D_u^{-1}(x,y)\gamma_5 = (D_d^{-1}(y,x))^{\dagger} \, , \tag{A.3}$$

which is useful to reduce the cost of Dirac matrix inversions by a factor of two, as it is sufficient to calculate the *up* propagators. Furthermore, it is useful to calculate $D_u^{-1}(x,y)$ by means of stochastic sources ξ^r which fulfil in-average normality in both the space-time coordinates as well as in the spin colour indices:

$$\delta(z,y) = \lim_{R\to\infty} \frac{1}{R} \sum_{r=1}^{R} \xi^r(z)(\xi^r(y))^{\dagger} \, . \tag{A.4}$$

With the help of the noise vectors ξ one can evaluate $D_u^{-1}(x,y)$ stochastically as follows:

$$\begin{aligned} \left(D_u^{-1}(x,y)\right)_{ab} &= \left(D_u^{-1}(x,z)\delta(z,y)\right)_{ab} \\ &= \lim_{R\to\infty} \frac{1}{R} \sum_{r=1}^{R} \left(\phi^r(x)\right)_a \left(\xi^r(y)^{\dagger}\right)_b \, , \end{aligned} \tag{A.5}$$

where $a, b \ldots$ represent both the spin and colour indices and where ϕ^r is given as the solution of the equation

$$\xi^r(x) = D_u(x,y)\phi^r(y) \, . \tag{A.6}$$

Note that if the limit of infinitely many sources is not taken, $D_u^{-1}(x,y)$ is only correct

up to noise terms that vanish for $R \to \infty$.

It is further advantageous, especially for disconnected quantities (such as e. g. $\left\langle \bar{\psi}\psi \right\rangle$), to make use of what is called the one-end trick [B$^+$08b] which arises from combining the identities

$$D_d - D_u = -4\ i\kappa(a\mu)\gamma_5 \tag{A.7}$$

and

$$D_d^{-1}(D_d - D_u)D_u^{-1} = D_u^{-1} - D_d^{-1}\ . \tag{A.8}$$

From these one obtains for the difference of *up* and *down* propagators:

$$\begin{aligned} D_u^{-1} - D_d^{-1} &= -4i\ \kappa\ (a\mu)D_d^{-1}\gamma_5 D_u^{-1} \\ &= -4i\ \kappa\ (a\mu)\gamma_5 (D_u^{-1})^\dagger D_u^{-1}\ , \end{aligned} \tag{A.9}$$

which has been found to improve the signal to noise ratio for disconnected contributions to mesons [B$^+$08b].

A.1 Determination of the Chiral Condensate

Starting with the definition of the chiral condensate in the twisted basis Eq. (3.7) and omitting the normalisation with respect to the lattice volume $1/(N_\tau N_\sigma^3)$ we have:

$$\begin{aligned} \left\langle \bar{\psi}\psi \right\rangle &\propto \left\langle \bar{\chi} i\gamma_5 \tau^3 \chi \right\rangle \\ &= -\left\langle \mathrm{Tr}\left(i\gamma_5 \left(D_u^{-1}(x,x) - D_d^{-1}(x,x) \right) \right) \right\rangle \\ &= 2\ \mathrm{Im}\left\langle \mathrm{Tr}\left(\gamma_5 D_u^{-1}(x,x) \right) \right\rangle \\ &= 2\ \mathrm{Im}\left\langle \frac{1}{R}\sum_r (\phi^r(x))_a^\dagger \left(\gamma_5 \xi^r(x)\right)_a \right\rangle + \text{noise}\ , \end{aligned} \tag{A.10}$$

where we used γ_5-hermiticity Eq. (A.3) in the intermediate step. In the last step we have substituted Eq. (A.5) in order to estimate the quantity with the help of stochastic sources. Alternatively we could rewrite the second line of above equations with the help of Eq. (A.9) which yields

$$\begin{aligned} &-\left\langle \mathrm{Tr}\left(i\gamma_5 \left(D_u^{-1}(x,x) - D_d^{-1}(x,x) \right) \right) \right\rangle \\ &\qquad = -4\ \kappa\ (a\mu) \left\langle \frac{1}{R}\sum_r \left((\phi^r(x))^\dagger \phi^r(x) \right) \right\rangle + \text{noise}\ . \end{aligned} \tag{A.11}$$

For $T > 0$ we have made use of Eq. (A.11) with volume sources of Gaussian noise, while for $T = 0$ we have used Eq. (A.10) with volume sources of $Z(2)$ noise (in both real and imaginary spinor components).

A.2 Determination of $\langle\bar{\chi}D_{\mathrm{W}}\chi\rangle$

The evaluation of $\langle\bar{\chi}D_{\mathrm{W}}\chi\rangle$ from stochastic estimators Eq. (A.5) proceeds as follows:

$$\begin{aligned}\langle\bar{\chi}D_{\mathrm{W}}\chi\rangle &= -\left\langle \mathrm{Tr}\left(\left(D_u^{-1}+D_d^{-1}\right)D_{\mathrm{W}}\right)\right\rangle \\ &= -\left\langle \mathrm{Tr}\left(D_u^{-1}D_{\mathrm{W}}+(D_u^{-1})^{\dagger}D_{\mathrm{W}}^{\dagger}\right)\right\rangle \\ &= -2\ \mathrm{Re}\left\langle \mathrm{Tr}\left(D_u^{-1}D_{\mathrm{W}}\right)\right\rangle \\ &= -2\ \mathrm{Re}\left\langle \frac{1}{R}\sum_r(\phi^r(x))_a^{\dagger}(D_{\mathrm{W}}\xi^r)_a(x)\right\rangle + \text{noise}\ ,\end{aligned} \tag{A.12}$$

where again γ_5-hermiticity Eq. (A.3) is used in an intermediate step.

A.3 Matrix Conventions

- The Pauli matrices:

$$\tau^1=\begin{pmatrix}0&1\\1&0\end{pmatrix}\quad \tau^2=\begin{pmatrix}0&-i\\i&0\end{pmatrix}\quad \tau^3=\begin{pmatrix}1&0\\0&-1\end{pmatrix} \tag{A.13}$$

- The γ-matrices:

$$\begin{aligned}\gamma_0&=\begin{pmatrix}0&0&-1&0\\0&0&0&-1\\-1&0&0&0\\0&-1&0&0\end{pmatrix} \quad \gamma_1=\begin{pmatrix}0&0&0&-i\\0&0&-i&0\\0&+i&0&0\\+i&0&0&0\end{pmatrix}\\ \gamma_2&=\begin{pmatrix}0&0&0&-1\\0&0&+1&0\\0&+1&0&0\\-1&0&0&0\end{pmatrix} \quad \gamma_3=\begin{pmatrix}0&0&-i&0\\0&0&0&+i\\+i&0&0&0\\0&-i&0&0\end{pmatrix}\\ \gamma_5&=\begin{pmatrix}+1&0&0&0\\0&+1&0&0\\0&0&-1&0\\0&0&0&-1\end{pmatrix}\end{aligned} \tag{A.14}$$

B Hybrid Monte Carlo on GPUs

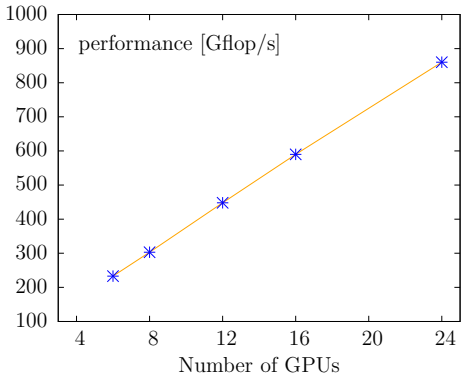

Figure 2.1: Scaling test of the GPU code parallelised in time direction only on different partitions including up to 24 GPUs of the JuDGE system [JuD12]. The lattice size has been $48^3 \times 96$ and nearly linear scaling is achieved.

Today's Graphics Processing Units (GPUs) become a more and more attractive hardware platform for the field of high performance computing. This is mainly due to the fact that these units (that should be seen as accelerator cards within a standard PC host) can deliver a multiple of the performance a standard multi-core processor can deliver and can achieve a better Watt/flop ratio. Furthermore, GPUs have become increasingly easy to program as the main manufacturers (NVIDIA and AMD) are supplying software development kits (such as CUDA [NVI12] or openCL [Khr12]). No special graphics related programming language needs to be used any more as was necessary in the pioneering work by Egri et al. ([EFH$^+$07]), which has opened the field of GPUs to the QCD community. However, basic knowledge of standard *C* or *fortran* is now enough.

In the past the main drawback for the use of GPUs was the fact that only calculations in single precision floating point arithmetics could be done efficiently on these devices[1] Therefore, one has to rely on mixed-precision algorithms in order to effectively obtain a double precision result using only single precision arithmetics. Such algorithms have been reported in Ref. [CBB$^+$10]. There have also been discussed the most crucial optimisations that are to be done in order to use the accelerating unit efficiently. For the inversion of the lattice Dirac operator (defined for the twisted mass action in Eq. (2.6)) these optimisations are mainly related to the reduction of memory accesses and include:

1. Reconstruction of the link fields U_μ from alternatively 12 or 8 numbers using the

[1] This constraint has been relaxed though with the release of NVIDIA's Fermi GPUs.

symmetries of an $SU(3)$ matrix,

2. Use of an alternative γ-matrix basis where γ_0 is diagonal $\mathrm{diag}(1, 1, -1, -1)$ such that when applying $(\mathbb{1} \pm \gamma_0)$ to a spinor χ only half of the spinor has to be loaded.

3. Gauge fixing to temporal gauge before the inversion on the device i. e. setting the temporal links to $U_0 \equiv \mathbb{1}$ for all but one (due to periodic boundary conditions) time slices.

The second optimisation also improves the communication when parallelising the lattice in the temporal direction in between different nodes of a parallel system. We have implemented the standard conjugate gradient algorithm (see e. g. Ref. [DD06]) in single precision for the even-odd preconditioned twisted mass Dirac matrix with above optimisations on GPU. Defect correction running on CPU (c. f. algorithm 1 of Ref. [CBB$^+$10]) is used in order to achieve a double precision result for the propagator. We have included the implementation into the ETMC code [UJSW06]. The performance one may obtain with this code on different types of GPUs belonging to NVIDIA's Fermi product series is:

GPU	performance [Gflop/s]
GTX 580	190
Tesla M2090	127

.

The performance of the MPI parallelised version of the code has been investigated on the JuDGE system in Jülich [JuD12] by means of a scaling test[2] on a $48^3 \times 96$ lattice employing different partitions of the system including in between 6 and 24 GPUs. We achieve nearly linear scaling as can be seen in Fig. 2.1.

Furthermore, the most costly parts of the calculation of gauge forces within the hybrid Monte Carlo algorithm have been ported to GPU, namely the calculation of the staples of plaquette and rectangle terms of the gauge action.

[2]We are grateful to C. Urbach for conducting this test on the JuDGE system.

C Tables of Simulations

In the following we provide lists that give further details about simulation parameters, temperature and some measured observables for the runs performed at $T > 0$. Furthermore, the achieved statistics in terms of number of trajectories of our different finite temperature simulations will be shown. Where not otherwise indicated we have used a Monte Carlo time step of $\tau_{\mathrm{MD}} = 1.0$ for these simulations.

Furthermore, we list the $T = 0$ simulations needed for renormalisation of finite temperature results. These were performed at masses corresponding to the B and D ensembles.

For the details about the ETMC ensembles that have been used we refer the reader to [B$^+$10a]. We have made advantage of all ensembles listed in this reference, fully using the available statistics. Additionally to the ensembles listed in Ref. [B$^+$10a] we use an ensemble at $\beta = 4.35$, $a\mu = 0.00175$ at $N_\tau \times N_\sigma^3 = 64 \times 32^3$ (private communication with E. Garcia Ramos) with the following parameters:

$$am_{\mathrm{PS}} = 0.0748(17), \quad \left(\frac{r_0}{a}\right) = 9.9(2) \ .$$

N_τ	N_σ	β	κ	$a\mu$	T[MeV]	Re(L)	$\langle\bar{\psi}\psi\rangle$ $(\cdot 10^2)$	# traj.
12	32	3.840	0.162731	0.00391	187	$6.1(3)\cdot 10^{-4}$	2.837(11)	3471
		3.860	0.162081	0.00380	193	$6.7(3)\cdot 10^{-4}$	2.637(10)	7114
		3.880	0.161457	0.00370	199	$8.8(3)\cdot 10^{-4}$	2.432(13)	3891
		3.900	0.160856	0.00360	205	$9.8(3)\cdot 10^{-4}$	2.253(15)	6666
		3.930	0.159998	0.00346	215	$1.40(4)\cdot 10^{-3}$	1.992(13)	3947
		3.945	0.159586	0.00339	220	$1.60(4)\cdot 10^{-3}$	1.853(23)	4839
		3.9525	0.159385	0.00335	222	$1.67(3)\cdot 10^{-3}$	1.829(19)	5962
		3.960	0.159187	0.00332	225	$1.86(4)\cdot 10^{-3}$	1.755(19)	6112
		3.9675	0.158991	0.00328	228	$1.98(3)\cdot 10^{-3}$	1.722(14)	7112
		3.975	0.158798	0.00325	230	$2.06(4)\cdot 10^{-3}$	1.676(13)	4505
		3.990	0.158421	0.00319	235	$2.45(4)\cdot 10^{-3}$	1.578(15)	4796

Table C.1: Simulation parameters for the A ensemble. Temperature values are from the $a(\beta)$ interpolation (first method). Results for the bare Polyakov loop and the chiral condensate are also shown.

N_τ	N_σ	β	κ	$a\mu$	T[MeV]	Re(L)	$\langle\bar{\psi}\psi\rangle$ $(\cdot 10^2)$	# traj.
12	32	3.8600	0.162081	0.00617	195	$5.9(3)\cdot 10^{-4}$	3.916(11)	12275
		3.8800	0.161457	0.00600	202	$7.3(3)\cdot 10^{-4}$	3.677(10)	12668
		3.9000	0.160856	0.00584	209	$8.7(2)\cdot 10^{-4}$	3.444(09)	9568
		3.9300	0.159998	0.00561	220	$1.24(3)\cdot 10^{-3}$	3.122(14)	12099
		3.9500	0.159452	0.00546	227	$1.51(4)\cdot 10^{-3}$	2.933(15)	5705
		3.9700	0.158927	0.00531	234	$1.95(3)\cdot 10^{-3}$	2.724(10)	9853
		3.9900	0.158421	0.00517	242	$2.20(4)\cdot 10^{-3}$	2.557(14)	8968
		3.9950	0.158297	0.00513	244	$2.31(4)\cdot 10^{-3}$	2.515(12)	6486
		4.0000	0.158175	0.00510	246	$2.51(4)\cdot 10^{-3}$	2.464(12)	6298
		4.0050	0.158053	0.00506	248	$2.54(5)\cdot 10^{-3}$	2.438(10)	7353
		4.0100	0.157933	0.00503	250	$2.70(5)\cdot 10^{-3}$	2.391(10)	9523
		4.0125	0.157874	0.00501	251	$2.81(4)\cdot 10^{-3}$	2.365(11)	10139
		4.0150	0.157814	0.00499	251	$2.84(5)\cdot 10^{-3}$	2.353(10)	8950
		4.0175	0.157755	0.00498	252	$2.82(4)\cdot 10^{-3}$	2.346(10)	11673
		4.0200	0.157696	0.00496	253	$2.89(4)\cdot 10^{-3}$	2.328(07)	10003
		4.0250	0.157579	0.00493	255	$3.02(4)\cdot 10^{-3}$	2.288(10)	9878
		4.0300	0.157463	0.00489	257	$3.10(4)\cdot 10^{-3}$	2.251(09)	6145
		4.0400	0.157235	0.00483	261	$3.39(5)\cdot 10^{-3}$	2.186(07)	6080
		4.0700	0.156573	0.00463	273	$4.00(8)\cdot 10^{-3}$	2.026(10)	679
		4.1000	0.155945	0.00445	285	$4.83(9)\cdot 10^{-3}$	1.894(04)	7837
		4.1500	0.154969	0.00422	305	$6.17(7)\cdot 10^{-3}$	1.736(03)	4080
		4.2000	0.154073	0.00396	326	$7.57(8)\cdot 10^{-3}$	1.583(02)	4640
		4.2500	0.153247	0.00372	347	$9.17(7)\cdot 10^{-3}$	1.451(03)	4160
		4.3500	0.151740	0.00316	391	$1.21(1)\cdot 10^{-2}$	1.185(01)	4334

Table C.2: Simulation parameters for the B12 ensemble. Temperature values are from the $\left(\frac{r_X}{a}\right)(\beta)$ interpolation (second method). Results for the bare Polyakov loop and the chiral condensate are also shown.

N_τ	N_σ	β	κ	$a\mu$	T[MeV]	Re(L)	$\langle\bar{\psi}\psi\rangle$ $(\cdot 10^2)$	# traj.
10	32	3.760	0.165607	0.00689	193	$1.57(07) \cdot 10^{-3}$	5.146(10)	7760
		3.780	0.164844	0.00672	201	$1.80(10) \cdot 10^{-3}$	4.769(15)	3328
		3.800	0.164111	0.00655	209	$2.25(06) \cdot 10^{-3}$	4.398(19)	3097
		3.820	0.163407	0.00639	217	$2.60(10) \cdot 10^{-3}$	4.091(17)	3516
		3.840	0.162731	0.00623	225	$3.22(06) \cdot 10^{-3}$	3.783(18)	3279
		3.865	0.161923	0.00600	236	$4.69(07) \cdot 10^{-3}$	3.365(19)	3450
		3.870	0.161766	0.00600	238	$4.42(08) \cdot 10^{-3}$	3.357(14)	5900
		3.875	0.161611	0.00600	240	$4.59(09) \cdot 10^{-3}$	3.351(18)	3600
		3.880	0.161457	0.00600	242	$4.78(23) \cdot 10^{-3}$	3.251(44)	8759
		3.885	0.161304	0.00600	244	$4.86(10) \cdot 10^{-3}$	3.222(40)	6400
		3.890	0.161153	0.00600	247	$5.13(13) \cdot 10^{-3}$	3.258(36)	7789
		3.895	0.161004	0.00600	249	$5.50(11) \cdot 10^{-3}$	3.143(24)	4450
		3.900	0.160856	0.00600	251	$5.75(11) \cdot 10^{-3}$	3.101(20)	5973
		3.910	0.160564	0.00600	255	$5.75(12) \cdot 10^{-3}$	3.085(39)	7250
		3.930	0.159998	0.00600	264	$7.17(10) \cdot 10^{-3}$	2.967(14)	8050
		3.970	0.158926	0.00529	281	$8.42(13) \cdot 10^{-3}$	2.465(07)	7276
		4.050	0.157010	0.00479	318	$1.24(02) \cdot 10^{-2}$	2.060(03)	8716
		4.100	0.155945	0.00449	342	$1.44(03) \cdot 10^{-2}$	1.873(04)	1519
		4.200	0.154073	0.00396	391	$2.00(02) \cdot 10^{-2}$	1.564(01)	4000
		4.350	0.151740	0.00326	469	$2.87(02) \cdot 10^{-2}$	1.220(01)	2235

Table C.3: Same as in table C.2 for B10.

N_τ	N_σ	β	κ	$a\mu$	T[MeV]	Re(L)	$\langle\bar{\psi}\psi\rangle$ $(\cdot 10^2)$	# traj.
8	28	3.76	0.165608	0.006888	242	$1.21(2)\cdot 10^{-2}$	4.248(70)	1892
		3.80	0.164111	0.006551	262	$1.58(2)\cdot 10^{-2}$	3.590(12)	5208
		3.85	0.162401	0.006153	288	$2.01(2)\cdot 10^{-2}$	3.081(07)	4444
		3.90	0.160856	0.005779	314	$2.46(2)\cdot 10^{-2}$	2.723(04)	3007
		3.97	0.158934	0.005292	352	$3.08(2)\cdot 10^{-2}$	2.348(03)	3148
		4.01	0.157955	0.005032	375	$3.45(2)\cdot 10^{-2}$	2.169(02)	2746
		4.05	0.157010	0.004785	398	$3.80(2)\cdot 10^{-2}$	2.012(01)	3792
		4.10	0.155952	0.004492	428	$4.27(2)\cdot 10^{-2}$	1.837(01)	3581
		4.20	0.154073	0.003960	489	$5.12(2)\cdot 10^{-2}$	1.546(01)	3750
		4.35	0.151740	0.003275	587	$6.56(2)\cdot 10^{-2}$	1.168(01)	4200
6	32	3.80	0.164111	0.006551	349	$7.17(3)\cdot 10^{-2}$	3.212(02)	949
		3.82	0.163406	0.006389	363	$7.38(3)\cdot 10^{-2}$	3.076(03)	1069
		3.84	0.162730	0.006231	377	$7.70(2)\cdot 10^{-2}$	2.945(01)	1271
		3.86	0.162080	0.006076	390	$7.98(2)\cdot 10^{-2}$	2.824(01)	1611
		3.90	0.160856	0.005779	419	$8.60(2)\cdot 10^{-2}$	2.603(01)	1976
		3.97	0.158934	0.005292	470	$9.62(2)\cdot 10^{-2}$	2.273(01)	2034
		4.05	0.157010	0.004785	531	$1.075(2)\cdot 10^{-1}$	1.963(01)	2151
		4.10	0.155952	0.004492	570	$1.115(3)\cdot 10^{-1}$	1.798(01)	1025
4	32	3.80	0.164111	0.006551	524	$2.507(1)\cdot 10^{-1}$	2.9518(3)	2493
		3.86	0.162080	0.006076	586	$2.605(1)\cdot 10^{-1}$	2.6245(2)	2233
		3.90	0.160856	0.005779	628	$2.669(1)\cdot 10^{-1}$	2.4324(2)	1737
		3.97	0.158934	0.005292	705	$2.782(1)\cdot 10^{-1}$	2.1392(2)	1547

Table C.4: Same as in table C.2 and table C.3 for all remaining B mass ensembles.

N_τ	N_σ	β	κ	$a\mu$	T[MeV]	Re(L)	$\langle\bar{\psi}\psi\rangle$ $(\cdot 10^2)$	# traj.
12	32	3.90	0.160856	0.008212	205	$8.4(5) \cdot 10^{-4}$	4.65(1)	0/3050/0
		3.93	0.159997	0.008007	215	$1.16(4) \cdot 10^{-3}$	4.31(2)	0/3101/0
		3.95	0.159452	0.007792	221	$1.35(3) \cdot 10^{-3}$	4.07(2)	0/5822/0
		3.97	0.158926	0.007521	228	$1.63(3) \cdot 10^{-3}$	3.82(1)	0/9179/0
		3.99	0.158421	0.007379	235	$2.11(5) \cdot 10^{-3}$	3.60(2)	0/5151/0
		4.01	0.157933	0.007180	243	$2.48(5) \cdot 10^{-3}$	3.41(2)	4640/0/5432
		4.02	0.157696	0.007084	246	$2.49(6) \cdot 10^{-3}$	3.36(3)	5120/0/3324
		4.03	0.157463	0.006988	250	$2.92(7) \cdot 10^{-3}$	3.25(3)	6240/0/3308
		4.04	0.157235	0.006893	254	$3.20(6) \cdot 10^{-3}$	3.15(3)	4080/0/3308
		4.05	0.157010	0.006800	258	$3.57(8) \cdot 10^{-3}$	3.06(2)	5240/0/0
		4.06	0.156789	0.006708	262	$3.79(5) \cdot 10^{-3}$	2.96(1)	6523/0/0
		4.07	0.156573	0.006617	267	$4.20(5) \cdot 10^{-3}$	2.88(1)	3389/1200/0
		4.10	0.155946	0.006385	278	$4.92(7) \cdot 10^{-3}$	2.72(1)	0/2160/0
		4.20	0.154073	0.005627	320	$7.4(2) \cdot 10^{-3}$	2.25(1)	0/2078/0

Table C.5: Simulation parameters for the C ensemble. The sum of trajectories given in the last column corresponds to three different runs with Monte Carlo time step $\tau_{\mathrm{MD}} = 0.5$ (run on APE in Rome), $\tau_{\mathrm{MD}} = 1.0$ (run on HLRN and GPUs) and $\tau_{\mathrm{MD}} = 1.0$ (run on LOEWE in Frankfurt). Temperature values are from the $a(\beta)$ interpolation (first method). Results for the bare Polyakov loop and the chiral condensate are also shown.

N_τ	N_σ	β	κ	$a\mu$	T[MeV]	Re(L)	$\langle\bar{\psi}\psi\rangle$ $(\cdot 10^1)$	# traj.
10	24	3.76	0.165608	0.022175	193	$0.8(4)\cdot 10^{-3}$	1.356(2)	6184
		3.80	0.164111	0.021000	210	$1.20(4)\cdot 10^{-3}$	1.219(1)	5955
		3.85	0.162401	0.019618	230	$1.96(7)\cdot 10^{-3}$	1.065(2)	6162
		3.90	0.160856	0.018327	251	$3.7(2)\cdot 10^{-3}$	0.932(2)	5286
		3.97	0.158934	0.016661	282	$7.4(2)\cdot 10^{-2}$	0.774(2)	6389
		4.05	0.157010	0.015240	319	$1.22(2)\cdot 10^{-2}$	0.655(1)	6873
		4.20	0.154073	0.012612	391	$2.03(2)\cdot 10^{-2}$	0.498(1)	6759
10	32	4.60	0.148758	0.007594	612	$4.31(4)\cdot 10^{-2}$	0.263(1)	1213
8	20	3.65	0.17020000	0.025173	189	-	1.799(1)	21656
		3.70	0.16806278	0.024063	213	$4.51(7)\cdot 10^{-3}$	1.576(2)	18240
		3.72	0.16721928	0.023416	222	$5.29(9)\cdot 10^{-3}$	1.483(2)	16961
		3.74	0.16639961	0.022787	232	$6.46(8)\cdot 10^{-3}$	1.394(2)	24771
		3.76	0.16560755	0.022175	242	$8.1(2)\cdot 10^{-3}$	1.310(3)	18392
		3.78	0.16484461	0.021580	252	$9.7(2)\cdot 10^{-3}$	1.227(2)	19091
		3.80	0.16411100	0.021000	262	$1.22(2)\cdot 10^{-2}$	1.146(3)	33329
		3.82	0.16340626	0.020436	272	$1.44(2)\cdot 10^{-2}$	1.078(2)	22399
		3.84	0.16272951	0.019887	282	$1.65(2)\cdot 10^{-2}$	1.019(2)	20450
		3.85	0.16240130	0.019618	288	$1.80(2)\cdot 10^{-2}$	0.986(1)	27895
		3.86	0.16207968	0.019353	293	$1.94(2)\cdot 10^{-2}$	0.958(2)	24244
		3.87	0.16176448	0.019091	298	$2.02(2)\cdot 10^{-2}$	0.933(2)	23330
		3.88	0.16145558	0.018833	303	$2.16(2)\cdot 10^{-2}$	0.910(2)	21986
		3.90	0.160856	0.018327	314	$2.33(2)\cdot 10^{-2}$	0.8653(7)	23455
		3.92	0.160280	0.017835	325	$2.58(2)\cdot 10^{-2}$	0.8252(7)	22831
		3.94	0.159726	0.017356	336	$2.73(2)\cdot 10^{-2}$	0.7885(6)	8812
		3.96	0.159193	0.016890	347	$2.93(2)\cdot 10^{-2}$	0.7548(5)	10974
		3.98	0.158681	0.016436	358	$3.12(2)\cdot 10^{-2}$	0.7234(4)	10889
		4.05	0.157010	0.015240	398	$3.80(2)\cdot 10^{-2}$	0.6404(2)	14180
		4.10	0.155952	0.014309	428	$4.24(2)\cdot 10^{-2}$	0.5851(2)	10233
		4.20	0.154073	0.012612	489	$5.17(2)\cdot 10^{-2}$	0.49219(5)	10861
		4.25	0.153238	0.011839	521	$5.62(2)\cdot 10^{-2}$	0.4530(1)	11573
		4.35	0.151740	0.010431	587	$6.52(2)\cdot 10^{-2}$	0.48505(3)	12089
8	32	4.60	0.148758	0.007594	765	$8.88(2)\cdot 10^{-2}$	0.26145(1)	4349
6	16	3.65	0.170200	0.025173	252	$4.29(5)\cdot 10^{-2}$	1.538(4)	10028
		3.70	0.168063	0.024063	284	$5.48(6)\cdot 10^{-2}$	1.334(2)	10198
		3.76	0.165608	0.022175	322	$6.44(5)\cdot 10^{-2}$	1.136(1)	13090
		3.80	0.164111	0.021000	349	$7.03(4)\cdot 10^{-2}$	1.030(1)	11773
		3.85	0.162401	0.019618	383	$7.80(5)\cdot 10^{-2}$	0.9187(3)	10516
		3.90	0.160856	0.018327	419	$8.50(5)\cdot 10^{-2}$	0.8250(2)	11207
		3.97	0.158934	0.016661	470	$9.53(5)\cdot 10^{-2}$	0.7155(1)	11109
		4.05	0.157010	0.015240	531	$1.076(4)\cdot 10^{-1}$	0.62522(6)	15926
6	20	4.20	0.154073	0.012612	652	-	0.48317(4)	7568
		4.35	0.151740	0.010431	782	-	0.38220(3)	3881
6	32	3.97	0.158934	0.016661	470	-	0.71530(7)	4315
		4.05	0.157010	0.015240	531	-	0.62516(6)	3637
4	20	4.20	0.154073	0.012612	978	-	0.46027(3)	7893

Table C.6: Simulation parameters for the D ensembles. Temperature values are from the $\left(\frac{r_X}{a}\right)(\beta)$ interpolation (second method).

N_τ N_σ	β	κ	$a\mu$	am_{PS}	$m_{\mathrm{PS}}L$	am_{PCAC}	$\left(\frac{r_0}{a}\right)$	# traj.
24 16	3.65	0.170200	0.007903	0.301(9)	4.8	$1.2(1)\cdot 10^{-2}$	3.14(8)	4635
	3.76	0.165607	0.006888	0.210(8)	3.3	$0.2(1.1)\cdot 10^{-3}$	4.10(3)	5514
48 24	3.85	0.162403	0.006	0.175(2)	4.2	$-1(4)\cdot 10^{-4}$	4.73(6)	744
	3.86	0.162081	0.006166	0.174(2)	4.1	$-2(3)\cdot 10^{-4}$	-	3917
	3.88	0.161457	0.006000	0.170(4)	4.0	$-6(3)\cdot 10^{-4}$	-	3142
	3.93	0.159998	0.005605	0.158(3)	3.7	$-1(3)\cdot 10^{-4}$	-	4142
	3.95	0.159452	0.005455	0.150(3)	3.6	$2(2)\cdot 10^{-4}$	-	3682
	3.99	0.158421	0.005166	0.140(3)	3.3	$-2(3)\cdot 10^{-4}$	-	2990
64 32	3.97	0.158927	0.005308	0.1441(9)	4.6	$-5(2)\cdot 10^{-4}$	5.8(1)	1086
	4.01	0.157933	0.005027	0.135(2)	4.3	$-3(2)\cdot 10^{-4}$	-	426
	4.10	0.155945	0.004447	0.117(2)	3.7	$2(1)\cdot 10^{-4}$	-	1590

Table C.7: Simulation parameters for the $T = 0$ runs at masses corresponding to the mass of the B ensemble. We also show results for the pseudoscalar and PCAC mass as well as $\left(\frac{r_0}{a}\right)$ where calculated.

N_τ N_σ	β	κ	$a\mu$	am_{PS}	$m_{\mathrm{PS}}L$	am_{V}	am_{PCAC}	$\left(\frac{r_0}{a}\right)$	# traj.
40 16	3.65	0.170200	0.025173	0.425(7)	6.8	0.75(2)	$2(2)\cdot 10^{-2}$	3.28(5)	2735
40 20	3.70	0.168092	0.024062	0.397(7)	7.9	0.707(8)	$-4.8(9)\cdot 10^{-3}$	3.64(5)	7359
	3.76	0.165608	0.022175	0.354(9)	7.0	0.64(2)	$-2.1(9)\cdot 10^{-3}$	3.95(3)	7405
	3.80	0.164111	0.021000	0.338(4)	6.7	0.618(8)	$-1.8(9)\cdot 10^{-3}$	4.17(2)	5319
	3.85	0.162403	0.019618	0.311(6)	6.2	0.57(2)	$-1.9(8)\cdot 10^{-3}$	4.59(5)	4880
	3.90	0.160856	0.018327	0.292(6)	5.8	0.51(1)	$-1.9(9)\cdot 10^{-3}$	4.84(7)	2522
	3.97	0.158926	0.016661	0.263(4)	5.2	0.491(7)	$-1.7(8)\cdot 10^{-3}$	5.43(6)	3849
	4.05	0.157010	0.0152	0.233(8)	4.6	0.41(1)	$-3(2)\cdot 10^{-3}$	6.2(1)	4180
	4.20	0.154073	0.0127	0.20(2)	4.0	0.374(9)	$-3(2)\cdot 10^{-3}$	7.7(2)	3363
	4.35	0.151740	0.0105	0.176(8)	3.5	0.281(7)	$-0.2(9)\cdot 10^{-3}$	9.3(4)	3708
20 20	3.74	0.166401	0.022787	-	-	-	-	-	1437
	3.93	0.159997	0.017594	-	-	-	-	-	677
48 24	4.20	0.154073	0.01	0.16(2)	3.8	0.336(9)	$4(12)\cdot 10^{-4}$	7.6(2)	810
	4.35	0.151740	0.006	0.14(3)	3.3	0.273(4)	$-8(20)\cdot 10^{-4}$	9.6(3)	977
40 32	4.6	0.148758	0.007594	-	-	-	-	11.4(6)	1235

Table C.8: Same as in table C.7 for the $T = 0$ runs at masses corresponding to the mass of the D ensemble. Additionally we show results for the vector meson mass where calculated.

Bibliography

[A+87] Albanese, M.; et al. (APE Collaboration): Glueball masses and string tension in lattice QCD. In: *Phys.Lett.*, volume B192:pp. 163–169, 1987. doi: 10.1016/0370-2693(87)91160-9.

[A+05] Adams, J.; et al. (STAR Collaboration): Azimuthal anisotropy in Au+Au collisions at s(NN)**(1/2) = 200-GeV. In: *Phys.Rev.*, volume C72:p. 014904, 2005. [nucl-ex/0409033].

[ABMS06] Andronic, A.; Braun-Munzinger, P.; Stachel, J.: Hadron production in central nucleus-nucleus collisions at chemical freeze-out. In: *Nucl.Phys.*, volume A772:pp. 167–199, 2006. doi:10.1016/j.nuclphysa.2006.03.012. [nucl-th/0511071].

[ADF+09] Aoki, S., Y. Borsanyi; Durr, S.; Fodor, Z.; Katz, S. D.; et al.: The QCD transition temperature: results with physical masses in the continuum limit II. In: *JHEP*, volume 0906:p. 088, 2009. doi:10.1088/1126-6708/2009/06/088. [arXiv:0903.4155].

[AEF+06] Aoki, Y.; Endrodi, G.; Fodor, Z.; Katz, S.D.; Szabo, K.K.: The Order of the quantum chromodynamics transition predicted by the standard model of particle physics. In: *Nature*, volume 443:pp. 675–678, 2006. doi:10.1038/nature05120. [hep-lat/0611014].

[AFKS06] Aoki, Y.; Fodor, Z.; Katz, S.D.; Szabo, K.K.: The QCD transition temperature: Results with physical masses in the continuum limit. In: *Phys.Lett.*, volume B643:pp. 46–54, 2006. doi:10.1016/j.physletb.2006.10.021. [hep-lat/0609068].

[AK+01a] Ali Khan, A.; et al. (CP-PACS collaboration): Equation of state in finite temperature QCD with two flavors of improved Wilson quarks. In: *Phys.Rev.*, volume D64:p. 074510, 2001. doi:10.1103/PhysRevD.64.074510. [hep-lat/0103028].

[AK+01b] Ali Khan, A.; et al. (CP-PACS Collaboration): Phase structure and critical temperature of two flavor QCD with renormalization group improved gauge action and clover improved Wilson quark action. In: *Phys.Rev.*, volume D63:p. 034502, 2001. doi:10.1103/PhysRevD.63.034502. [hep-lat/0008011].

[Aok84] Aoki, S.: New phase structure for lattice QCD with Wilson fermions. In: *Phys. Rev.*, volume D30:p. 2653, 1984. doi:10.1103/PhysRevD.30.2653.

[B+08a] Baron, R.; et al. (ETM Collaboration): Status of ETMC simulations with N(f) = 2+1+1 twisted mass fermions. In: *PoS*, volume LATTICE2008:p. 094, 2008. [arXiv:0810.3807].

[B+08b] Boucaud, Ph.; et al. (ETM): Dynamical twisted mass fermions with light quarks: Simulation and analysis details. In: *Comput. Phys. Commun.*, volume 179:p. 695, 2008. doi:10.1016/j.cpc.2008.06.013. [arXiv:0803.0224].

[B+10a] Baron, R.; et al. (ETM Collaboration): Light meson physics from maximally twisted mass lattice QCD. In: *JHEP*, volume 1008:p. 097, 2010. doi:10.1007/JHEP08(2010)097. [arXiv:0911.5061].

[B+10b] Borsanyi, S.; et al. (Wuppertal-Budapest Collaboration): Is there still any Tc mystery in lattice QCD? Results with physical masses in the continuum limit III. In: *JHEP*, volume 1009:p. 073, 2010. doi:10.1007/JHEP09(2010)073. [arXiv:1005.3508].

[BBC+09] Bazavov, A.; Bhattacharya, T.; Cheng, M.; Christ, N.H.; DeTar, C.; et al.: Equation of state and QCD transition at finite temperature. In: *Phys.Rev.*, volume D80:p. 014504, 2009. doi:10.1103/PhysRevD.80.014504. [arXiv:0903.4379].

[BBC+12] Bazavov, A.; Bhattacharya, T.; Cheng, M.; DeTar, C.; Ding, H.T.; et al.: The chiral and deconfinement aspects of the QCD transition. In: *Phys.Rev.*, volume D85:p. 054503, 2012. doi:10.1103/PhysRevD.85.054503. [arXiv:1111.1710].

[BEF+10] Borsanyi, S.; Endrodi, G.; Fodor, Z.; Jakovac, A.; Katz, S. D.; et al.: The QCD equation of state with dynamical quarks. In: *JHEP*, volume 1011:p. 077, 2010. doi:10.1007/JHEP11(2010)077. [arXiv:1007.2580].

[BEF+11] Borsanyi, S.; Endrodi, G.; Fodor, Z.; Katz, S. D.; Krieg, S.; et al.: The QCD equation of state and the effects of the charm. In: *PoS*, volume LATTICE2011:p. 201, 2011. [arXiv:1204.0995].

[BHM+10] Bornyakov, V.G.; Horsley, R.; Morozov, S.M.; Nakamura, Y.; Polikarpov, M.I.; et al.: Probing the finite temperature phase transition with N(f) = 2 nonperturbatively improved Wilson fermions. In: *Phys.Rev.*, volume D82:p. 014504, 2010. doi:10.1103/PhysRevD.82.014504. [arXiv:0910.2392].

[BHN+11] Bornyakov, V.G.; Horsley, R.; Nakamura, Y.; Polikarpov, M.I.; Rakow, P.; et al.: Finite temperature phase transition with two flavors of improved Wilson fermions. In: , 2011. [arXiv:1102.4461].

[BIK+11] Burger, F.; Ilgenfritz, E.-M.; Kirchner, M.; Lombardo, M.P.; Müller-Preussker, M.; et al.: The thermal QCD transition with two flavours of twisted mass fermions. In: Revised version to be submitted to *Phys. Rev.* D, 2011. [arXiv:1102.4530].

[BMM+85] Bochicchio, M.; Maiani, L.; Martinelli, G.; Rossi, G. C.; Testa, M.: Chiral symmetry on the lattice with Wilson fermions. In: *Nucl.Phys.*, volume B262:p. 331, 1985. doi:10.1016/0550-3213(85)90290-1.

[BMS07] Braun-Munzinger, P.; Stachel, J.: The quest for the quark-gluon plasma. In: *Nature*, volume 448:pp. 302–309, 2007. doi:10.1038/nature06080.

[BMW09] Braun-Munzinger, P.; Wambach, J.: Colloquium: Phase diagram of strongly interacting matter. In: *Rev.Mod.Phys.*, volume 81:pp. 1031–1050, 2009. doi:10.1103/RevModPhys.81.1031.

[CBB+10] Clark, M.A.; Babich, R.; Barros, K.; Brower, R. C.; Rebbi, C.: Solving Lattice QCD systems of equations using mixed precision solvers on GPUs. In: *Comput.Phys.Commun.*, volume 181:pp. 1517–1528, 2010. doi:10.1016/j.cpc.2010.05.002. [arXiv:0911.3191].

[CCD+06] Cheng, M.; Christ, N.H.; Datta, S.; van der Heide, J.; Jung, C.; et al.: The transition temperature in QCD. In: *Phys.Rev.*, volume D74:p. 054507, 2006. doi:10.1103/PhysRevD.74.054507. [hep-lat/0608013].

[CCD+08] Cheng, M.; Christ, N.H.; Datta, S.; van der Heide, J.; Jung, C.; et al.: The QCD equation of state with almost physical quark masses. In: *Phys.Rev.*, volume D77:p. 014511, 2008. doi:10.1103/PhysRevD.77.014511. [arXiv:0710.0354].

[CEH+10] Cheng, M.; Ejiri, S.; Hegde, P.; Karsch, F.; Kaczmarek, O.; et al.: Equation of state for physical quark masses. In: *Phys. Rev.*, volume D81:p. 054504, 2010. doi:10.1103/PhysRevD.81.054504. [arXiv:0911.2215].

[CP75] Cabibbo, N.; Parisi, G.: Exponential Hadronic Spectrum and Quark Liberation. In: *Phys.Lett.*, volume B59:pp. 67–69, 1975. doi:10.1016/0370-2693(75)90158-6.

[CR00] Chetyrkin, K. G.; Retey, A.: Renormalization and running of quark mass and field in the regularization invariant and MS-bar schemes at three and four loops. In: *Nucl. Phys.*, volume B583:pp. 3–34, 2000. doi:10.1016/S0550-3213(00)00331-X. [hep-ph/9910332].

[Cre07] Creutz, M.: Why rooting fails. In: *PoS*, volume LAT2007:p. 007, 2007. [arXiv:0708.1295].

[DD06] DeGrand, T.; DeTar, C.: *Lattice methods for quantum chromodynamics*. World Scientific, 2006.

[DDGP05] D'Elia, M.; Di Giacomo, A.; Pica, C.: Two flavor QCD and confinement. In: *Phys.Rev.*, volume D72:p. 114510, 2005. doi:10.1103/PhysRevD.72.114510. [hep-lat/0503030].

[DH09] DeTar, C.; Heller, U.M.: QCD thermodynamics from the lattice. In: *Eur.Phys.J.*, volume A41:p. 405, 2009. doi:10.1140/epja/i2009-10825-3. [arXiv:0905.2949].

[DKPR87] Duane, S.; Kennedy, A.D.; Pendleton, B.J.; Roweth, D.: Hybrid Monte Carlo. In: *Phys. Lett.*, volume B195:pp. 216–222, 1987. doi:10.1016/0370-2693(87)91197-X.

[EFH+07] Egri, G. I.; Fodor, Z.; Hoelbling, C.; Katz, S. D.; Nogradi, D.; et al.: Lattice QCD as a video game. In: *Comput.Phys.Commun.*, volume 177:pp. 631–639, 2007. doi:10.1016/j.cpc.2007.06.005. [hep-lat/0611022].

[EKL+09] Ejiri, S.; Karsch, F.; Laermann, E.; Miao, C.; Mukherjee, S.; et al.: On the magnetic equation of state in (2+1)-flavor QCD. In: *Phys.Rev.*, volume D80:p. 094505, 2009. doi:10.1103/PhysRevD.80.094505. [arXiv:0909.5122].

[EM00] Engels, J.; Mendes, T.: Goldstone mode effects and scaling function for the three-dimensional O(4) model. In: *Nucl.Phys.*, volume B572:pp. 289–304, 2000. doi:10.1016/S0550-3213(00)00046-8. [hep-lat/9911028].

[FOU90] Fukugita, M.; Okawa, M.; Ukawa, A.: The issue of the order of the deconfining phase transition in SU(3) lattice gauge theory. In: *Nucl.Phys.Proc.Suppl.*, volume 17:pp. 204–209, 1990. doi:10.1016/0920-5632(90)90238-P.

[FR04] Frezzotti, R.; Rossi, G. C.: Chirally improving Wilson fermions. I: O(a) improvement. In: *JHEP*, volume 08:p. 007, 2004. [hep-lat/0306014].

[GW73] Gross, D.J.; Wilczek, F.: Asymptotically free gauge theories. 1. In: *Phys.Rev.*, volume D8:pp. 3633–3652, 1973. doi:10.1103/PhysRevD.8.3633.

[GW74] Gross, D.J.; Wilczek, F.: Asymptotically free gauge theories. 2. In: *Phys.Rev.*, volume D9:pp. 980–993, 1974. doi:10.1103/PhysRevD.9.980.

[Hag65] Hagedorn, R.: Statistical thermodynamics of strong interactions at high-energies. In: *Nuovo Cim.Suppl.*, volume 3:pp. 147–186, 1965.

[HK01] Hasenfratz, A.; Knechtli, F.: Flavor symmetry and the static potential with hypercubic blocking. In: *Phys.Rev.*, volume D64:p. 034504, 2001. doi:10.1103/PhysRevD.64.034504. [hep-lat/0103029].

[HKH+01] Huovinen, P.; Kolb, P.F.; Heinz, Ulrich W.; Ruuskanen, P.V.; Voloshin, S.A.: Radial and elliptic flow at RHIC: Further predictions. In: *Phys.Lett.*, volume B503:pp. 58–64, 2001. doi:10.1016/S0370-2693(01)00219-2. [hep-ph/0101136].

[HP10] Huovinen, P.; Petreczky, P.: QCD equation of state and hadron resonance gas. In: *Nucl.Phys.*, volume A837:pp. 26–53, 2010. doi:10.1016/j.nuclphysa.2010.02.015. [arXiv:0912.2541].

[IJL+09] Ilgenfritz, E.-M.; Jansen, K.; Lombardo, M.P.; Müller-Preussker, M.; Petschlies, M.; et al. (tmfT): Phase structure of thermal lattice QCD with $N_f = 2$ twisted mass Wilson fermions. In: *Phys. Rev.*, volume D80:p. 094502, 2009. [arXiv:0905.3112].

[JMMU09] Jansen, K.; McNeile, C.; Michael, C.; Urbach, C. (ETM Collaboration): Meson masses and decay constants from unquenched lattice QCD. In: *Phys.Rev.*, volume D80:p. 054510, 2009. doi:10.1103/PhysRevD.80.054510. [arXiv:0906.4720].

[JuD12] JuDGE: *JuDGE: Juelich Dedicated GPU Environment*. Jülich Supercomputing Centre (JSC), 2012. URL http://www.fz-juelich.de/ias/jsc/EN/Expertise/Supercomputers/JUDGE/JUDGE_node.html.

[Kar94] Karsch, F.: Scaling of pseudocritical couplings in two flavor QCD. In: *Phys.Rev.*, volume D49:pp. 3791–3794, 1994. doi:10.1103/PhysRevD.49.3791. [hep-lat/9309022].

[Khr12] Khronos group: *OpenCL*, 2012. URL http://www.khronos.org/opencl/.

[KLP00] Karsch, F.; Laermann, E.; Peikert, A.: The Pressure in two flavor, (2+1)-flavor and three flavor QCD. In: *Phys.Lett.*, volume B478:pp. 447–455, 2000. doi:10.1016/S0370-2693(00)00292-6. [hep-lat/0002003].

[KPS81] Kuti, J.; Polonyi, J.; Szlachanyi, K.: Monte Carlo study of SU(2) gauge Theory at finite temperature. In: *Phys.Lett.*, volume B98:p. 199, 1981. doi:10.1016/0370-2693(81)90987-4.

[Kro07] Kronfeld, A. S.: Lattice gauge theory with staggered fermions: How, where, and why (not). In: *PoS*, volume LAT2007:p. 016, 2007. [arXiv:0711.0699].

[LP03] Laermann, E.; Philipsen, O.: The status of lattice QCD at finite temperature. In: *Ann.Rev.Nucl.Part.Sci.*, volume 53:pp. 163–198, 2003. doi:10.1146/annurev.nucl.53.041002.110609. [hep-ph/0303042].

[LW85a] Lüscher, M.; Weisz, P.: Computation of the action for on-shell improved lattice gauge theories at weak coupling. In: *Phys.Lett.*, volume B158:p. 250, 1985. doi:10.1016/0370-2693(85)90966-9.

[LW85b] Lüscher, M.; Weisz, P.: On-shell improved lattice gauge theories. In: *Commun. Math. Phys.*, volume 97:p. 59, 1985. doi:10.1007/BF01206178.

[MM94] Montvay, I.; Münster, G.: *Quantum fields on a lattice*. Cambridge University Press, 1994.

[MPIJ+09] Müller-Preussker, M.; Ilgenfritz, E.-M.; Jansen, K.; Lombardo, M. P.; Philipsen, O.; et al.: On the phase structure of lattice QCD with twisted-mass Wilson fermions at non-zero temperature. In: *PoS*, volume LAT2009:p. 266, 2009. [arXiv:0912.0919].

[MS81a] McLerran, L. D.; Svetitsky, B.: A Monte Carlo study of SU(2) Yang-Mills theory at finite temperature. In: *Phys.Lett.*, volume B98:p. 195, 1981. doi:10.1016/0370-2693(81)90986-2.

[MS81b] McLerran, L. D.; Svetitsky, B.: Quark liberation at high temperature: A Monte Carlo study of SU(2) gauge theory. In: *Phys.Rev.*, volume D24:p. 450, 1981. doi:10.1103/PhysRevD.24.450.

[Mün04] Münster, G.: On the phase structure of twisted mass lattice QCD. In: *JHEP*, volume 09:p. 035, 2004. doi:10.1088/1126-6708/2004/09/035. [hep-lat/0407006].

[N+10] Nakamura, K.; et al. (Particle Data Group): Review of particle physics. In: *J.Phys.G*, volume G37:p. 075021, 2010. doi:10.1088/0954-3899/37/7A/075021.

[NVI12] NVIDIA: *CUDA toolkit*, 2012. URL http://www.nvidia.com/content/cuda/cuda-toolkit.html.

[Phi10] Philipsen, O.: Lattice QCD at non-zero temperature and baryon density. In: , pp. 273–330, 2010. [arXiv:1009.4089].

[Phi12] Philipsen, O.: The QCD equation of state from the lattice. In: , 2012. [arXiv:1207.5999].

[Pol73] Politzer, H. D.: Reliable perturbative results for strong interactions? In: *Phys.Rev.Lett.*, volume 30:pp. 1346–1349, 1973. doi:10.1103/PhysRevLett.30.1346.

[PS95] Peskin, M. E.; Schroeder, D. V.: *An introduction to quantum field theory*. Westview Press, 1995.

[PV02] Pelissetto, A.; Vicari, E.: Critical Phenomena and Renormalization Group Theory. In: *Phys.Rept.*, volume 368:pp. 549–727, 2002. doi:10.1016/S0370-1573(02)00219-3. [cond-mat/0012164].

[PW84] Pisarski, R. D.; Wilczek, F.: Remarks on the chiral phase transition in chromodynamics. In: *Phys.Rev.*, volume D29:pp. 338–341, 1984. doi:10.1103/PhysRevD.29.338.

[PZ10] Philipsen, O.; Zeidlewicz, L.: Cut-off effects of Wilson fermions on the QCD equation of state to O(g**2). In: *Phys.Rev.*, volume D81:p. 077501, 2010. doi:10.1103/PhysRevD.81.077501. [arXiv:0812.1177].

[R D10] R Development Core Team: *R: A language and environment for statistical computing*. R Foundation for Statistical Computing, Vienna, Austria, 2010. ISBN 3-900051-07-0, URL http://www.R-project.org.

[Rot05] Rothe, H. J.: *Lattice gauge theories*. World Scientific, 2005.

[SBS10] Sarkar, S.; Bikash, S.; Satz, H.: *The physics of the quark-gluon plasma*. Springer Verlag, 2010.

[Shi08] Shindler, A.: Twisted mass lattice QCD. In: *Phys. Rept.*, volume 461:p. 37, 2008. doi:10.1016/j.physrep.2008.03.001. [arXiv:0707.4093].

[Smi02] Smit, J.: *Introduction to quantum fields on a lattice*. Cambridge University Press, 2002.

[Som94] Sommer, R.: A new way to set the energy scale in lattice gauge theories and its applications to the static force and alpha-s in SU(2) Yang-Mills theory. In: *Nucl. Phys.*, volume B411:p. 839, 1994. doi:10.1016/0550-3213(94)90473-1. [hep-lat/9310022].

[SW05] Sharpe, S. R.; Wu, J. M. S.: Twisted mass chiral perturbation theory at next-to-leading order. In: *Phys. Rev.*, volume D71:p. 074501, 2005. doi:10.1103/PhysRevD.71.074501. [hep-lat/0411021].

[SY82] Svetitsky, B.; Yaffe, L. G.: Critical behavior at finite temperature confinement transitions. In: *Nucl.Phys.*, volume B210:p. 423, 1982. doi:10.1016/0550-3213(82)90172-9.

[U+10] Umeda, T.; et al. (WHOT-QCD Collaboration): EOS in 2+1 flavor QCD with improved Wilson quarks by the fixed-scale approach. In: *PoS*, volume LATTICE2010:p. 218, 2010. [arXiv:1011.2548].

[U+12] Umeda, T.; et al. (WHOT-QCD Collaboration): Equation of state in 2+1 flavor QCD with improved Wilson quarks by the fixed scale approach. In: *Phys.Rev.*, volume D85:p. 094508, 2012. doi:10.1103/PhysRevD.85.094508. [arXiv:1202.4719].

[UEA+09] Umeda, T.; Ejiri, S.; Aoki, S.; Hatsuda, T.; Kanaya, K.; et al.: Fixed scale approach to equation of state in lattice QCD. In: *Phys.Rev.*, volume D79:p. 051501, 2009. doi:10.1103/PhysRevD.79.051501. [arXiv:0809.2842].

[UJSW06] Urbach, C.; Jansen, K.; Shindler, A.; Wenger, U.: HMC algorithm with multiple time scale integration and mass preconditioning. In: *Comput. Phys. Commun.*, volume 174:p. 87, 2006. doi:10.1016/j.cpc.2005.08.006. [hep-lat/0506011].

[Urb12] Urbach, Carsten: *'hadron'-Package, Fitting code for lattice QCD in R*, 2012. URL http://www.itkp.uni-bonn.de/~urbach/.

[Vla11] Vladikas, A.: Three topics in renormalization and improvement. In: , pp. 161–222, 2011. [arXiv:1103.1323].

[Wei83] Weisz, P.: Continuum limit improved lattice action for pure Yang- Mills theory. 1. In: *Nucl. Phys.*, volume B212:p. 1, 1983. doi:10.1016/0550-3213(83)90595-3.

[Wil74] Wilson, K. G.: Confinement of quarks. In: *Phys. Rev.*, volume D10:p. 2445, 1974. doi:10.1103/PhysRevD.10.2445.

[Wil77] Wilson, K. G.: Quarks and strings on a lattice. In: *New phenomena in subnuclear physics., ed. A. Zichichi*, 1977. Plenum Press, New York (Erice, 1975).

[Wol04] Wolff, U. (ALPHA): Monte Carlo errors with less errors. In: *Comput. Phys. Commun.*, volume 156:p. 143, 2004. doi:10.1016/S0010-4655(03)00467-3. [hep-lat/0306017].

[WW84] Weisz, P.; Wohlert, R.: Continuum limit improved lattice action for pure Yang- Mills theory. 2. In: *Nucl. Phys.*, volume B236:p. 397, 1984. doi:10.1016/0550-3213(84)90543-1.

[YHM05] Yagi, K.; Hatsuda, T.; Miake, Y.: *Quark Gluon Plasma*. Cambridge University Press, 2005.

[Zei08] Zeidlewicz, L.: *Gitterregularisierte QCD mit chiral verdrehtem Massenterm bei endlichen Temperaturen*. Diploma thesis, Westfälische Wilhelms-Universität Münster, 2008.

[Zei11] Zeidlewicz, L.: *The thermal transition of quantum chromodynamics with twisted mass fermions*. Ph.D. thesis, Johann Wolfgang Goethe-Universität Frankfurt am Main, 2011.

List of Figures

List of Tables

Selbständigkeitserklärung

Ich erkläre, dass ich die vorliegende Arbeit selbständig und nur unter Verwendung der angegebenen Literatur und Hilfsmittel angefertigt habe.

Berlin, den 4.10.2012 Florian Burger